

# Qualitative Effect of Tissue Heterogeneity and Modiolus Porosity on the Transmembrane Potential of Type - 1 Spiral Ganglion Neurons in the Human Cochlea: A Simulation Study

DISSERTATION

*submitted to obtain the degree of Doctor Engineer (Dr. -Ing.)*

*to the*

Faculty of Computer Science and Electrical Engineering  
University of Rostock,  
Germany

September, 2018

**Author:**

Kiran Kumar Sriperumbudur  
born on 10.05.1976 in  
Karakkayalagudem, India

## **Reviewers:**

### 1. Reviewer

Prof. Dr. Ursula van Rienen  
Institute of General Electrical Engineering,  
University of Rostock, Germany

### 2. Reviewer

Prof. Dr. Hans wilhelm Pau (emiratus)  
Clinic and Polyclinic of Ear, Nose and Throat,  
University of Rostock, Germany

### 3. Reviewer

Prof. Dr. Anthony Gummer  
Department of Otolaryngology,  
University of Tübingen, Germany

### 4. Reviewer

Prof. Dr. Sascha Spors  
Institute of Communications Engineering,  
University of Rostock, Germany

**Date of submission:** September 26, 2018

**Date of defense:** Febraury 19, 2019

# Declaration of Authorship

I, Kiran Kumar Sriperumbudur  
born on 10.05.1976 in

Karakkayalagudem, India, declare that this thesis titled, "Qualitative Effect of Tissue Heterogeneity and Modiolus Porosity on the Transmembrane Potential of Type - 1 Spiral Ganglion Neurons in the Human Cochlea: A Simulation Study" and the work presented in it are my own. I confirm that:

- This work was done wholly or mainly while in candidature for a research degree at this University.
- Where any part of this thesis has previously been submitted for a degree or any other qualification at this University or any other institution, this has been clearly stated.
- Where I have consulted the published work of others, this is always clearly attributed.
- Where I have quoted from the work of others, the source is always given. With the exception of such quotations, this thesis is entirely my own work.
- I have acknowledged all main sources of help.
- Where the thesis is based on work done by myself jointly with others, I have made clear exactly what was done by others and what I have contributed myself.

Signed:

---

Date:

---



*“Creativity is the greatest rebellion in existence ”*

OSHO



# Abstract

Electric stimulation of auditory nerve by cochlear implants has been a successful clinical intervention to treat the sensorineural deafness. However, the mechanism of interaction between the applied electric field and its neural counterparts such as intact spiral ganglion neurons (SGNs) in the cochlea has not been fully explored. Many experimental studies have been suggesting that the morphological features of the cochlea, electrophysiological properties of neural components, electrode design, electrode placement and stimulating strategies are the main factors that affect the functionality of cochlear implants. Even though the factors mentioned above are included explicitly and implicitly in the modeling, the existing contextual *in silico* studies of the cochlea could not adequately explain the stochastic and dynamic firing of intact type -1 SGNs. Although evident, the orientation and clusters of the SGNs, the modiolus porosity, and the tissue heterogeneity in the Rosenthal's canal have often been neglected in the state-of-the-art *in silico* studies due to modeling complexities.

In the present study, two innovative methods *viz.* image-based method and equation based method are proposed to model the modiolus porosity and tissue heterogeneity in the Rosenthal's canal (RC). The qualitative effect of these microstructures on the sub-threshold transmembrane potential ( $V_m$ ) of the SGNs is investigated using two-dimensional and three-dimensional finite element models of the cochlea.

The simulation results suggest that in the presence of a homogeneous extracellular medium in the RC, the signal initiation sites vary with the orientation of the SGNs. Also, the clusters of SGNs would act as a single giant cell during the signal generation and propagation. Further, if the modiolus is assumed as a hard bone, the corresponding electric conductivity would result in very low  $V_m$  of the SGNs. In contrast, if the modiolus is assumed as a porous bone, the corresponding effective conductivity would result in very high  $V_m$  of the SGNs. Nevertheless, the conductivity mapped on the porous modiolus using image-based method have yielded a moderate  $V_m$  of SGNs. The proposed equation-based method suggests that the global and local porosity of the modiolus would profoundly affect the  $V_m$  of the SGNs.

Further, in the presence of a heterogeneous medium that comprised of satellite glial cells (SGCs) and myelinated tissues in the RC, the SGN-electrode distance has a trivial effect on the  $V_m$  of the SGNs. On the contrary, the pathology of the cochlea that could alter the tissue density in the RC would profoundly affect the stimulation profile of the SGNs. Within the scope of the present study, it can be suggested that the variable degree of heterogeneity around each SGN could be one of the reasons for the dynamic firing of the SGNs. The simulation results also advocate the importance of accurate dielectric values of various tissues for *in silico* modeling.

Apart from the academic interest, the present study stresses the importance of further extensive research on the tissue heterogeneity and the modiolus porosity in the RC for the optimization of the performance of cochlear implants.



# Zusammenfassung

Die elektrische Stimulation des Hörnervs durch Cochlea-Implantate hat sich bei der klinischen Intervention zur Behandlung der sensorineuralen Taubheit als erfolgreich erwiesen. Der Mechanismus der Wechselwirkung zwischen dem angelegten elektrischen Feld und seinen neuralen Gegenstücken wie den intakten Spiralganglionneuronen (SGNs) in der Cochlea wurden noch nicht vollständig erforscht. Viele experimentelle Studien deuten darauf hin, dass sowohl die morphologischen Merkmale der Cochlea, als auch elektrophysiologische Eigenschaften von neuralen Komponenten, Elektroden-Design, Elektrodenplatzierung und Stimulierungsstrategien die Hauptfaktoren sind, welche die Funktionalität von Cochlea-Implantaten beeinflussen. Obwohl die oben genannten Faktoren explizit und implizit in die Modellierung einbezogen sind, konnten bisherige kontextuelle *in silico*-Studien der Cochlea das stochastische und dynamische Feuern der intakten Typ-1 SGNs nicht adäquat erklären. Obwohl offensichtlich, wurden die Ausrichtung und Cluster der SGNs, die Modiolus-Porosität und die Gewebe-Heterogenität im Rosenthal-Kanal in den modernen *in silico*-Studien aufgrund von Modellkomplexitäten oft vernachlässigt.

In der vorliegenden Studie werden mit einer bildbasierten Methode und einem auf einer Gleichung basierten Verfahren zwei innovative Methoden vorgeschlagen, um die Modiolus-Porosität und Gewebheterogenität im Rosenthal-Kanal (RC) zu modellieren. Der qualitative Effekt dieser Mikrostrukturen auf das unterschwellige Membranpotential der SGNs wird unter Verwendung von zweidimensionalen und dreidimensionalen Finite-Elemente-Modellen der Cochlea untersucht.

Die Simulationsergebnisse legen nahe, dass in Gegenwart eines homogenen extrazellulären Mediums im RC die Signalinitiierungsstellen mit der Orientierung der SGNs variieren. Weiterhin wirken die Cluster von SGNs während der Signalerzeugung und -ausbreitung als eine einzelne Riesenzelle. Wenn ferner der Modiolus als ein harter Knochen angenommen wird, würde die entsprechende elektrische Leitfähigkeit zu einem sehr niedrigen Membranpotential der SGNs führen. Im Gegensatz dazu würde, wenn der Modiolus als ein poröser Knochen angenommen wird, die entsprechende effektive Leitfähigkeit zu einem sehr hohen Membranpotential der SGNs führen. Nichtsdestoweniger ergab die Leitfähigkeit, die auf dem porösen Modiolus unter Verwendung einer bildbasierten Methode abgebildet wurde, ein moderates Membranpotential von SGNs. Die vorgeschlagene, auf einer Gleichung basierende Methode, legt nahe, dass eine globale und lokale Porosität des Modiolus, das Membranpotential der SGNs tiefgreifend beeinflussen.

Weiterhin hat der SGN-Elektrodenabstand in Anwesenheit eines heterogenen Mediums, das aus Satellitengliazellen (SGCs) und myelinisierten Geweben im RC besteht, eine triviale Wirkung auf das Membranpotential der SGNs. Im Gegensatz dazu würde die Pathologie der Cochlea, die die Gewebedichte in der RC verändern könnte, das Stimulationsprofil der SGNs tiefgreifend

beeinflussen. Die vorliegende Studie legt nahe, dass der variable Grad der Heterogenität um jede SGN einer der Gründe für die dynamische Auslösung der SGNs sein könnte. Die Simulationsergebnisse unterstreichen auch die Wichtigkeit genauer dielektrischer Werte (elektrische Leitfähigkeit, relative Permittivität) verschiedener Gewebe für die *in silico*-Modellierung.

Neben dem akademischen Interesse betont die vorliegende Studie die Bedeutung weiterer umfangreicher Forschung zur Gewebheterogenität und zur Modiolus-Porosität im RC zur Optimierung der Leistung von Cochlea-Implantaten.

# Acknowledgements

I am grateful to:

**Prof. Dr. Ursula van Rienen** for giving me the opportunity and freedom to choose the research objectives. She stood by my side and guided me whenever I was in doubt. She always made me to believe that the 'impossibility' in science is nothing but a delayed possibility in the future. Her unique style of supervision and rich flavor of humanity are great takeaways for my future endeavors.

**Prof. Dr. Hans wilhelm Pau** for his support and encouragement during my research. I am thankful to Prof. Pau for introducing me to Prof. Anthony Gummer.

**Prof. Dr. Anthony Gummer** for accepting to review my thesis. The bloc practicum conducted by Prof. Gummer helped me a lot to have a right perspective of my research.

**German Research Foundation (DFG)** for the financial support through Research Training Group 1505 'welisa'.

I am indebted to *Sri K. Giridhar* for helping me during my undergraduate studies which paved a way to my academic career.

I am privileged to have Prof. Dr. Mohit Kumar and Dr. Shefali Kumar as my extended family. They have supported me in every walk of life.

I am indebted to Aruna-KLN chary-Adithi, Prasanna-Rajkumar-Amulya-Anmol, Dr. K. Srinivasa Chary, Dr. S. Sriranga Chary, Prof. S. Laxmana Murthy, Smt. Kamala and Sri. Umamaheshwara Sharma for their unconditional love and support.

I am pretty much lucky to have my friends Bhaskar, Suri, Bhavani, Venkat, Recep and Kati. I am thankful to all my colleagues for their understanding and cooperation during the difficult times. I appreciate Karthik Sridhar for his assistance. I am also thankful to those individuals who have criticized me for my betterment.

I am very much pleased with the lively presence of Swathi-Phani-Virat. Their love and support made me special in many ways.

Right from the day I first met Revathi, the magic of her love has transformed my life. She is the one who in the first place encouraged me to join the research group when I was indecisive about my career. We spent together all these years learning, growing and complementing each other. I have no words to express my gratitude towards my beauty with brains Revathi, my sweet heart Rasya and lovely Sriram.

My mother Smt. Andamma, inspite of her deteriorating health, encouraged me to go abroad while perhaps she needed me the most. My father Sri. Narsimha Chary taught me how to stay cool and enjoy the life as it comes. I bow down to the feet of my parents for being my greatest teachers and best friends.

The more I understand the manifested form of science the more I fascinated with the unmanifested form of the energy behind it. I salute both the manifested and unmanifested forms of the universal energy..!

# Contents

<b>Declaration of Authorship</b>	<b>iii</b>
<b>Abstract</b>	<b>vii</b>
<b>Acknowledgements</b>	<b>xi</b>
<b>1 Introduction</b>	<b>1</b>
1.1 Motivation . . . . .	1
1.2 Problem definition . . . . .	2
1.3 Thesis organization . . . . .	3
<b>2 Background</b>	<b>5</b>
2.1 The mechanism of hearing . . . . .	5
2.1.1 Outer ear . . . . .	5
2.1.2 Middle ear . . . . .	5
2.1.3 Inner ear . . . . .	6
2.2 The cochlea . . . . .	7
2.2.1 Signal-generating mechanism . . . . .	7
2.2.2 Signal-receiving mechanism . . . . .	8
2.3 Hearing loss . . . . .	9
2.4 Cochlear implants . . . . .	10
2.5 <i>In silico</i> models . . . . .	11
2.5.1 Some state-of-the-art <i>in silico</i> models . . . . .	11
2.5.2 Quasistatic approximation . . . . .	14
2.5.3 Finite Element Method . . . . .	16
2.6 Mesh convergence . . . . .	17
<b>3 Electric Stimulation of Intact SGNs in a Homogeneous Medium</b>	<b>23</b>
3.1 Extracellular stimulation of a neural tissue . . . . .	23
3.1.1 Activating function . . . . .	24
3.2 Modeling transmembrane potential of SGNs in a homogeneous medium . . . . .	25
3.2.1 Model geometry . . . . .	26
3.2.2 Transmembrane potential . . . . .	29
3.2.3 Boundary conditions . . . . .	30
3.2.4 Thin film approximation of the membrane . . . . .	31
3.2.5 Dielectric properties of biological tissues . . . . .	33
3.3 Simulation . . . . .	34
3.3.1 2D results . . . . .	34
3.3.2 Effect of SGN orientation on the signal initiation sites . . . . .	35

3.3.3	Spiral ganglion neuronal clusters . . . . .	39
3.3.4	3D results . . . . .	42
3.4	Summary . . . . .	43
<b>4</b>	<b>Modeling the Porosity of the Modiolus</b>	<b>45</b>
4.1	The Modiolus . . . . .	45
4.2	Modeling the modiolus porosity . . . . .	46
4.2.1	Image-based modeling . . . . .	47
4.2.2	Results . . . . .	47
4.2.3	Equation-based modeling . . . . .	52
4.3	Summary . . . . .	55
<b>5</b>	<b>Modeling Tissue Heterogeneity in the Rosenthal's Canal</b>	<b>57</b>
5.1	The Rosenthal's canal . . . . .	57
5.2	Problem definition . . . . .	58
5.3	Method . . . . .	59
5.3.1	Allocation of electric conductivities to the tissues . . . . .	61
	Electric conductivity of satellite glial cells . . . . .	61
5.3.2	Tissue classification in the Rosenthal's canal . . . . .	62
5.4	Simulation . . . . .	63
5.5	Results . . . . .	66
5.5.1	Scenario1 . . . . .	66
5.5.2	Scenario2 . . . . .	67
5.5.3	Scenario3 . . . . .	69
5.5.4	Anisotropic conductivity of group2 tissues . . . . .	76
5.5.5	Tissue depletion in Rosenthal's canal . . . . .	80
5.6	Discussion . . . . .	82
5.7	Summary . . . . .	84
<b>6</b>	<b>Conclusion</b>	<b>87</b>
	<b>Bibliography</b>	<b>93</b>

# List of Figures

2.1	Middle ear . . . . .	6
2.2	Inner ear . . . . .	7
2.3	Cochlear duct . . . . .	8
2.4	Organ of corti . . . . .	9
2.5	Cochlear Implant . . . . .	10
2.6	Types of finite elements . . . . .	17
2.7	Manual mesh . . . . .	19
2.8	Absolute error and relative error . . . . .	20
2.9	Total electric energy estimation . . . . .	20
2.10	Skewness estimation . . . . .	21
3.1	Passive response of the membrane . . . . .	24
3.2	Comparison of transmembrane potential and AF . . . . .	26
3.3	SGN model . . . . .	27
3.4	2D computational domain . . . . .	28
3.5	3D parametric model of human cochlea . . . . .	29
3.6	3D computational domain . . . . .	30
3.7	Membrane approximation . . . . .	32
3.8	Potential distribution in 2D computational domain . . . . .	34
3.9	Transmembrane potentials of SGNs . . . . .	36
3.10	Signal initiation sites on SGNs for $0^\circ$ . . . . .	37
3.11	Random orientation of SGNs in the RC . . . . .	37
3.12	Signal initiation sites on SGNs for $45^\circ$ orientation . . . . .	38
3.13	Signal initiation sites on SGNs for $90^\circ$ orientation . . . . .	39
3.14	Signal propagation in the SGN clusters . . . . .	40
3.15	Signal propagation in a cluster due to the ephaptic coupling . . . . .	41
3.16	Potential distribution in the 3D computational domain . . . . .	42
4.1	Porous Modiolus . . . . .	46
4.2	Image based modiolus porosity samples . . . . .	48
4.3	Transmembrane potential as a function of modiolus conductivity . . . . .	49
4.4	Effective conductivity of the modiolus . . . . .	50
4.5	Effective conductivity <i>vs</i> mapped conductivity . . . . .	51
4.6	Equation based modiolus porosity samples . . . . .	54
4.7	Effect of local porosity on the induced $V_m$ of the SGNs . . . . .	55
5.1	Immunohistochemistry of the human SGN . . . . .	59
5.2	Image of immunohistochemistry of SGN . . . . .	60
5.3	2D Computational containing SGN contours . . . . .	60
5.4	RGB color coded tissues in the RC . . . . .	61

5.5	Automatic mesh generated by COMSOL for the computational domain. . . . .	64
5.6	Mesh refinement on the thin tissues . . . . .	65
5.7	Electric field distribution in the RC in Scenario1 . . . . .	67
5.8	Effect of SGN shape on the induced transmembrane potential	68
5.9	Potential distribution in Scenario2 . . . . .	68
5.10	Induced transmembrane potential in Scenario2 . . . . .	70
5.11	Electric potential and electric field distribution in Scenario3 . .	71
5.12	Transmembrane potential in Scenario3 . . . . .	72
5.13	Transmembrane potential of first eight SGNs in Scenario3 . . .	74
5.14	Transmembrane potential of next eight SGNs in Scenario3 . .	75
5.15	Anisotropic conductivity in the Cartesian global coordinate system . . . . .	78
5.16	Anisotropy in curvilinear coordinates system . . . . .	79
5.17	Transmembrane potential as the function of the tissue depletion	81
5.18	Effect of low conductive layer . . . . .	83



# List of Tables

2.1	Differential and integral forms of Maxwell's equations. . . . .	14
2.2	Mesh parameters . . . . .	18
3.1	Dimensions of computational subdomains . . . . .	29
3.2	Electric conductivity of biological tissues . . . . .	33
3.3	FHN parameters . . . . .	40
5.1	Electric conductivity values of sub-domains. . . . .	62



# Abbreviations

<b>AIS</b>	Axonal Initial Segments
<b>AN</b>	Auditory Nerve
<b>C1-C19</b>	Cell numbers
<b>CI</b>	Cochlear Implants
<b>FEM</b>	Finite Element Method
<b>LEM</b>	Lumped Element Model
<b>MRT</b>	Magnetic Resonance Tomography
<b>NMSC</b>	Non-Myelinated Schwann Cells
<b>RC</b>	Rosenthal's Canal
<b>RGB</b>	Red Green Blue
<b>S1-S9</b>	Sample numbers
<b>SEM</b>	Scanning confocal Electron Microscopy
<b>SGC</b>	Satellite Glial Cells
<b>SGN</b>	Spiral Ganglion Neurons
<b>SIS</b>	Signal Initiation Site
<b>TEM</b>	Transmission Electron Microscopy
$V_m$	Transmembrane Potential
<b>VCM</b>	Volume Conductor Model
<b>μCT</b>	micro Computer Tomography



*Dedicated to*

**MY FAMILY**



# Chapter 1

## Introduction

"Blindness separates us from things  
but deafness separates us from  
people."

---

*Helen Keller*

### 1.1 Motivation

A healthy hearing organ functions through various electro-mechanical processes. Any malfunction in the auditory transduction from the outer ear to the auditory cortex could result in different levels of hearing impairment. Over 360 million people worldwide, especially children are suffering from profound hearing loss [1]. Since the hearing provides necessary inputs to the brain for the social, intellectual and creative growth, many profoundly deaf children are facing social, psychological and economic deprivation [2, 3].

Various genetic, pathological and physical factors could induce the profound deafness in humans [4, 5]. Of those, depletion of inner hair cells and subsequent degeneration of peripheral processes of the auditory nerve leads to the sensory neural deafness [6]. In such pathology, electric stimulation of intact spiral ganglion neurons (SGNs) of the auditory nerve by cochlear implants (CI) has been an approved clinical intervention to treat the profound deafness [7, 8, 9]. Historically, the first cochlear implant consisting of a single channel electrode was clinically tested in 1961 [10]. Since then, the experimental studies related to morphology, electrophysiology of the auditory nerve have been enriching the knowledge about the mechanism of action potential (AP) generation and propagation in the cochlear neurons [11]. Alongside, cutting-edge technology has been offering new possibilities to build highly customized software and sophisticated electronic devices [12, 13]. In spite of abundant scientific and technological support, cochlear implants have been suffering an undesirable performance plateau [14, 15, 16]. For example, the quality of sound perception in noisy ambiances and clean pitch discrimination in music are still craving features for CI recipients [17].

In the midst of these experimental and technological developments, various *in silico* studies have been providing valuable insights to the hearing

research. Especially, mathematical models could foresee the effect of different anatomical and electrophysiological factors on the electric field distribution. For example, using an appropriate *in silico* model, one could visualize the interaction between the applied electric field and the targeted SGNs which is incomprehensible in *in vivo* studies. State-of-the-art *in silico* cochlea models admissibly play an indispensable role for the optimization of the CI functionality. On the one hand, *in silico* studies of biological systems have unprecedented advantages over other methods in understanding, asserting, and predicting the outcome of underlying biological processes; on the other hand, many computer models have severe drawbacks in reproducing realistic biological scenarios.

Understandably, mathematical models rely on essential simplifications and necessary assumptions to formulate a biophysical scenario. For example, in the majority of *in silico* studies which are discussed in the later chapters, nerve fibers and SGNs were assumed as thin cylinders and regular spheres respectively [18]. Likewise, many morphological and anatomical constituents of the human inner ear were ignored in the process of problem simplification. Strikingly, some evident parameters were either neglected or overly simplified in almost all existing *in silico* studies of the auditory nerve. Apparently such rudimentary modeling approaches with a variety of computational and modeling limitations could be a reason for many discrepancies in the results of simulation studies and experimental studies. Prospectively, every scientific study has been contributing directly or indirectly to the development of high efficient multichannel cochlear implants. In that sense, it is very motivating to ascertain that each bit of knowledge added to hearing research could prove invaluable for deaf people worldwide.

## 1.2 Problem definition

Electric field distribution in the Rosenthal's canal (RC) is a widely studied phenomenon through *in silico* modeling. The modiolus bone and the extracellular medium in the RC are the most essential computational domains, especially in the volume conductor models of the cochlea. Strikingly, almost all existing *in silico* models have assumed a homogeneous extracellular medium and non-porous modiolus bone in the RC for computations [19, 20]. However, it is evident from the temporal bone studies that:

- The spatial arrangement of type-1 SGNs in the RC is asymmetric. Also, type-1 SGNs in the RC form clusters,
- The Modiolus is not a hard bone; rather it is the fabrication of multiple porous layers,
- The extracellular medium in the Rosenthal's canal contains various heterogeneously distributed tissues.

The inclusion of above micro-anatomical features in an *in silico* model of the cochlea could yield entirely different electric field distribution in the RC. On



the one hand, the simulation results could even contravene several predictions of corresponding state-of-the-art *in silico* models. On the other hand, these results could provide a valuable theoretical base to explain the dynamic firing behavior of SGNs. Also, one could anticipate an explanation for the disproportion between the number of survived spiral ganglion neurons and the hearing quality. Such model could also serve as a useful tool for optimizing the CI electrode functionality. The simulation results could be useful to explore the intrinsic factors that are affecting the selective stimulation of SGNs.

This thesis is intended to present a fresh perspective and a qualitative analysis regarding:

- The random spatial arrangement of spiral ganglion neurons and its effects on the signal initiation sites during the electric stimulation of ‘amputated’ auditory neurons,
- The impact of highly porous modiolus bone on the electric field distribution in the Rosenthal’s canal,
- The effect of tissue heterogeneity on the stimulation profile of intact spiral ganglion neurons.

## 1.3 Thesis organization

**Chapter 2** presents an overview of auditory transduction, a short note about the cochlear implants and a concise summary on the advantages and drawbacks of a few contextual mathematical models of the cochlea.

**Chapter 3** contains the theoretical background and a concise discussion of the relevant finite element models which describe the electric stimulation of auditory nerve by cochlear implants.

**Chapter 4** introduces two novel methods for implementing the modiolus porosity in a three-dimensional computational model of the cochlea. Apart from the image-based method, a set of reaction-diffusion equations to replicate the asymmetric porosity of multi-layered modiolus is described in this chapter.

**Chapter 5** presents an image-based method to implement the tissue heterogeneity in the RC in a two-dimensional finite element model of the cochlea. The significance and clinical relevance of the simulation results are presented.

**Chapter 6** contains the conclusion and a discussion on the prospect of the present study.



# Chapter 2

## Background

This chapter contains a brief account on the mechanism of auditory transduction in a healthy human ear and describes the causes of deafness and the functionality of cochlear implants. A categorical literature review on the existing *in silico* models is also provided in this chapter.

### 2.1 The mechanism of hearing

As the consequence of coherently functioning small and complex organs which are sensitive to external acoustic stimuli, the human could perceive the hearing sensation [21]. The mechanism of hearing takes place in three important stages involving respective functional units of the hearing organ.

#### 2.1.1 Outer ear

The outer ear is a unique cartilage structure called pinna that protrudes from both, left and right side of the skull. Naturally designed pinna localizes the incoming sound energy and sends it through a narrow ear canal that proceeds towards the eardrum. The eardrum is a tympanic membrane of approximately 1 cm diameter and 0.1 mm thickness that separates the outer ear from the middle ear. Due to the peculiar structure of the ear canal, the incident acoustic vibrations on the pinna resonate in the ear canal. As a result, tenfold amplified peak pressure could be exerted on the eardrum. In general, the audible frequency of human ranges from 20 Hz to 20 KHz [22]. Recently it has been proved that the unique structure of the outer ear of an individual can be used as a biometric identification factor [23].

#### 2.1.2 Middle ear

The amplified characteristic sound pressure vibrates the cone-shaped eardrum which acts as the first acoustic signal transducer. These mechanical vibrations transfer to the ossicles. Ossicles are tiny bone structures that consist of the malleus, the incus and the stapes. This compound bone structure acts as a sound controller and as a protective device from excessive loudness. Malleus is connected to the eardrum and stapes is connected to the oval window of

the vestibule of the inner ear. In a nut shell, the ossicles concentrate the force of vibrations via certain kind of impedance matching on the oval window [24]. Figure 2.1 depicts the structure of the middle ear.

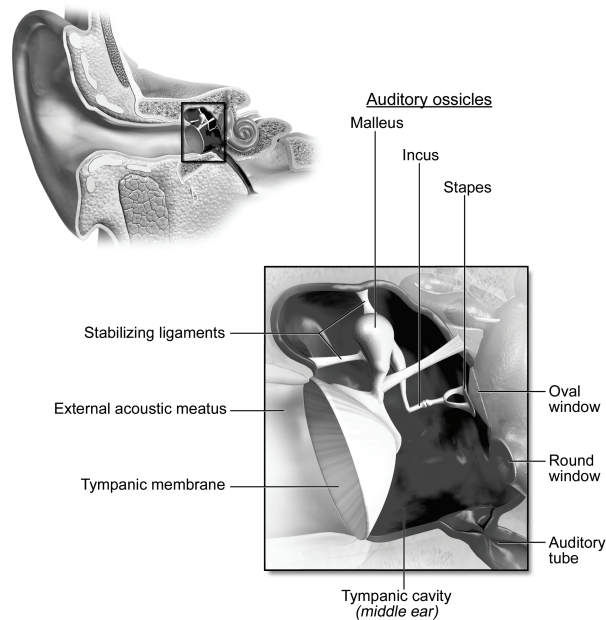


FIGURE 2.1: A sketch of the middle ear (picture source: *Blausen.com staff* (2014). "Medical gallery of Blausen Medical 2014". *WikiJournal of Medicine* 1 (2). DOI:10.15347/wjm/2014.010. ISSN 2002-4436. - Own work, CC BY 3.0, <https://commons.wikimedia.org/w/index.php?curid=29025010>)

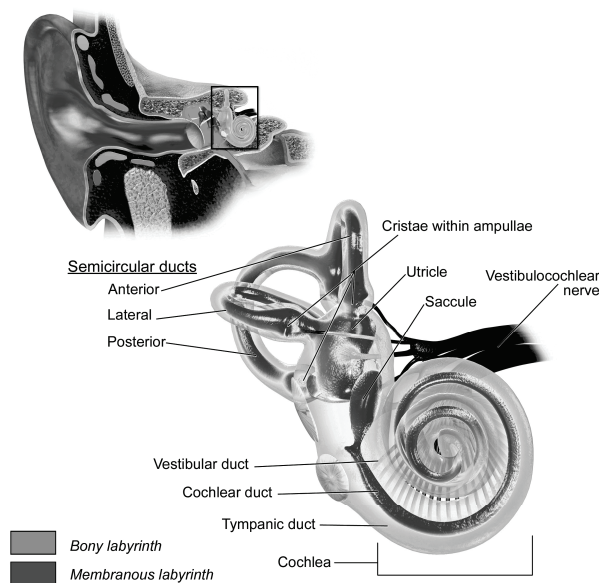
### 2.1.3 Inner ear

The most complex transduction of the mechanical vibrations induced by the Stapes takes place in the inner ear (Figure 2.2). These induced vibrations push the oval window's membrane of the cochlea. As a result, traveling waves are produced in the perilymph of the scala vestibuli. The traveling waves composed of localized peaks move towards the apical region of the cochlea. Through the helicotrema, these fluidic waves travel into the perilymph of the scala tympani. The vibrations of the round window make the compensating movements against the incident fluidic waves in the scala tympani. The orchestral vibrations of the tectorial membrane, the organ of Corti and the basilar membrane push the endolymphatic liquid film between the tectorial membrane and the inner hair cells. These movements deflect the stereocilia resulting in sound-coded electric impulses into the peripheral processes of the auditory nerve. These electric pulses or action potentials (AP) travel through the non-myelinated spiral ganglion neurons and reach the auditory cortex of the brain via central processes of the auditory nerve [25]. In short, the cochlea is an efficient and highly sophisticated frequency analyzer that transforms acoustic signals into corresponding electrical signals. The complex structures

## 2.2. The cochlea

---

of the cochlea need to be adequately understood for unraveling the hearing process.



---

FIGURE 2.2: A sketch of the inner ear (picture source: *Blausen.com staff (2014). "Medical gallery of Blausen Medical 2014.WikiJournal of Medicine 1 (2). DOI:10.15347/wjm/2014.010. ISSN 2002-4436. - Own work, CC BY 3.0,https://commons.wikimedia.org/w/index.php?curid=29025011).*

## 2.2 The cochlea

Human cochlea is a snail-shaped structure with three fluid chambers located within the temporal bone as shown in Figure 2.3. The bony labyrinth helps to reflect the fluid vibrations in the cochlea [26]. The uniqueness in the anatomy of the human cochlea can be compared to the uniqueness of fingerprints of an individual. Hence, any generalized cochlea structure may or may not represent a realistic cochlea. Temporal bone studies [27, 28] indicate that the uncoiled length of the human cochlea varies from 38.6 mm to 45.6 mm with a substantial difference in the dimensions of scalatympani and scalavestibuli. Since the acoustic signal generation in the cochlea is the consequence of complex hydrodynamic activities, the anatomical variations of the cochlea play a prominent role in shaping the individual hearing abilities.

### 2.2.1 Signal-generating mechanism

The scala vestibuli or vestibular duct is the second largest chamber filled with perilymph that is composed of high sodium and low potassium concentrations. The scala vestibule first receives the acoustic vibrations from the membrane of the oval window and transmits the energy further in the form of traveling waves [29]. Scala tympani or tympanic duct is filled with perilymph. The

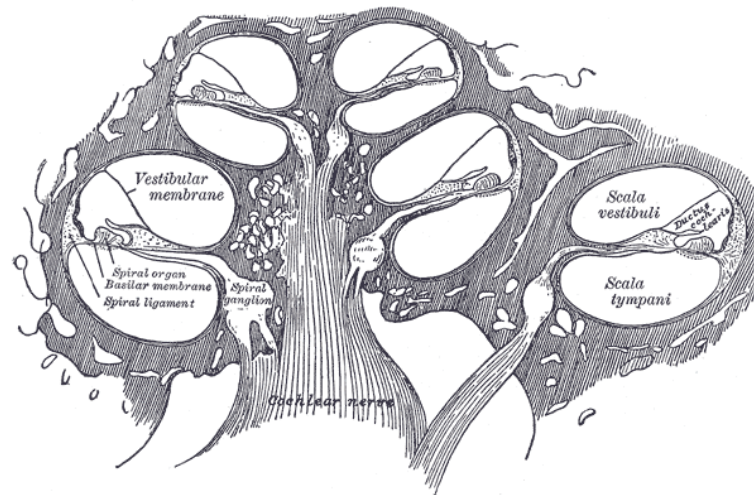


FIGURE 2.3: A schematic cross section of human cochlea. Cochlear duct is situated between scala vestibuli and scala tympani ( Picture source: By Henry Vandyke Carter - Henry Gray (1918) *Anatomy of the Human Body*, Bartleby.com: Gray's Anatomy, Plate 928, Public Domain).

scala vestibuli and the scala tympani have a common transitional region at the apical part of the cochlea called the helicotrema. The hydrodynamic waves from the scala vestibule create a counter-movement in the round window situated at the basal region of the cochlea that damps the energy

The scala media or cochlear duct is filled with endolymph that consists of high potassium and low sodium concentrations. Scala media is situated between scala tympani and scala vestibule. As the housing of the organ of Corti is strategically located in this region, endolymph plays an essential role in triggering the electric signals into the hair cells.

The membranous labyrinth consists of the basilar membrane and the Reissner's membrane which separates the perilymph from the endolymph and thus maintains the much needed endocochlear potential. The basilar membrane supports a travelling wave with an envelope maximum located at a frequency-specific place along the membrane, called the tonotopic place [30]. High frequencies are localized at the base, and low frequencies are localized at the apex [31]. For many species, [32] has derived a generally applicable function to describe the tonotopic place as a function of stimulus frequency.

## 2.2.2 Signal-receiving mechanism

The signal-receiving mechanism consists broadly of three essential components namely, the organ of Corti, inner hair cells, and outer hair cells. The organ of Corti is a micro-architecture composed of a highly varied strip of epithelial cells sitting on the basilar membrane situated in the cochlear duct. It acts as the primary receiving component of the resultant vibrations from the signal-generating mechanisms (Figure 2.4). The epithelium, containing the

### 2.3. Hearing loss

---

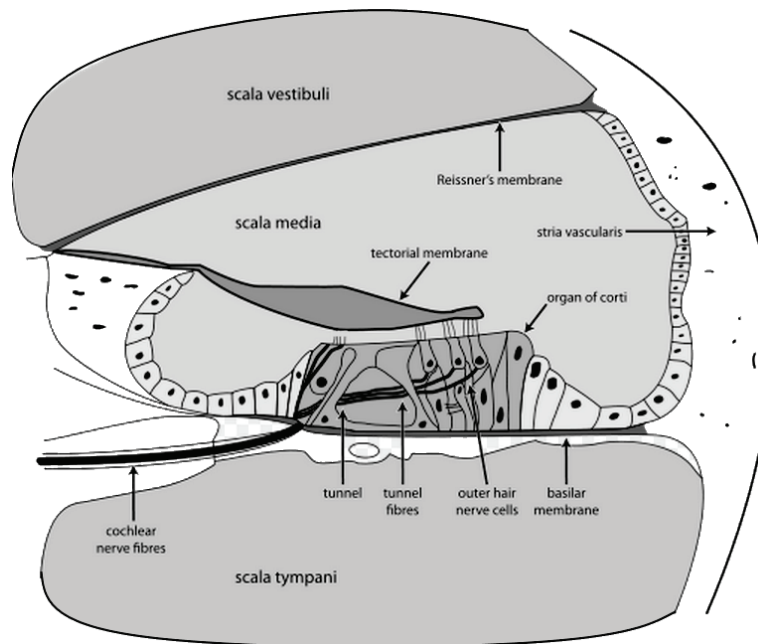


FIGURE 2.4: Organ of Corti comprised of various microstructures (picture source: Oarih at <https://commons.wikimedia.org/w/index.php?curid=3202255>)

hair cells, enables transduction of basilar-membrane vibrations into receptor currents and eventually the generation of action potentials [33, 34].

The transducing elements within the epithelium are the sensory inner hair cells and the electromechanical outer hair cells. Their stereocilia are deflected due to shearing motion between the apical surface of the hair cells and the tectorial membrane. This deflection causes modulation of 1) the opening probability of mechanosensitive channels in the stereocilia, 2) the receptor current, and 3) the receptor potential [35]. In the case of the inner hair cells, the receptor potential modulates the release of transmitter substance, which results in excitatory post-synaptic potentials and action potentials [35].

In the case of the outer hair cells, the receptor potential produces a somatic electromechanical force, which acts against friction to amplify and sharpen the vibration of the basilar membrane and, therefore, the deflection of the stereocilia [36, 37].

## 2.3 Hearing loss

Hearing loss in humans is one of the major sensory disabilities in the world [38]. As a result of the outer and the middle ear infections, otitis, ossicular damage the conductive hearing loss would occur. It can be cured with the proper medication or surgical intervention. The dysfunction of the cochlea due to various pathological, genetic and acquired diseases would result in the sensorineural hearing loss [39]. One of the main reasons for the profound deafness is the loss of hair cells and subsequent decay of peripheral processes [40]. Although

this pathological condition would damage the natural hearing permanently, the intact SGNs and central processes facilitate various hearing restoration interventions like implantation of cochlear electrodes in the inner ear [41].

## 2.4 Cochlear implants

Cochlear implants are successfully restoring the hearing sensation in profoundly deaf people. The general aim of the cochlear implants is to deliver electrical pulses into the auditory nerve similar to the action potential pulses evoked during the natural auditory transduction. Cochlear implants work in two stages, in the first stage, the microphone placed near the patient's ear receives the sound waves and sends the corresponding signals to the signal processing unit. In the second stage, depending upon the frequency of the input signals, various signal processing algorithms mask and code the electrical signals and transmit the respective electrodes to stimulate the auditory nerve fibers [42]. Monopolar, bipolar and tripolar stimulation strategies are presently in use with different energy efficiencies [43]. Figure 2.5 shows a schematic of the outer and inner components of a cochlear implant.

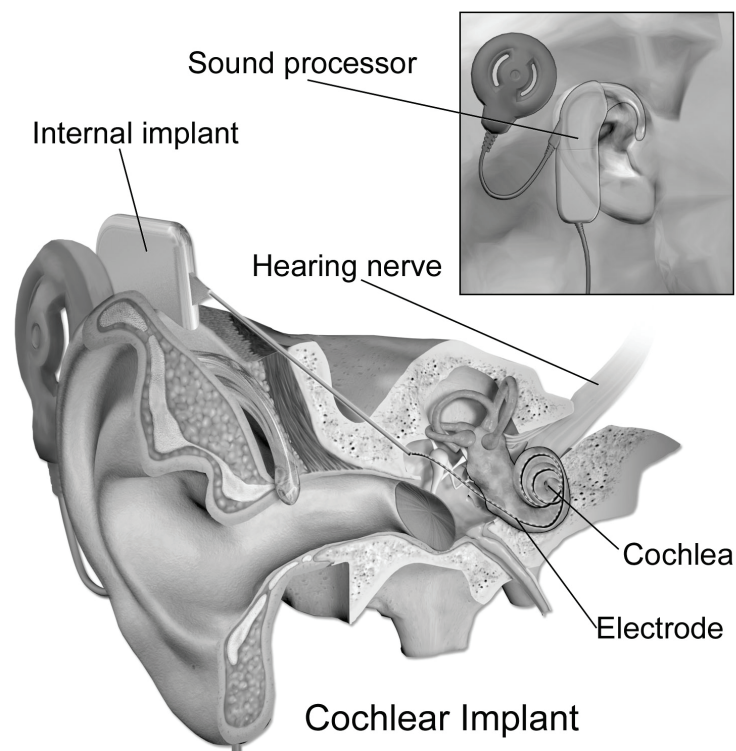


FIGURE 2.5: Cochlear Implant (picture source: Blausen.com staff (2014). "Medical gallery of Blausen Medical 2014". WikiJournal of Medicine 1 (2). DOI:10.15347/wjm/2014.010. ISSN 2002-4436. - Own work, CC BY 3.0, <https://commons.wikimedia.org/w/index.php?curid=29025007>)

In addition to various clinical and technical difficulties, morphological peculiarities such as variation in the anatomy of the cochlea have been posing



significant challenges to determine the optimal electrode insertion depth into the scalatympani with minimal insertion trauma [44]. Another major obstacle to gaining in-depth understanding is the lack of direct access to the auditory neurons. All available data about the auditory nerve and SGNs in the Rosenthal's canal are based on the histochemically fixed cochleae [45]. The preparation method of the cochleae could itself cause damage to the sensitive structures in the Rosenthal's canal. In a way, the exact mechanism of interaction between the cochlear neurons and the applied electric field is still not fully known.

## 2.5 *In silico* models

*In silico* modeling is a heuristic approach for defining and solving a biomedical problem within the scope of permissible assumptions and simplifications.

Simulation of the electric field distribution in the cochlea has been a major modeling objective of *in silico* studies. There exist various *in silico* models which deal with other essential mechanisms of the cochlea, such as the hydrodynamics of the basilar membrane and trauma induced by electrode insertion [46, 47, 48, 49]. With ever-increasing computational power and robust numerical schemes, simulation results of lumped element models, as well as volume conductor models, are opening new windows to explore the cochlea. A concise discussion of some state-of-the-art *in silico* models is given in the following section. Additional details and in-depth literature review of various cochlear models can be found in [19, 50, 51].

### 2.5.1 Some state-of-the-art *in silico* models

Pioneering work of von Békésy [52] using a lumped elements model (LEM) to describe the electrical behavior of the cochlea has laid a foundation for the development of various *in silico* models. Subsequent lumped element models proposed by Johnstone and colleagues in 1966 [53] and Strelhoff in 1973 [54] investigated the electrical pathways and the potential distribution in the guinea pig cochlea. Later, Suesserman and Spielman [55] as well as Kral [56] proposed improved LEMs to study the effect of electrode configuration and the electric field distribution in the cochlea. Vanpoucke and colleagues in 2004 [57] proposed an elegant LEM model based on electrical field imaging. In this model, the dielectric properties of various tissues were modeled as layers of lumped elements to investigate the local current pathways. A major drawback in all lumped element models is the assumption of the uncoiled cochlea in which three fluid chambers run parallel to each other and omission of the real cochlear anatomy and intact neural structures.

Girzon first introduced the inclusion of cochlear anatomy in computational models in 1987 [58] through a volume conductor model (VCM). Unlike lumped element models in which only the effective impedance of cochlear structures was considered, the introduction of VCM made it possible to locally

assign dielectric properties of tissues depending on their spatial arrangement in the cochlea. This method also stressed the significance of the inclusion of cochlear anatomy in *in silico* models. The model visualized various current spreading paths in the cochlea. However, the results are unrealistic due to low-resolution image data, point source electrodes, and usage of finite difference method.

Later, Finely and colleagues [59] proposed a series of VCMs to overcome the limitations of the Girzon model. A three-dimensional stimulating electrode in a cylindrical cochlea extruded from an anatomically detailed two-dimensional slice of the basal turn was modeled to represent a small straight portion of the cochlea. Auditory nerve fibers were also modeled to study the activation of the neural population for various threshold currents using the finite element method. However, the effect of snail shape of the cochlea and the influence of spiral ligament on the electric field distribution were not studied in the model.

Improving upon Finely models, Frijns and colleagues proposed a guinea pig cochlear model with a rotational symmetric geometry [60, 61, 62]. In spite of modeling anomalies and anatomical aberrations, these models have shown the qualitative effect of the curvature of the cochlea on the potential distribution. Further, anatomically realistic human cochlea embedded with realistic electrode geometry and detailed neural pathways was given by Kalkman and colleagues in 2014 [63]. Through these *in silico* models Frijns and his group made compelling arguments about how cochlear anatomy, tissue properties, electrode design, and stimulation pulse shape affect the neural excitation.

Hanekom and others [64] performed some useful investigations in a three-dimensional cochlea model based on the photomicrographs for human cochlea specimens. This model mainly focused on the effect of electrode placement on the asymmetric potential distribution and the subsequent impact on the excitation thresholds of auditory nerve fibers. However, this model geometry was limited to one and a half turn of the cochlea with a constant cross-sectional area.

Rattay and colleagues [65, 66, 67] focused on modeling a detailed neural excitation setup rather than the accuracy of cochlear geometry. Simple helical cochlea geometry with enough anatomical details embedded with a compartment model of nerve fibers was used to investigate the nerve signal latency concerning the morphology and morphometry of the targeted neural elements. However, his proposed 'activating function' to estimate the activated nerve fiber population [68] was sensitive to the geometric irregularities of the model [69]. For this reason, all his models suggested the higher activation probability at the acute curvatures of neural structures. Nevertheless, these models are considered as some of the best mathematical models that describe the electrophysiological properties of the auditory nerve.

Choi [70, 71], Whiten [72], Saba [73] also proposed their study-specific VCMs, especially Grünbaum [74] has investigated the electric field distribution in the scala chambers using anatomically realistic human cochlear model. All volume conductor models of the cochlea signify the role of different macro

and micro components of the cochlea to achieve the optimal cochlear implant performance.

A careful comparative study of models mentioned above reveals that each state-of-the-art *in silico* model has its study-specific advantages followed by unwanted drawbacks. In essence,

- VCMs have unprecedented advantages over LEMs,
- Inclusion of any new anatomical detail in the computational model of the cochlea may result in different model predictions,
- Material properties play a vital role in determining the model output,
- Since a mathematical model is subjected to appropriate assumptions, an *in silico* model could only reproduce a semi-realistic biological phenomenon within the reach of specific mathematical formulations,
- Variations in the cochlear anatomy, uncertainties in the tissue properties and missing anatomical details are impeding the faithful modeling of the cochlea. As a consequence, most of the simulation results have been appreciated for the academic interest but discouraged in the clinical applications.

A set of constituent equations that describe the relation between the material properties of the tissues and the incident electromagnetic wave is necessary to model the electric stimulation of auditory nerve by cochlear implant electrodes. Fundamental equations of electrodynamics which describe the relation between electric and magnetic fields was given by James Clark Maxwell [75]. Broad spectrum of electromagnetic problems can be solved using Maxwell's equations. Differential and integral forms of Maxwell's equations are shown in Table 2.1. Here  $\mathbf{E}$ ,  $\mathbf{B}$ ,  $\mathbf{J}$ ,  $\mu_0$ ,  $\epsilon_0$ ,  $\rho$  are electric field, magnetic flux, current density, permeability of free space, permittivity of free space and electric charge density, respectively.  $\partial\Omega$  is the closed boundary surface of a fixed volume  $\Omega$  and  $\partial\Sigma$  is the closed boundary curve of a fixed surface  $\Sigma$ .

Electromagnetic fields can be classified into stationary fields, quasistatic fields, general time dependent fields and electromagnetic waves. Maxwell's equations representing these field problems can be solved by various analytical and numerical methods. An excellent analysis on Maxwell's equations including various applications and different solution methods was given by van Rienen in [76].

Study specific deduction of the Maxwell's equations is necessary to model a problem. In the case of modeling a low frequency bioelectric phenomenon, the quasistatic approximation described in the following section would be suitable to simulate the electric field distribution.

TABLE 2.1: Differential and integral forms of Maxwell's equations.

Differential form	Integral form
$\nabla \cdot \mathbf{E} = \frac{\rho}{\epsilon_0}$	$\oiint_{\partial\Omega} \mathbf{E} \cdot d\mathbf{S} = \frac{1}{\epsilon_0} \iiint_{\Omega} \rho dV$
$\nabla \cdot \mathbf{B} = 0$	$\oiint_{\partial\Omega} \mathbf{B} \cdot d\mathbf{S} = 0$
$\nabla \times \mathbf{E} = -\frac{\partial \mathbf{B}}{\partial t}$	$\oint_{\partial\Sigma} \mathbf{E} \cdot d\mathbf{l} = -\frac{d}{dt} \iint_{\Sigma} \mathbf{B} \cdot d\mathbf{S}$
$\nabla \times \mathbf{B} = \mu_0 \mathbf{J} + \mu_0 \epsilon_0 \frac{\partial \mathbf{E}}{\partial t}$	$\oint_{\partial\Sigma} \mathbf{B} \cdot d\mathbf{l} = \mu_0 \iint_{\Sigma} \mathbf{J} \cdot d\mathbf{S} + \mu_0 \epsilon_0 \frac{d}{dt} \iint_{\Sigma} \mathbf{E} \cdot d\mathbf{S}$

### 2.5.2 Quasistatic approximation

Present study assumes a volume conductor model in the quasistatic regime in which the extracellular matrix is assumed as homogeneous, isotropic conductive medium. According to Plonsey and Heppner [77], equation (2.1) and equation (2.2) represent the solutions for inhomogeneous Helmholtz equations which are used in bioelectric applications such as extracellular stimulation of the neural tissues with a point source. Here,  $\mathbf{A}(x, y, z)$  and  $\Phi(x, y, z)$  are the vector potential and the scalar potential respectively.

$$\mathbf{A}(x, y, z) = \frac{\mu}{4\pi} \int_{V'} \frac{\mathbf{J}'_s(x', y', z') e^{-jk\mathbf{R}}}{\mathbf{R}} dV'(x', y', z'), \quad (2.1)$$

$$\Phi(x, y, z) = \frac{1}{4\pi(\sigma + j\omega\epsilon)} \int_{V'} \frac{\rho'(x', y', z') e^{-jk\mathbf{R}}}{\mathbf{R}} dV'(x', y', z'), \quad (2.2)$$

here

$$\mathbf{R}^2 = (x - x')^2 + (y - y')^2 + (z - z')^2, \quad (2.3)$$

and for purely resistive medium,

$$k^2 = -j\omega\mu\sigma(1 + j\omega\epsilon/\sigma), \quad (2.4)$$

where  $\mathbf{J}_s, \omega, \mu, \sigma, \epsilon, \mathbf{R}$  and  $V$  are the source current density, angular frequency, permeability, conductivity, permittivity, dimension of the volume of interest and electric potential, respectively. The primed variables refer to the source point whereas unprimed variables refer to the field point. Now the electric field can be defined as

$$\mathbf{E} = -j\omega\mathbf{A} - \nabla\Phi \quad (2.5)$$

A quasistatic bioelectric model should now satisfy the conditions shown in equations (2.6) through (2.9). Here the required dielectric constants in

## 2.5. In silico models

---

the context of the present study are  $\sigma_{avg} = 0.6$  S/m,  $R_{max} = 2 \times 10^{-3}$  m,  $\omega = 2000\pi$  rad/s for 1 kHz frequency and  $\mu = 4\pi \times 10^{-7}$  H/m.

- *Propagation effect*: Equations (2.3) and (2.4) yield  $kR_{max} \approx 1.36 \times 10^{-4}(1 - j)$  that satisfies

$$|kR_{max}| \ll 1 \quad (2.6)$$

Equation (2.6) makes the phase shift term  $e^{-jkR}$  in (2.1) and (2.2) to unity. Hence, the propagation effects in the system can be neglected.

- *Inductive effect*: If the propagation effects are negligible then the inductive effects can be neglected, since equation (2.6) readily satisfies

$$|kR_{max}|^2 \ll 1 \quad (2.7)$$

- *Capacitive effect*: To neglect the capacitive effects, the medium should satisfy

$$\omega\varepsilon/\sigma \ll 1 \quad (2.8)$$

Since the coefficient  $(\sigma + j\omega\varepsilon)$  in equation (2.2) which can be written as  $\sigma(1 + j\omega\varepsilon/\sigma)$ , it will become a real number as a consequence of equation (2.8). Even though this condition is not robust with high frequencies, the medium can be considered as resistive in low frequencies.

- *Boundary conditions*: The normal component at the boundaries of two different tissues with electric conductivities  $\sigma_1$  and  $\sigma_2$ , respectively, should obey the continuity boundary condition since the total current is solenoidal. Hence,

$$(\sigma_1 \mathbf{E}_{1n} - \sigma_2 \mathbf{E}_{2n}) = 0 \quad (2.9)$$

After applying the conditions shown in equations (2.6) through (2.9) in equation (2.2) and equation (2.5) yields,

$$\Phi(x, y, z) = \frac{1}{4\pi\sigma} \int_{V'} \frac{\rho'(x', y', z')}{R} dV'(x', y', z'), \quad (2.10)$$

and

$$\mathbf{E} = -\nabla\Phi \quad (2.11)$$

Then the quasi-stationary assumption for the homogeneous extracellular medium without magnetic effects yields

$$\nabla^2\Phi = -\frac{\rho}{\sigma} \quad (2.12)$$

Thus, the electric field distribution in the Rosenthal's canal without any internal sources can be calculated by solving the following constituent equations

$$\mathbf{J} = \sigma \mathbf{E} \quad (2.13)$$

$$\mathbf{E} = -\nabla\Phi \quad (2.14)$$

$$\nabla \cdot (\nabla\Phi) = 0 \quad (2.15)$$

Here  $\mathbf{J}$ ,  $\mathbf{E}$  and  $\Phi$  represent the current density, electric field and electric potential, respectively; while  $\sigma$  represents the electric conductivity of the given computational subdomain.

### 2.5.3 Finite Element Method

Analytical solutions are not always possible for physical problems defined by partial differential equations (PDE). However, the solution can be approximated using numerical methods. A suitable numerical method is essential to solve the defined problem on a computational domain. The present study intended to model the electric stimulation of auditory nerve by cochlear implant electrodes. The model geometry consists of many thin and complex domains. In such cases, the finite element method (FEM) is considered as a suitable choice [78, 79] to simulate the electric field distribution. FEM solves the differential form of Maxwell's equations for the electric field distribution considering the dielectric properties, initial values and boundary conditions on model domains.

Basically, FEM proceeds in four stages [80, 81] *viz.* discretization of the solution region into finite subregions called finite elements, deriving the governing equations, assembling the elements of the solution region, and solving the resultant equation system.

In the first stage, the discretization process subdivides the model geometry into small elements and interconnects them at finite number of nodes. This offers the flexibility of using irregular grids to efficiently handle the meshing of complex geometries. Depending upon the spatial dimensions of the model geometry, different mesh elements *viz.* linear, triangular or tetrahedral etc. are used for discretization (please refer Figure 2.6).

The central idea of FEM is to approximate the solution by some linear combination of basis functions on discrete number of points in a computational domain. For instance, if  $\phi$  is a dependent quantity in a physical system described by a PDE, then an approximation of the real solution can be expressed as

$$\phi \approx \phi_h = \sum_i \phi_i \psi_i \quad (2.16)$$

here  $\phi_h$  is the approximate solution,  $\psi_i$  are the basis functions and  $\phi_i$  are the coefficients of the basis functions. An elaborate discussion about the FEM is beyond the scope of the present study. A further concise description of FEM in the context of solving equation (2.15) on a simple geometry can be found in [80, 81].

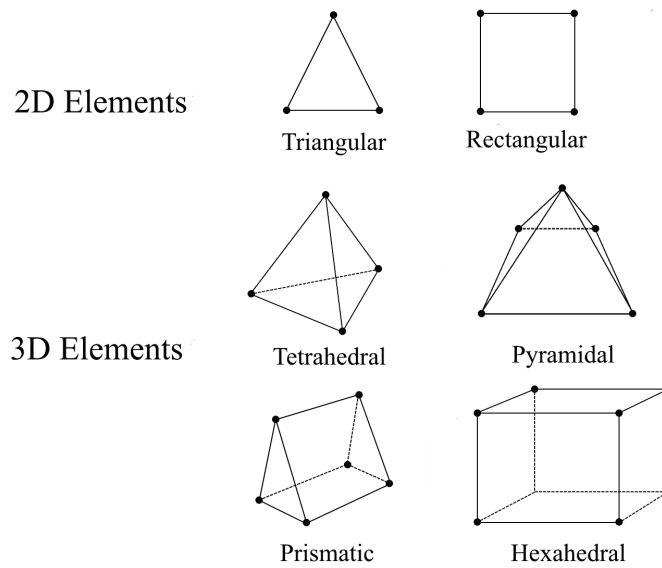


FIGURE 2.6: Some basic 2D and 3D finite elements.

## 2.6 Mesh convergence

All simulations in the present study were performed using COMSOL Multiphysics<sup>®</sup> software (here after referred as COMSOL) that is based on FEM. COMSOL offers flexible and versatile meshing options for discretization of the complex topology of computational domains. Depending upon the dimensions of the computational domain, the software offers different predefined meshing options and study-specific automatic meshing options. Present study was performed in 2D and 3D geometries with different layers of subdomains. Three orders of magnitude size variance of subdomains was tackled carefully during the meshing process.

Eight different mesh cases were studied on 3D computational domain. First, seven study-specific predefined mesh cases namely *extremely coarse*, *coarser*, *coarse*, *normal*, *fine*, *finer*, *extremely fine* were studied for mesh convergence considering the parameters given in Table 2.2. Here, the mesh parameters for the first seven cases were chosen by COMSOL. Table 2.2 shows the mesh parameters *viz.* maximum element size (Max. size) that limits how big each element could be, maximum element growth rate (Growth rate) that limits the size difference of two adjacent elements, curvature factor (Curv.factor) that limits how big a mesh element can be along a curved boundary, and resolution of narrow regions (Resolution) that controls the number of layers of mesh elements in a narrow region. As a default, COMSOL used tetrahedral mesh for 3D computational domains and triangular mesh for 2D computational domains.

Coarse meshes took less computational time but resulted in deformation in the shape of the SGNs. For fine meshes, model geometry retained the shape but resulted in a huge number of mesh points; for instance, the extremely fine

TABLE 2.2: Mesh parameters

Mesh id	Mesh type	Max. size	Growth rate	Curv.factor	Resolution
1	Ex.coarse	0.47	1.7	0.8	0.3
2	Coarser	0.371	1.6	0.7	0.4
3	Coarse	0.247	1.5	0.6	0.5
4	Normal	0.198	1.45	0.5	0.6
5	Fine	0.136	1.4	0.4	0.7
6	Finer	0.0865	1.35	0.3	0.85
7	Ex.fine	0.0494	1.3	0.2	1
8	Manual	0.016	1.45	0.5	0.6

mesh resulted in 15 million mesh points. For this reason, manual meshing was considered as the eighth meshing case to optimize the mesh. Setting the minimum mesh element size to one-fourth of the size of the thinnest subdomain and adjusting the remaining mesh parameters accordingly, mesh convergence was studied. Figure 2.7 shows the final mesh obtained by manual meshing (mesh 8). Assuming the solution given by the extremely fine mesh as the best solution, total energy of the system and potential distribution on the middle most SGN were calculated. Figure 2.8 shows relative error ( $\epsilon_{rel}$ ) and absolute error ( $\epsilon_{abs}$ ) in the electric potential which were estimated according to equation (2.17) and equation (2.18)

$$\epsilon_{abs} = \|\phi_{best} - \phi_i\| \quad (2.17)$$

$$\epsilon_{rel} = \frac{\|\phi_{best} - \phi_i\|}{\|\phi_{best}\|} \quad (2.18)$$

where  $\phi_{best}$  is the best solution given by the extremely fine mesh and  $\phi_i$  is the solution given by various indicated meshes.

Figure 2.9 shows the total electric energy solved for the number of degrees of freedom in each mesh case. COMSOL calculates the number of degrees of freedom as the product of the number of nodes and the number of dependent variables of a chosen problem.

Mesh quality was automatically controlled by the software in accordance with the skewness as defined below:

$$\text{Equiangle skewness} = \max \left[ \frac{\theta_{max} - \theta_e}{180 - \theta_e}, \frac{\theta_e - \theta_{min}}{\theta_e} \right]. \quad (2.19)$$



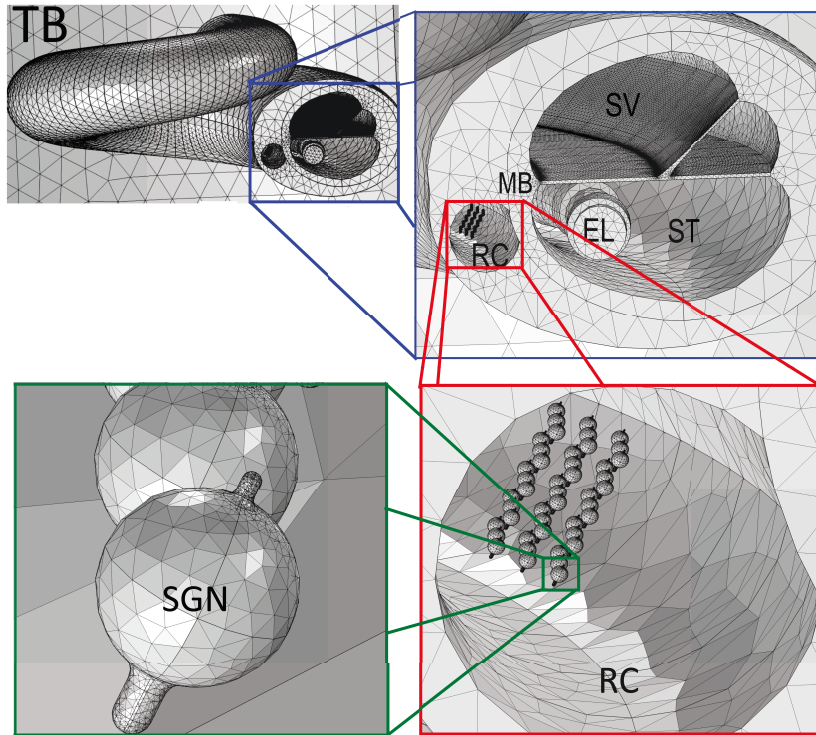


FIGURE 2.7: Finite element mesh obtained by manual meshing (mesh 8) on a 3D computational domain. TB-Temporal bone, MB-modiolus bone, SV-scala vestibuli, ST-scala tympani, EL-electrode, RC-Rosenthal's canal and SGN-spiral ganglion neuron.

where  $\theta_{max}$ ,  $\theta_{min}$  and  $\theta_e$  are the largest angle in the cell, the smallest angle in the cell and the equiangle of the cell, respectively. *Skewness* was plotted for each mesh case as shown in Figure 2.10.

Manual meshing with chosen parameters was considered for the simulations. In the manual meshing case, the relative error was close to that of fine meshing case (mesh 6). The number of mesh elements and computational time were substantially reduced in manual meshing case. Further, a relative error of  $10^{-3}$  magnitude is acceptable, since the electric conductivity values in the model were not accurate more than three decimal places which itself induces an error within the range of the relative error. Further, local mesh refinement was performed manually wherever necessary to improve the element quality.

For 2D computational domain, extremely fine mesh with adaptive mesh refinement was implemented. In this simulation case, mesh convergence study was not carried out as the area of interest for the simulation study was small and computational time was only 5 minutes with extremely fine mesh, and error in the numerical solution was within  $10^{-11}$  magnitude. However, in the case of modeling heterogeneity in the 2D computational domain, it was necessary to seed enough number of mesh points on cell boundaries to retain the realistic micro-anatomy of the spiral ganglion neurons. Automatic meshing option in COMSOL was unable to perform this task. For this reason,

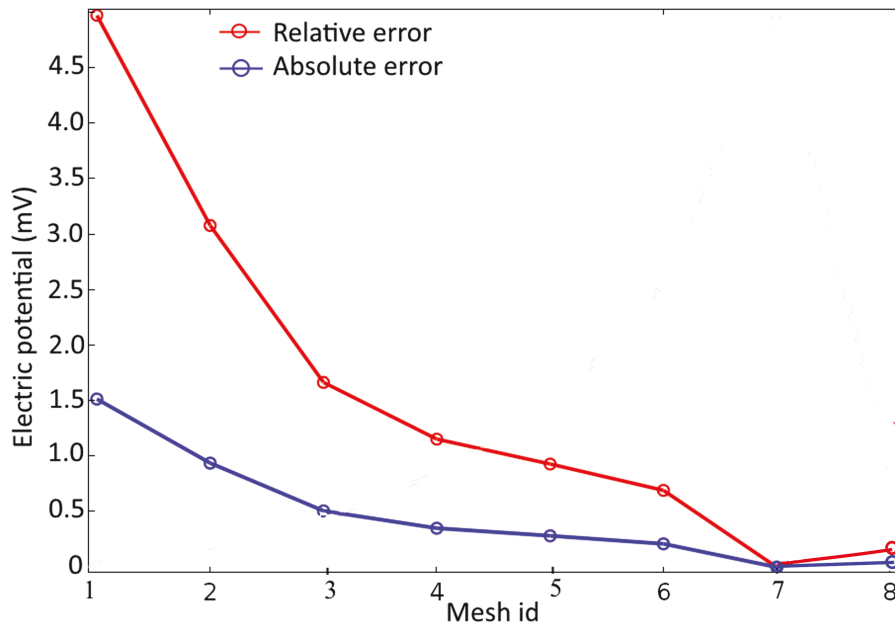


FIGURE 2.8: Absolute error, relative error in electric potential on the middle most SGN estimated for each mesh type in 3D computational domain.

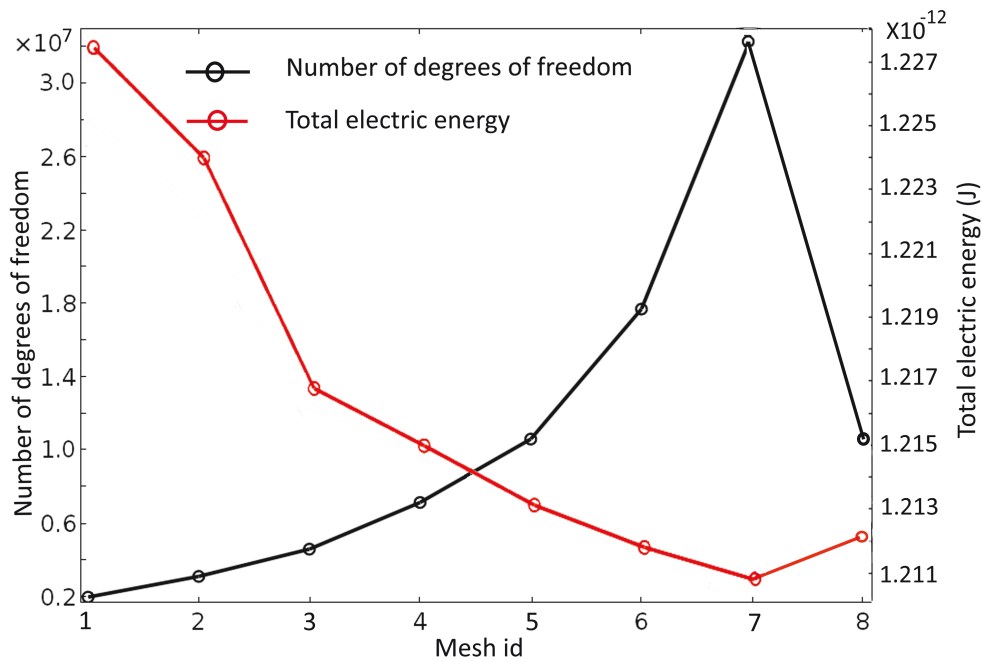


FIGURE 2.9: Total electric energy and respective degrees of freedom for each mesh type in 3D computational domain.

depending upon the topology of the SGNs cell body, required number of mesh points were seeded on the boundaries. Remaining subdomains are meshed by taking these seeded mesh points as reference. Mesh convergence study with different mesh sizes was not performed due to the fixed number

## 2.6. Mesh convergence

---

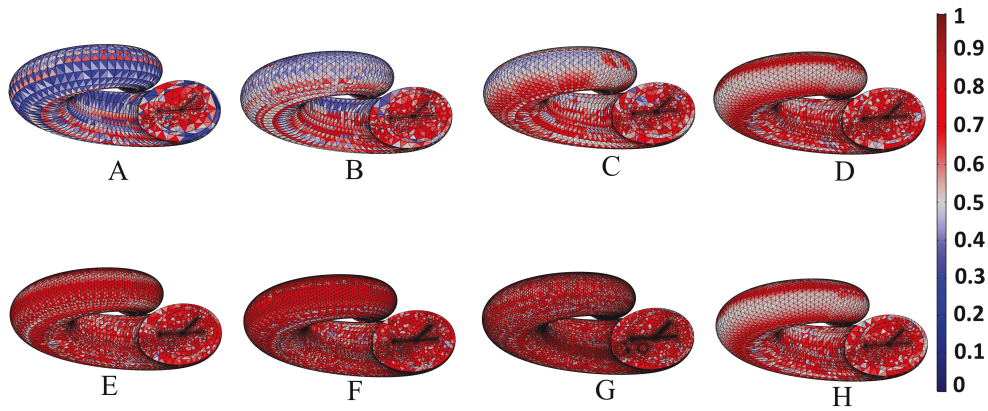


FIGURE 2.10: Color coded representation of skewness for (A) Extremely coarse mesh, (B) Coarser mesh, (C) Coarse mesh, (D) Normal mesh, (E) Fine mesh, (F) Finer mesh, (G) Extremely fine mesh and (H) Manual mesh in 3D computational domain. More than 0.5 skewness value on the scale of 0 to 1 generally indicates good element quality.

of elements on the cell boundaries. However utmost care was taken to avoid the formation of inverted mesh elements. A constraint-based local mesh refinement was performed on the area of interest to minimize the interpolation errors. A convergence study regarding the constraint-based mesh refinement is provided in the related chapter.



## Chapter 3

# Electric Stimulation of Intact SGNs in a Homogeneous Medium

In this chapter, some fundamental concepts and necessary assumptions to estimate the signal initiation sites on the neural membrane are introduced. Various aspects of modeling transmembrane potential of type-1 SGNs in a homogeneous extracellular medium using two-dimensional and three-dimensional finite element models of the cochlea are also presented. The subthreshold response of the SGNs to the applied electric field which was not considered in the existing state-of-the-art *in silico* models is studied. The effects of SGN orientation and cell clustering on the signal initiation are investigated.

### 3.1 Extracellular stimulation of a neural tissue

When a neural membrane is exposed to an external electric field, certain potential difference builds up across the membrane. If the induced transmembrane potential ( $V_m$ ) exceeds the threshold potential, the membrane-specific ion channels initiate the action potentials [82] in the nerve. However, the phase transition of the lipid bilayer of the neural membrane could also evoke the action potential in the nerve [83]. Further, the effectiveness of extracellular stimulation depends on the threshold phenomenon of the targeted neural tissues. However, a thorough correlation between the applied extracellular electric field and the excitation threshold of the neural tissue was not established. Nevertheless, extensive theoretical analysis on the threshold phenomenon is available in the literature [84, 85, 86].

For example, based on the Hodgkin-Huxley model of squid giant axon excitation in space clamp conditions, Plonsey and Barr [87] estimated that the duration of the stimulus should be around 0.25 ms which is equal to the time constant for the opening of sodium ion channels. In the case of short duration stimulation pulses (less than 0.25 ms) it was concluded that the vicinity of the stimulation source plays a prominent role in tissue excitation. Richard FitzHugh [88] presented a detailed phase-plane analysis and classification of the threshold phenomenon based on an 'all or none' response of the excitable tissues. According to FitzHugh, the threshold phenomenon could

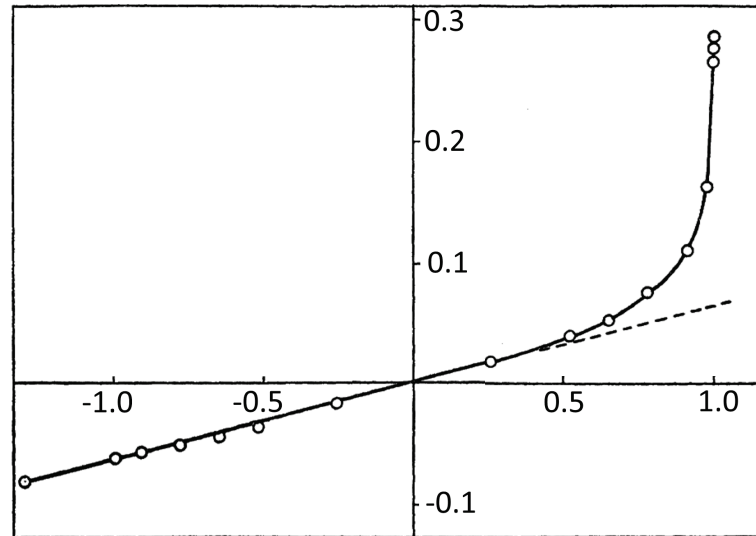


FIGURE 3.1: Relation between the applied stimulus and membrane response in a crab axon. The abscissa shows the stimulus intensity as a fraction of the threshold stimulus and the ordinate shows the membrane potential at 0.29 ms after the stimulus measured as a fraction of the action potential peak. (Picture source: Re-drawn with the permission from Hodgkin AL. 1938. "The subthreshold potentials in a crustacean nerve fiber". Proc R Soc Londaon, Ser B 126:87-121.)

be explained in three categories namely discontinuous, singular-point and quasi-threshold phenomenon.

In general, kinetics of membrane-specific protein ion channels or lipid ion channels [89] determine the neural excitation. However, when a neural membrane encounters the electric field, the ion channels across the membrane would not spontaneously become active. Rather, the neural membrane responds like a thin resistive sheet. It produces a so-called 'polarization potential' until the induced  $V_m$  reaches the threshold value [90] (please refer Figure 3.1). This passive behavior of the membrane in the sub-threshold potential milieu can be exploited in the modeling studies.

### 3.1.1 Activating function

A robust formulation is beneficial in *in silico* studies to predict the activation of neural membrane due to the extracellular stimulation. Frank Rattay proposed the 'activating function' derived from the core conductor cable equation to estimate the site of excitation on the neural tissue [91]. The usefulness of the two approaches namely sub-threshold 'transmembrane potential' and 'activating function' to predict the neural activation was critically examined by Altman, Plonsey and Barr [87, 92]. Derived from the electrical network model of the myelinated nerve, the rate of change of transmembrane potential is given by equation (3.1). Where  $V_m$ ,  $C_m$ ,  $d$ ,  $V_e$  and  $\rho_i$  are transmembrane potential, membrane capacitance, nerve diameter, extracellular potential and intracellular resistivity, respectively. And  $(i_{Na} + i_K + i_L + i_P)_n$  represent the

### 3.2. Modeling transmembrane potential of SGNs in a homogeneous medium

ionic current densities of corresponding sodium, potassium, leakage and unspecific permeability at node  $n$ , respectively.

$$\frac{dV_m}{dt} = \frac{1}{C_m} \left[ \frac{d}{4\rho_i} \left( \frac{\partial^2 V_m}{\partial z^2} + \frac{\partial^2 V_e}{\partial z^2} \right) - (i_{Na} + i_K + i_L + i_P)_n \right] \quad (3.1)$$

The second spatial derivative of the extracellular potential in equation (3.1) was termed as the 'activating function' (AF) denoted by  $A_f(z)$  below,

$$A_f(z) = \frac{\partial^2 V_e}{\partial z^2} \quad (3.2)$$

$$f(V_m(z)) = \frac{\partial^2 V_m}{\partial z^2} \quad (3.3)$$

However, the AF shown in equation (3.2) would predict no activation of nerve in the case of a cylindrical nerve of infinite length exposed to a uniform electric field in a homogeneous medium. Nevertheless, in a realistic biological scenario, nerves have finite dimensions. The active region predicted by the AF on the nerve could serve as an indicative approximation. In equation (3.2) the intracellular potential and the morphology of the nerve have not been considered while defining the AF. AF stands out as a good predictor of the nerve activation in the case of a short stimulating pulse applied by a stimulating electrode in the vicinity of the nerve. However, various other factors such as electrode configuration and its proximity to the membrane, stimulation frequency, dielectric properties of the extracellular medium and the active neural tissues characterize the electric field distribution and thereby the activation of the targeted nerve.

Whereas equation (3.3) shows the functional input of the transmembrane potential in equation (3.1) which is an inherent result of the membrane thickness, intracellular potential, nerve morphology and extracellular medium. In other words, unlike the AF, the sub-threshold transmembrane potential represents the actual response of the cell to the applied electric field. Figure 3.2 shows the ratio of AF and subthreshold transmembrane potential against the distance of the stimulating electrode. The subthreshold transmembrane potential is a good predictor of the signal initiation site on the neural membrane where the AF fails to predict the activation of the nerve accurately.

## 3.2 Modeling transmembrane potential of SGNs in a homogeneous medium

Almost all *in silico* models discussed in Chapter 2 have assumed a homogeneous medium in the Rosenthal's canal (RC) to model the electric stimulation of the auditory nerve. It is noteworthy from the literature that the role played by the induced  $V_m$  of SGNs in the context of signal initiation sites on the auditory nerve was not studied explicitly. Moreover, signal initiation sites on the auditory nerve were not known in the case of amputated peripheral

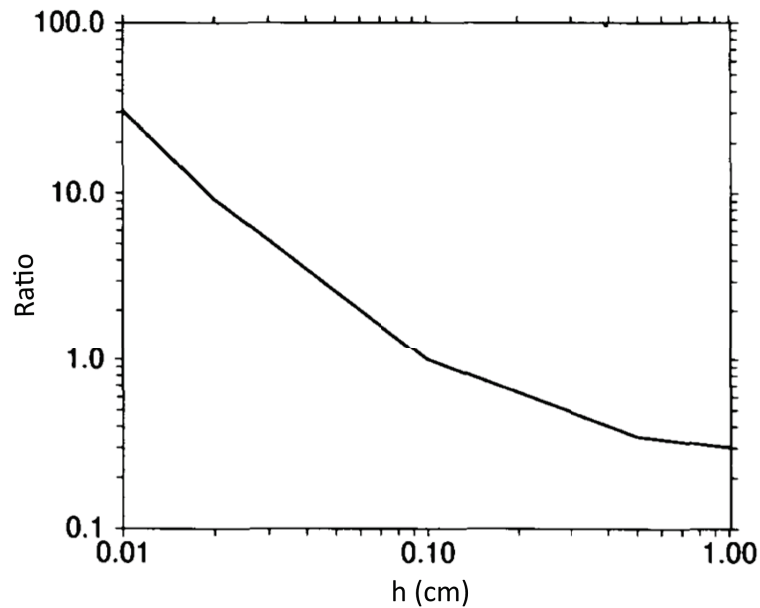


FIGURE 3.2: Ratio of the AF to the maximal transmembrane potential. The ratio is plotted as a function of distance  $h$  of the stimulus electrode from the fiber on the log scale. If the AF were an ideal predictor, the ratio would be a horizontal line through Ratio = 1. (Picture source: Reused with the permission from R. Plonsey and R. C. Barr, "Electric field stimulation of excitable tissue," in *IEEE Transactions on Biomedical Engineering*, vol. 42, no. 4, pp. 329-336, April 1995.)

axons [93]. However, experimental studies and modeling studies speculate that the signal initiation most probably takes place on the cell body or the peripheral axonal initial segment of the auditory nerve [65, 94, 95, 96, 97]. This implies that an SGN cell body with only intact AIS as shown in Figure 3.3 assumed to be good enough to model the location of signal initiation sites on the auditory nerve.

### 3.2.1 Model geometry

Modeling a realistic cochlear geometry from  $\mu$ CT or MRI data retains the morphometry of the cochlea. However, delineating complicated anatomy through simplified geometry is a necessary evil in mathematical modeling. Especially in the case of modeling the human cochlea, a 'benchmark' cochlear geometry to suit all modeling scenarios is implausible. Since the anatomical variations of the cochlea is highly discordant from subject to subject [27], the patient-specific *in silico* models becoming more relevant [98]. Geometrical considerations in modeling depend typically on the aim of the study. For example, a realistic geometry of the cochlea is essential to investigate the hydrodynamics of the basilar membrane, as the results exclusively depend on the volume of the scala chambers. Likewise, realistic cochlear geometry is a prerequisite to model the electrode insertion trauma, since the so-called 'bottleneck' region in the scala tympani is crucial for atraumatic insertion [99, 100].



### 3.2. Modeling transmembrane potential of SGNs in a homogeneous medium

Further, to model the electric stimulation of auditory nerve by cochlear implants, a realistic cochlear geometry is especially essential to simulate the monopolar stimulation case. Since the counter electrode is usually placed far from the active electrode, the curvature of the scala chambers in general, and the morphometry of the scala tympani, in particular, provide an arbitrary path for the injected current to reach the counter electrode which in turn affects the field distribution and neural activation [101].

However, in the case of bipolar stimulation two adjacent electrodes act as active and counter electrodes in the scala tympani. Since the injected current chooses the shortest and less resistive path to reach the counter electrode, the resultant electric field tend to confine to a small region. This confinement, in turn, enables the selective stimulation of spiral ganglion neurons. In this particular case, dielectric properties of the tissues involved predominantly influence the electric field distribution compared to that of the anatomy of bony labyrinth of the cochlea [102].

Present study considered the bipolar electric stimulation of spiral ganglion neurons in the Rosenthal's canal at the basal region of the cochlea. A two-dimensional geometry of the area of interest as shown in Figure 3.4 has been modeled within the framework of following assumptions.

1. A longitudinal section of the cochlea formed by a plane connecting the central planes of the scala tympani, spiral ganglion cell bodies, and the electrode pads has been considered.
2. The hard bony capsule and the basilar membrane offer higher resistance compared to that of the extracellular medium and the porous modiolus.
3. The type-1 spiral ganglion cell body with intact AIS was modeled as a circle attached with two thin rectangles at diametrically opposite points as shown in Figure 3.3.

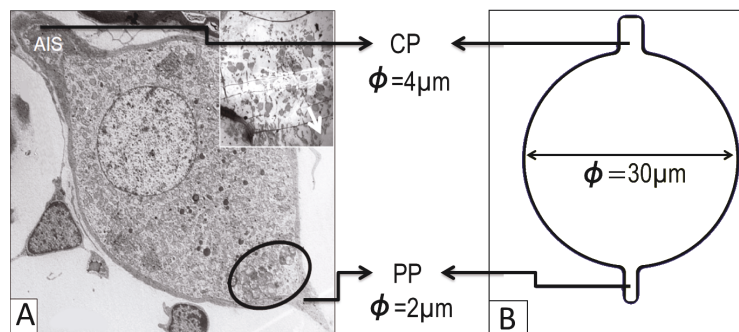


FIGURE 3.3: Spiral ganglion neuron model, (A) Type I SGN with accumulation of intracytoplasmic inclusion bodies in the distal pole. AIS - axonal initial segment. Inset shows marked region at low magnification. *Picture source: Taken from [93] and re-used with the permissions.* (B) Simplified two dimensional model of SGN with AIS. PP - Peripheral process, CP - Central process,  $\phi$  - diameter of the corresponding component.

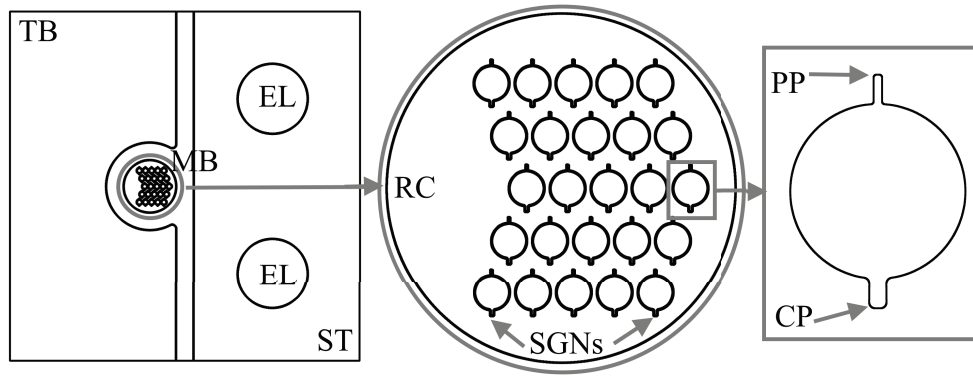


FIGURE 3.4: A simplified 2D computational domain of the area of interest used for the simulation. TB - Temporal bone, MB - Modiolus bone, EL - Electrodes, RC- Rosenthal's canal, SGNs - Spiral ganglion neurons, ST - Scala tympani, CP - Central processes, PP - Peripheral processes.

Table 3.1 shows the dimensions of the modeled subdomains. Above model assumptions also suffice the inclusion of only basal turn geometry to capture the simulation scenario in 3D. Instead of modeling all two and a half turns of the cochlea, inclusion of only the volume of interest curtails the computational cost without losing the generality of the problem. The simplified three-dimensional geometry of the bony labyrinth enclosing the scala tympani, the scala media, the scala vestibule, the basilar membrane, the Reissner's membrane, the spiral ligament and the modiolus bone in a cylindrical temporal bone was constructed using COMSOL modeling interface. The typical snail shape of the cochlea was constructed based on the parametric curve defined by the following spatial coordinates:

$$x = \exp(0.25\theta) \cos(2.25\theta) \quad (3.4)$$

$$y = \exp(0.25\theta) \sin(2.25\theta) \quad (3.5)$$

$$z = \exp(0.25\theta) \quad (3.6)$$

Here  $\theta$  takes values from 0 to  $2\pi$ . The resultant geometry was scaled down to the range of realistic dimensions as shown in Figure 3.5. Out of two and a half turns, slightly more than one turn of the basal region was considered for the simulations as shown in Figure 3.6. This volume encloses the full electrode length which represents 400 degrees of electrode insertion depth. However, the resultant three-dimensional geometry of the cochlea could not accurately replicate the morphometry of the human cochlea. Nevertheless, the parametric model has been constructed in such a way that the modiolus and the RC are compliant with the study-specific modifications such as the implementation of the porosity and tissue heterogeneity. Hence, the parametric model of the cochlea has been used for the simulations.

<sup>1</sup>This realistic model was constructed as a part of Wissenschaftlicher Hilfe (WiHi) by Karthik Sridhar. However, the Rosenthal's canal and the SGNs could not be constructed with the available MRI data. Hence, the model was not used for simulations.

### 3.2. Modeling transmembrane potential of SGNs in a homogeneous medium

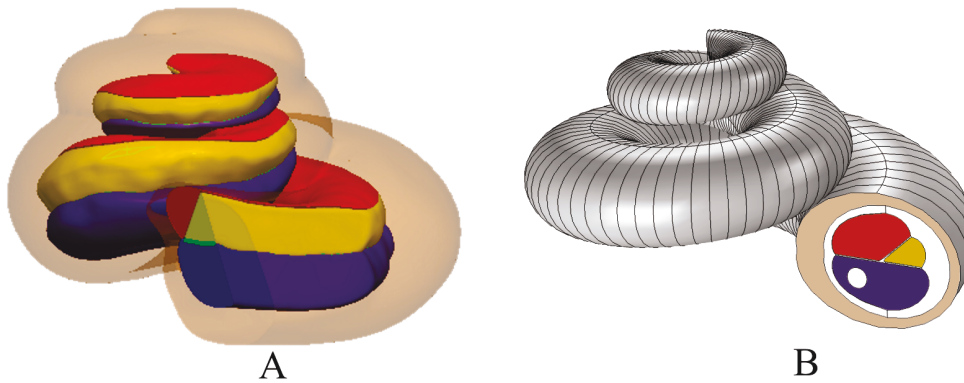


FIGURE 3.5: (A) 3D cochlea model constructed from MRI data<sup>1</sup>, (B) 3D parametric model of human cochlea scaled to the range of realistic dimensions. Color code of scala chambers: red-scala vestibule, yellow-scala medium, blue-scala tympani.

TABLE 3.1: Dimensions of computational subdomains

Subdomain	Dimensions
Temporal bone	0.5 cm $\times$ 0.5 cm
Modiolus bone	100 $\mu$ m $\times$ 2 mm
Electrode	0.3 mm (diameter)
Scala tympani	1 mm $\times$ 1 mm
Rosenthal's canal	250 $\mu$ m (diameter)
Spiral ganglion neurons	30 $\mu$ m (diameter)
Central processes	4 $\mu$ m (diameter)
Peripheral processes	2 $\mu$ m (diameter)

#### 3.2.2 Transmembrane potential

A sufficiently high electric field induces a certain potential difference across the membrane of a biological cell. The difference between the intracellular potential and the extracellular potential is termed as transmembrane potential ( $V_m$ ) of that cell.

$$V_m = V_{int} - V_{ext} \quad (3.7)$$

The transmembrane potential at any point on the cell membrane in a homogeneous electric field can be expressed analytically by Schwan equation [103,

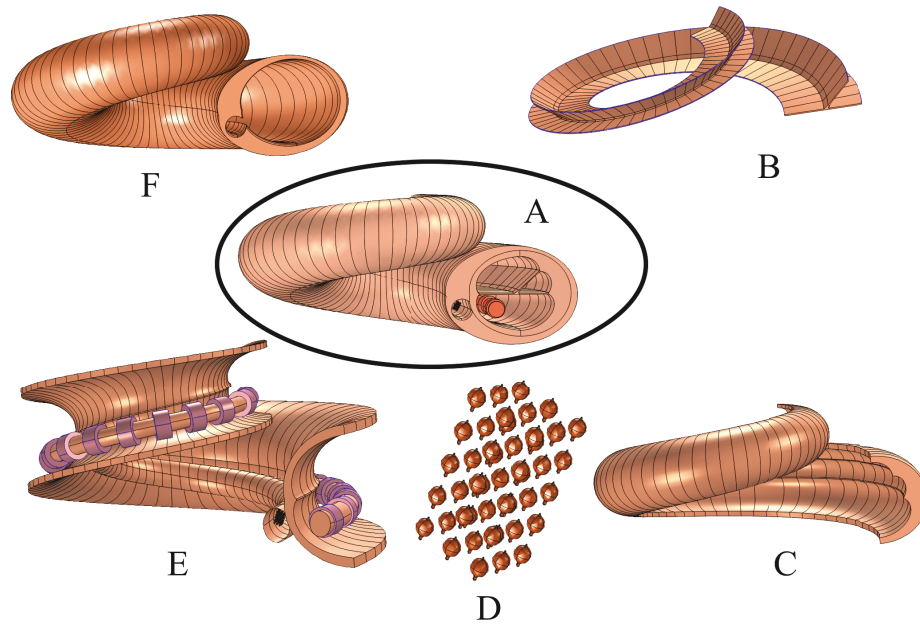


FIGURE 3.6: Exploded view of 3D model of the human cochlea. (A) 3D computational domain, (B) Basilar and Reissner's membranes, (C) Spiral ligament, (D) Spiral ganglion neurons in the RC, (E) Modiolus bone and cochlear implant electrode, (F) Surrounding bone.

104]

$$V_m = AEr \cos \theta \quad (3.8)$$

Here  $A$  is the *cell constant* which depends on the cell shape and size, while  $E$ ,  $r$ , and  $\theta$  are the applied electric field, cell radius and cell orientation with the field respectively. Detailed descriptions and various analytic models of the transmembrane potential can be found in [105, 106, 107].

### 3.2.3 Boundary conditions

Suitable boundary conditions are a prerequisite to approximate reasonably accurate numerical solution. One persistent problem in the *in silico* modeling of auditory nerve stimulation is assigning proper boundary conditions to the outer boundaries of the domain, especially in monopolar electrode configuration case [101]. In the monopolar stimulation, the counter electrode is situated at the outer layer of the skull. Therefore the large volume of the head and other tissues should be included in the model. Modeling all those tissues not only demands substantial computational cost but also induces modeling inaccuracies. For example, it is not always possible to assume the continuity boundary condition at the interface of different tissues, since many active tissues such as the optical nerve and facial nerve and blood vessels are present at the vicinity of the cochlea [101]. To overcome this issue, a recent *in silico* model followed the multiscale modeling approach to approximate the

### 3.2. Modeling transmembrane potential of SGNs in a homogeneous medium

resultant potential on the nearest bone volume [108]. However, in the case of bipolar stimulation where the electric field distribution tends to confine in a relatively small volume, it is safe to assign following boundary conditions.

- *Electric insulation boundary condition* was assigned to all outer boundaries.

$$\mathbf{n} \cdot \mathbf{J} = 0 \quad (3.9)$$

where  $\mathbf{n}$  is the unit normal vector and  $\mathbf{J}$  is the current density.

- *Continuity boundary condition* was assigned to all interior boundaries except on the boundaries of spiral ganglion neurons and AIS.

$$\mathbf{n} \cdot (\mathbf{J}_1 - \mathbf{J}_2) = 0 \quad (3.10)$$

where  $\mathbf{J}_1$  and  $\mathbf{J}_2$  are the current densities on either side of the selected boundaries, respectively.

- The thickness of the spiral ganglion neuronal membrane is approximately 10 nm which is extremely difficult to model as a computational subdomain. Comparing with the dimensions of the model geometry the discretization of this nanoscale membrane demands an unprecedented number of mesh elements. One elegant way would be using thin film approximation available in COMSOL as *contact impedance boundary condition*.

$$\begin{aligned} \mathbf{n} \cdot \mathbf{J}_{int} &= \sigma(V_{int} - V_{ext})/d \\ \mathbf{n} \cdot \mathbf{J}_{ext} &= \sigma(V_{ext} - V_{int})/d \end{aligned} \quad (3.11)$$

Here  $V$ ,  $\mathbf{J}$ ,  $\sigma$  and  $d$  represent the electric potential, current density and electric conductivity of the cell membrane respectively. The subscripts *int* and *ext* indicate the *internal* and *external* side of the cell membrane, respectively. On one electrode 150  $\mu\text{A}$  input current was applied and on the other electrode ground boundary condition was applied.

A comparative study has been carried out to check the correctness of the *contact impedance boundary condition* against the analytical solution and the solution obtained by physical modeling of the thin membrane.

#### 3.2.4 Thin film approximation of the membrane

The present study aims to model the subthreshold transmembrane potential of SGNs induced by the extracellular stimulation in a homogeneous medium. In such case, the cell membrane can be assumed as a thin resistive sheet. A cell membrane can be modeled as a thin resistive sheet if it satisfies two conditions. Firstly, the activation time constant should be larger than the effective time constant of the membrane, and secondly, the stimulation duration should be larger than the activation time constant [87]. The transmembrane potential of

a cell modeled under these conditions not only reduces the mathematical complexity but also provides a theoretical basis to estimate the site of excitation. Hence, the analysis of induced  $V_m$  across the passive membrane would be a good approach to obtain considerable knowledge about the active membrane behavior.

As a proof of concept, a spherical cell of  $30 \mu\text{m}$  diameter which is equal to the diameter of the spiral ganglion neuron at the basal region of the cochlea was modeled in a homogeneous extracellular medium. The induced  $V_m$  was calculated in three possible cases. In the first case, a  $10 \text{ nm}$  thin membrane geometry was modeled. In the second case, the cell membrane was modeled with the thin-film approximation. In the third case, the transmembrane potential was approximated using equation (3.8). The maximal transmembrane potential was almost equal in all three cases (please refer Figure 3.7). Later, a spiral ganglion neuron with intact axon initial segments was modeled, and the induced  $V_m$  was calculated using thin-film approximation. The effect of the geometry of AIS on the induced maximal transmembrane potential was found to be negligible.

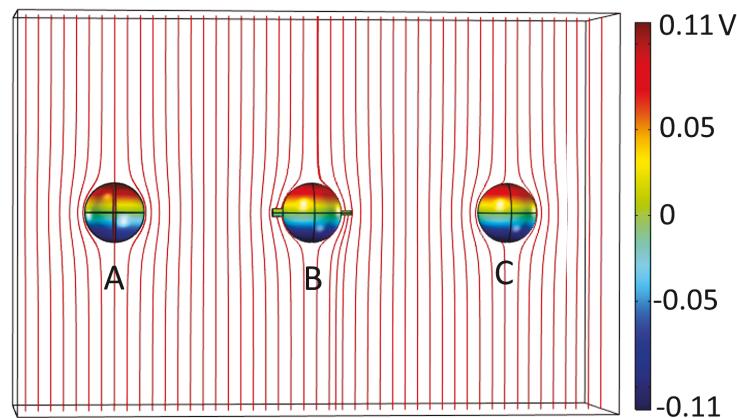


FIGURE 3.7: Comparison of induced maximal transmembrane potential for three modeling cases, (A)  $10 \text{ nm}$  thin neural membrane induced  $0.113 \text{ V}$ , (B) Spiral ganglion neuron with initial segments induced  $0.11312 \text{ V}$ , (C) Cell membrane modeled with thin film approximation induced  $0.11299 \text{ V}$ . Deviation of electric field lines (red lines) can be seen at the curvature of the cell membrane.

The thin film approximation is defined by equation (3.11) in COMSOL. The maximal transmembrane potential induced on a spherical cell of  $15 \mu\text{m}$  radius ( $r$ ) was calculated analytically using equation (3.8) also known as Schwan equation [109, 110] for frequency-independent medium. Here substituting  $A= 1.5$  (cell constant for spherical cell),  $E= 5020 \text{ V/m}$  (uniform electric field induced by  $1 \text{ V}$  potential applied on the electrode) and  $\theta= 0^\circ$  (angle between measuring point and the electric field) in equation (3.8) yields a maximal transmembrane potential  $V_m= 0.1129 \text{ V}$ . Above results suggest that the contact impedance boundary condition could approximate a thin neural membrane considerably well.

### 3.2.5 Dielectric properties of biological tissues

Indistinct electric conductivity values of the biological tissues related to human cochlea are available in the literature. Notably, most of those values are manipulated to fit the concerned study cases [102]. A compendium of available dielectric properties of cochlear tissues used in some state-of-the-art *in silico* models is given in Table 3.2. Re-scaling the conductivity values to match the model geometry, stimulus frequency, and sampling techniques could be the main reason for discrepancies in the reported conductivity values. The inclusion of uncertain material properties in the model could result in irrational model output [111].

TABLE 3.2: Electric conductivity of biological tissues

Tissue		Conductivity (S/m)
Bone components	Temporal bone	0.02 <sup>a</sup> , 0.016 <sup>g</sup>
	Modiolar bone	0.2 <sup>a</sup> , 0.085 <sup>c</sup>
	Skull	0.073 <sup>c</sup>
	Lateral wall	0.156 <sup>c,d,f,h,j</sup> , 0.159 <sup>b</sup>
	Otic capsule	0.008 <sup>d</sup>
	Compact bone	0.06 <sup>e</sup>
	Soft bone	0.04 <sup>e</sup>
Neural components	Auditory nerve	0.334 <sup>a,b,d,f,g,i</sup>
	Spiral ganglion	0.334 <sup>b,c</sup>
	Brain gray matter	0.34 <sup>e</sup>
	Brain white matter	0.143 <sup>e</sup>
	Myelinated tissues	$3.45 \times 10^{-6l}$
	Satellite glial cells	$4 \times 10^{-8m}$
Membranes	Basilar membrane	0.005 <sup>a</sup> , 0.056 <sup>b</sup> , 0.0625 <sup>d</sup> , 0.25 <sup>f</sup> , 0.027 <sup>j</sup>
	Reissner's membrane	0.005 <sup>a</sup> , 0.0016 <sup>b</sup> , 0.0029 <sup>f</sup> , 0.002 <sup>j</sup>
Other components	Spiral ligament	0.334 <sup>a</sup> , 0.599 <sup>d</sup>
	Perilymph	0.476 <sup>k</sup> , 2 <sup>a</sup> , 0.699 <sup>d</sup> , 1.43 <sup>b,f,g,h,j</sup>
	Endolymph	2 <sup>a,i</sup> , 1.67 <sup>b,f,g,h,j</sup> , 0.599 <sup>d</sup>
	Cerebrospinal fluid	1.538 <sup>e</sup>

<sup>a</sup>[58], <sup>b</sup>[59], <sup>c</sup>[55], <sup>d</sup>[61], <sup>e</sup>[112], <sup>f</sup>[64], <sup>g</sup>[65], <sup>h</sup>[70], <sup>i</sup>[72], <sup>j</sup>[73], <sup>k</sup>[31], <sup>l</sup> [113], <sup>m</sup>[114]

### 3.3 Simulation

All simulations in the present study were performed using the AC/DC module in COMSOL software. Model equations were solved using the multifrontal massively parallel sparse direct solver (MUMPS) unless otherwise mentioned separately. MUMPS is designed for parallel factorization and iterative refinement with backward error analysis of large sparse systems of linear algebraic equations [115].

The problem was solved for 172,178 degrees of freedom using the stationary solver and MUMPS. The final solution was accepted with the error of  $10^{-9}$  magnitude. All simulations were performed on the windows server work station with 64-Bit Intel(R) Xenon(R) CPU with 3.40 GHz (two processors) with 256 GB RAM.

Simulation results for the two-dimensional computational domain (2D) and the three-dimensional computational domain (3D) are discussed in the following sections.

#### 3.3.1 2D results

The electric potential distribution in the 2D computational domain is shown in Figure 3.8. For the present simulation scenario, RC is exposed to a minimum of 0.429 V to the maximum of 0.446 V. Although SGNs have same shape and size, the variance in the potential distribution and the spatial arrangement of SGNs in the RC have induced cell-specific transmembrane potentials. The variance in the maximal transmembrane potential is proportional to the distance between SGNs and the electrode. Since SGNs are modeled a few micrometers apart from each other, the maximal transmembrane potential induced on each SGN has not significantly varied.

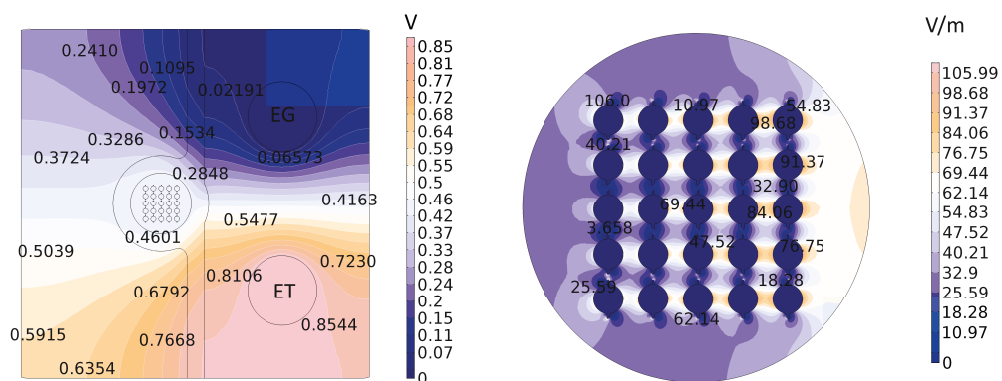


FIGURE 3.8: Contours of voltage distribution in the computational domain (left) and the contours of electric field distribution in the RC (right). ET - active electrode assigned with  $150 \mu\text{A}$  current, EG - counter electrode assigned with ground.

Figure 3.9 shows the transmembrane potential of indicated SGNs. Maximal transmembrane potential induced on the most proximal SGNs was 1.4 mV



(Figure 3.9 (D)) and that on the distal SGNs was 1 mV (Figure 3.9 (B)). The vertical arrangement of SGNs within a given distance from the electrode would not profoundly affect the SGN stimulation profile. However, the case of the horizontal spatial variance of SGNs from the electrode shows a considerable effect on the induced  $V_m$  (Figure 3.9 (A) and (C)). The maximal transmembrane potential induced on the second layer of SGNs (C17 to C25) is within 1.2 mV (Figure 3.9 (E)). In this specific simulation scenario, the AIS were aligned parallel to the line joining the geometric center of two electrodes. The electric field lines passing through the RC run parallel to the AIS of the SGNs as shown in Figure 3.10 (A). As a consequence, the maximal transmembrane potential is induced on the AIS of every SGN which is consistent with equation (3.8). In this simulation case, the AF also reached the maximum positive value at the same location where the induced  $V_m$  has maximal value (please refer Figure 3.10). The cumulative results suggest that the signal initiation can take place on the AIS. These results also show the sensitivity of spatial arrangement of SGNs to the electric stimulation.

#### 3.3.2 Effect of SGN orientation on the signal initiation sites

Morphological studies suggest that the SGNs seldom have a symmetrical arrangement in the RC. For example, in [93] the authors published a series of pictures obtained by scanning electron microscopy (SEM) and immunohistochemistry of SGNs that shows the random arrangement of SGNs (Figure 3.11). To study the effect of SGN orientation on the signal initiation sites, two more simulation cases in which two possible orientation angles  $45^\circ$  and  $90^\circ$  made by AIS with the line joining the geometric center of two electrodes were assumed. Simulation results of those two cases are shown in Figure 3.12 and Figure 3.13. In the second and third simulation cases, the location where the induced  $V_m$  on each SGN is maximal does not coincide with the location where the AF is maximum.

These results are prominent in two different perspectives. In the modeling perspective, signal initiation sites predicted by the AF may not necessarily comply with the realistic scenario. For example, in the second and third simulation cases the AF has predicted the signal initiation sites on the AIS irrespective of SGN orientation (please refer Figure 3.12 and Figure 3.13). The maximal value of the AF indicates the probability of signal initiation at the area of interest. This could happen due to the heterogeneous material properties of the medium. This could also occur due to the presence of rough and irregular geometrical shapes in the model where the electric field intensity tends to be higher. For this reason, the AF would always reach its maximum value at thin AIS. However, this inherent drawback of AF has a surprising advantage regarding the physiology of the neural membrane. Experimental studies [65, 116, 117] arguably suggest that the density of voltage-dependent sodium ion channels (Nav) on the AIS is 50 times higher than that of the soma. These Nav channels lower the activation threshold and thereby initiate the action potential on the axonal initial segment. Henceforth, irrespective of all other cell properties, the probability of signal initiation on the AIS is higher

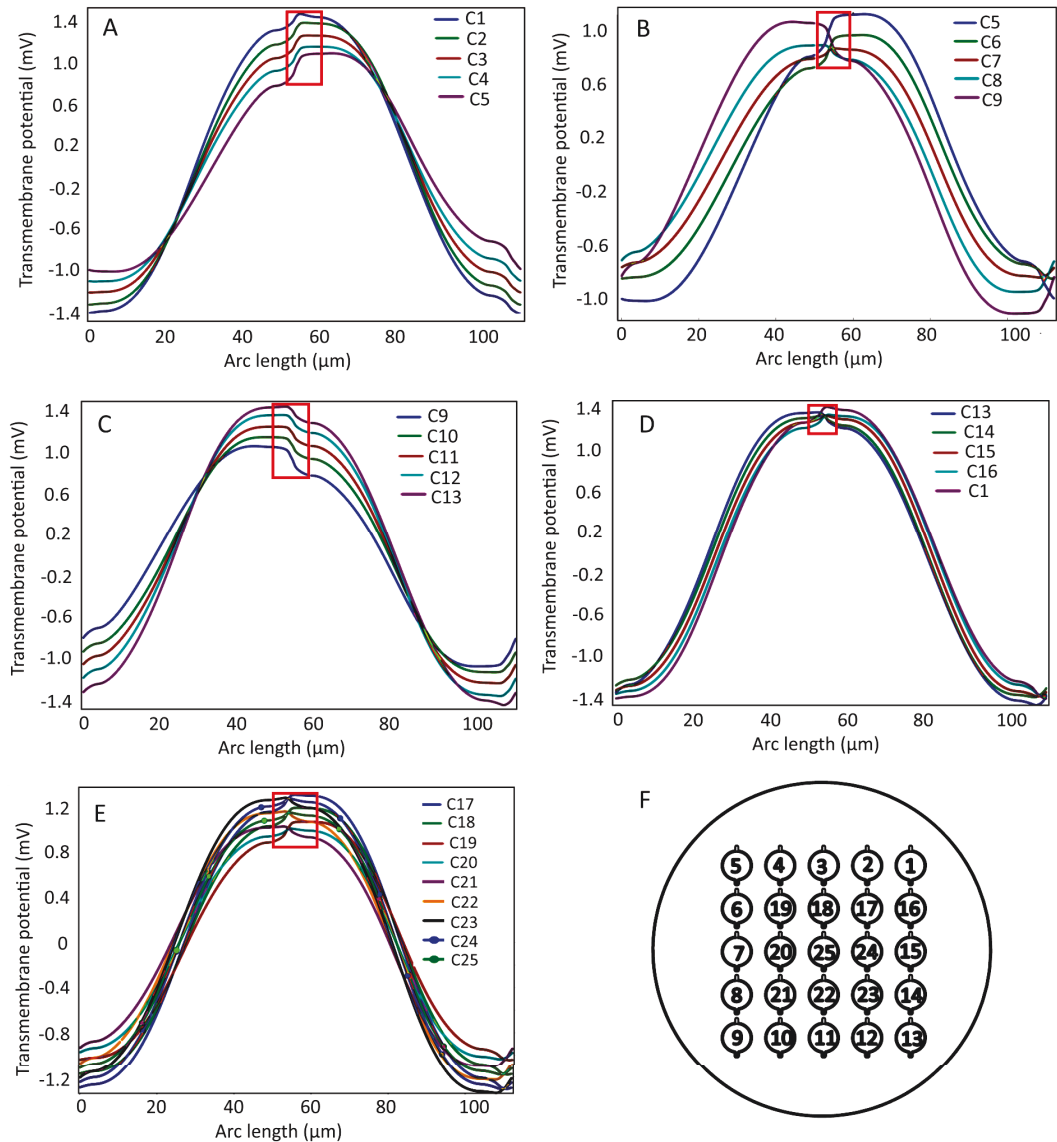


FIGURE 3.9: (A)–(E) The induced  $V_m$  of indicated SGNs (C1-C25). (F) C1 through C25 represent the SGN reference numbers. Red boxes indicate the location of AIS.

than the probability of signal initiation on the cell body. Strikingly, AF predicts the same for cat and guinea pig myelinated auditory nerve models [65, 118].

However, above argument may not be appropriate for the unmyelinated axons. The density of Nav channels on the AIS is reported to be only five times higher than that on the soma [119, 120]. On the other hand, Kole and group [95] reported through the patch clamp experiments that the density of Nav channels on the soma and its AIS was almost equal. Since the activation threshold varies logarithmically with the density of the Nav channels [121], the activation threshold of intact AIS would be within the comparable magnitude to that of the unmyelinated soma. In other words, the effect of 50 times higher Nav ion channel density on lowering the activation threshold of the AIS could not be the same with only five times higher Nav channel density.

### 3.3. Simulation

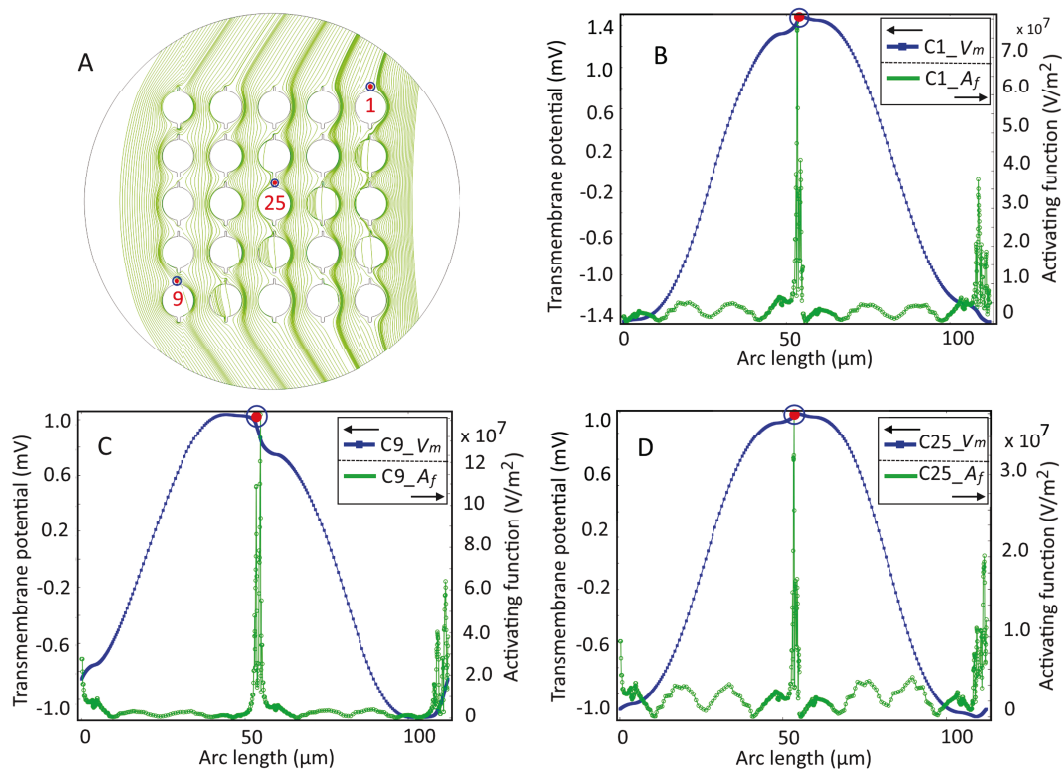


FIGURE 3.10: (A)–(D) Sites of maximal transmembrane potential ( $V_m$ –blue circles) and maximal value of the AF ( $A_f$ –red dots) on indicated SGNs. Electric field lines are shown in green in (A)

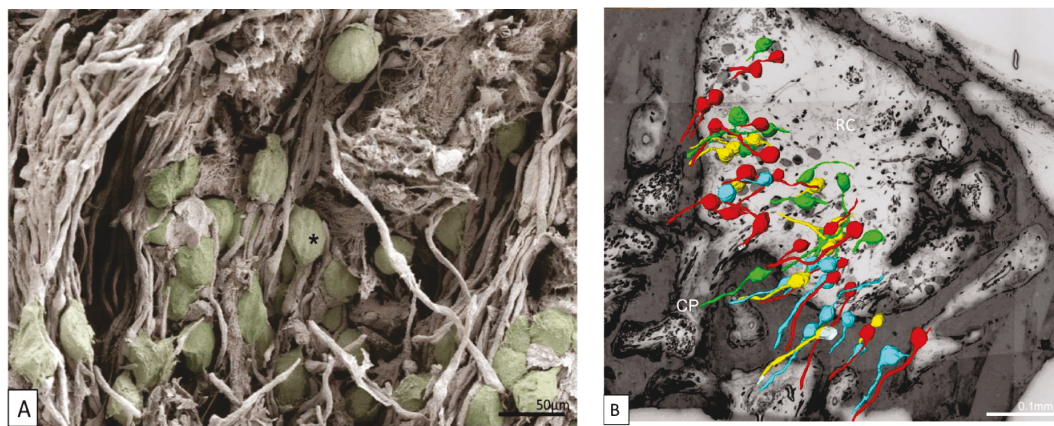


FIGURE 3.11: Random orientation of SGNs in the RC. (A) Scanning electron microscopy of human spiral ganglion in basal turn. Neural cell bodies have been artificially stained green. (B) Light microscopy of the SGNs from a damaged region where SGNs are depicted in arbitrary colors. RC–Rosenthal’s canal, CP–Central processes. (Picture source: Taken from [93] with the permissions.)

Even though the central axons of the amputated auditory nerve in humans are myelinated, the SGNs cell bodies are unmyelinated. Therefore one can assume the feasibility of signal initiation on the cell body which is consistent with

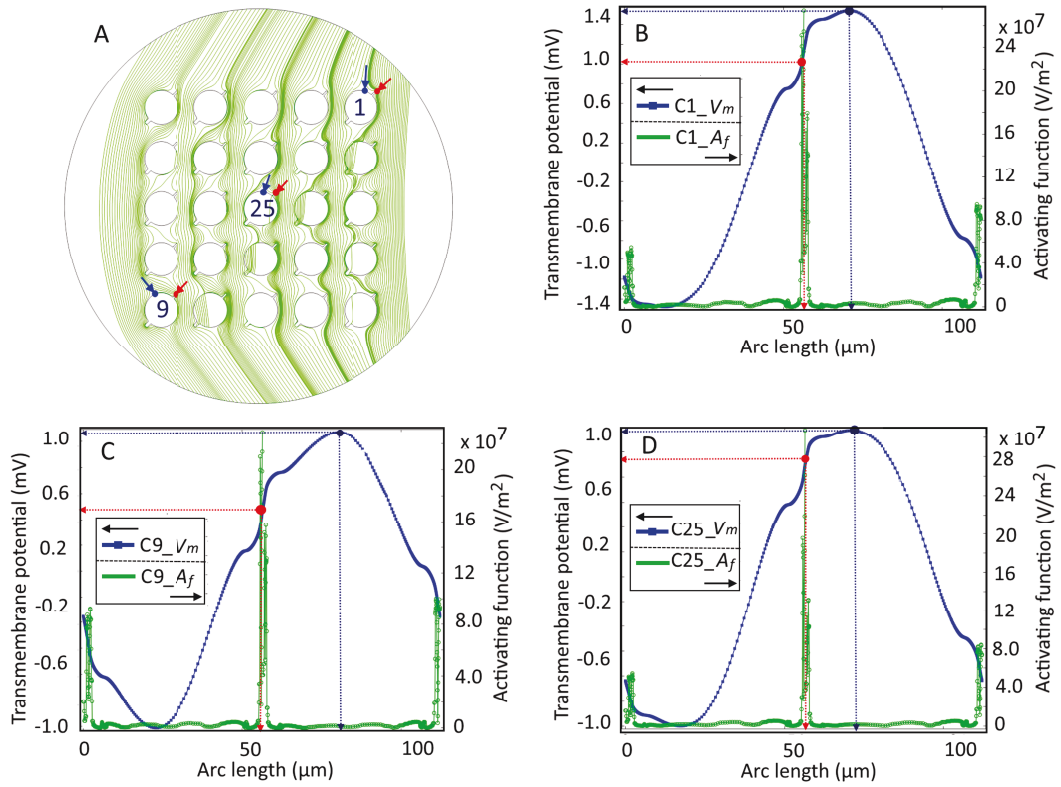


FIGURE 3.12: (A)–(D) Sites of maximal transmembrane potential ( $V_m$ –blue dot and arrows) and maximal value of the AF ( $A_f$ –red dot and arrows) on the indicated SGNs for  $45^\circ$  orientation. It is observable that the  $V_m$  is not reached its maximal value at the signal initiation sites predicted by the AF.

multiple signal initiation sites reported in [94]. In this context, the prediction of signal initiation sites on SGNs with respect to the maximal transmembrane potential would be realistic.

In the sub-threshold voltage perspective, experimental studies suggest that most of the sodium ion channels stay inactive until the sub-threshold potential induced by external electric stimulation reaches at least 80 percent of required activation threshold (Figure 3.1). For example, in Figure 3.12 (B) the sub-threshold transmembrane potentials induced on the cell body and on the axonal initial segment were 1.5 mV and 1 mV, respectively. The sub-threshold potentials should be a little less than 80 percent of the required activation threshold. In this instance, the activating threshold should be at least 2 mV. Hence the density of Nav ion channels should be much higher than that of cell soma to reduce the activation threshold of AIS at least by 50 percent for signal initiation. In any case, lowering the activation threshold of AIS does not alter the induced maximal transmembrane potential of the cell soma. This implies that the propagating signal through the AIS experiences very strong hyper and depolarized regions of the soma. In this scenario, the cell soma typically blocks the action potential propagation [65, 122, 123]. For the safe propagation of action potential through the cell soma, the maximal transmembrane potential

### 3.3. Simulation

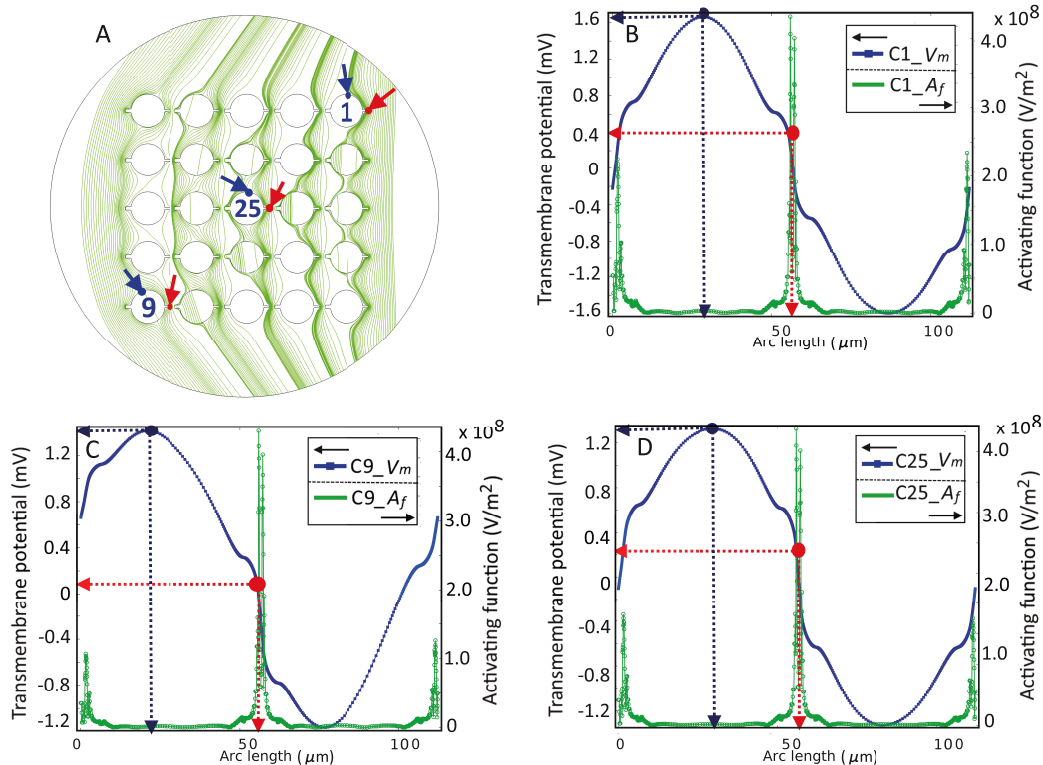


FIGURE 3.13: (A)–(D) Sites of maximal transmembrane potential ( $V_m$ —blue dot and arrows) and maximal value of the AF ( $A_f$ —red dot and arrows) on indicated SGNs for  $90^\circ$  orientation. The AF predicts the signal initiation at the AIS even though the maximal  $V_m$  is induced on the cell soma.

need to be induced on or near the AIS. The orientation of SGNs concerning the electric field lines could favor the signal initiation and propagation in the auditory nerve.

#### 3.3.3 Spiral ganglion neuronal clusters

Several SGN cell clusters in the RC have been observed in morphological studies of human temporal bones [93]. Two or three SGNs in each cluster share a common membrane at their inner boundaries. Interestingly, the cell clusters are predominant in older people. The role of these cell clusters in the auditory transduction is not explored thoroughly. However, since the speed of nerve impulse is proportional to the volume of the neuronal cell body, some *in silico* models suggest that the cell clusters probably regulate the temporal component of the nerve signal during the auditory transduction [124, 125].

In this context, the effect of cell clustering on the signal initiation and propagation is studied using a two dimensional computational model of the RC. Signal initiation and propagation in the SGNs is modeled using the FitzHugh-Nagumo (FHN) electric impulse model [126, 127]. FHN equations qualitatively replicate the electrical activity of the action potential. In FHN equations,

the generation and propagation of action potential is described through an excitation variable ( $V$ ) which is analogous to the transmembrane potential, and the recovery variable ( $U$ ) as shown in equation (3.12).

$$\begin{aligned}\frac{\partial V}{\partial t} &= \Delta V + V(a - V)(V - 1) - U \\ \frac{\partial U}{\partial t} &= e(bV - cU - d)\end{aligned}\tag{3.12}$$

The detailed description of the dynamics of FHN equations such as phase plane analysis is beyond the scope of the present study. For further details of FHN based models, please refer [128, 129]. The description and the values of system parameters  $a, b, c, d$ , and  $e$  in FHN equations are shown in table 3.3 (taken from [128]). The maximal induced  $V_m$  on each SGN is taken as the initial values of  $V$ . A threshold voltage of 1.4 mV is fixed as an activation constraint on the membrane of each SGN. This constraints the SGNs from firing the action potentials unless the induced  $V_m$  on an SGN crosses 1.4 mV. The signal initiation site is assumed as a point where the induced  $V_m$  is maximal on an SGN. This assumption is useful to investigate the effect of clustering on the external stimulation of SGNs.

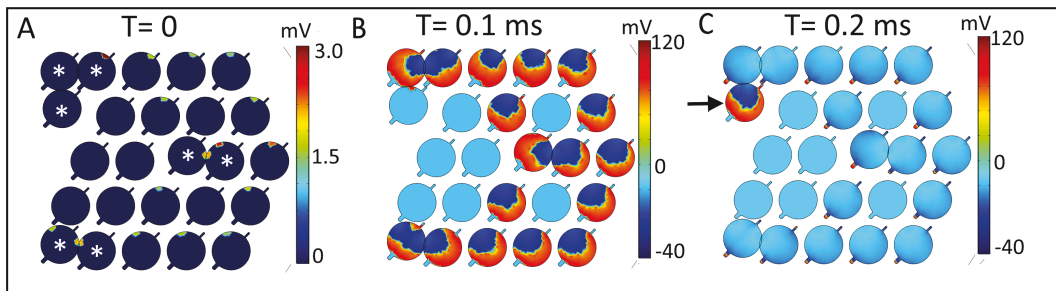


FIGURE 3.14: (A) Signal initiation sites on the SGNs where a star marks the clustered SGNs. (B) Signal propagation through the activated SGNs. (C) The arrow shows the activation of an SGN in the cluster due to ephaptic coupling.

TABLE 3.3: FHN parameters

Parameter	Value	Description
$a$	0.0014	Excitation threshold
$b$	0.002	System parameter
$c$	2.54 $b$	System parameter
$d$	0	System parameter
$e$	1.8	Excitability

A hypothetical case of cell clustering is shown in Figure 3.14 (A), where two or more SGNs form a cluster. Figure 3.14 (B) and (C) shows the signal initiation

### 3.3. Simulation

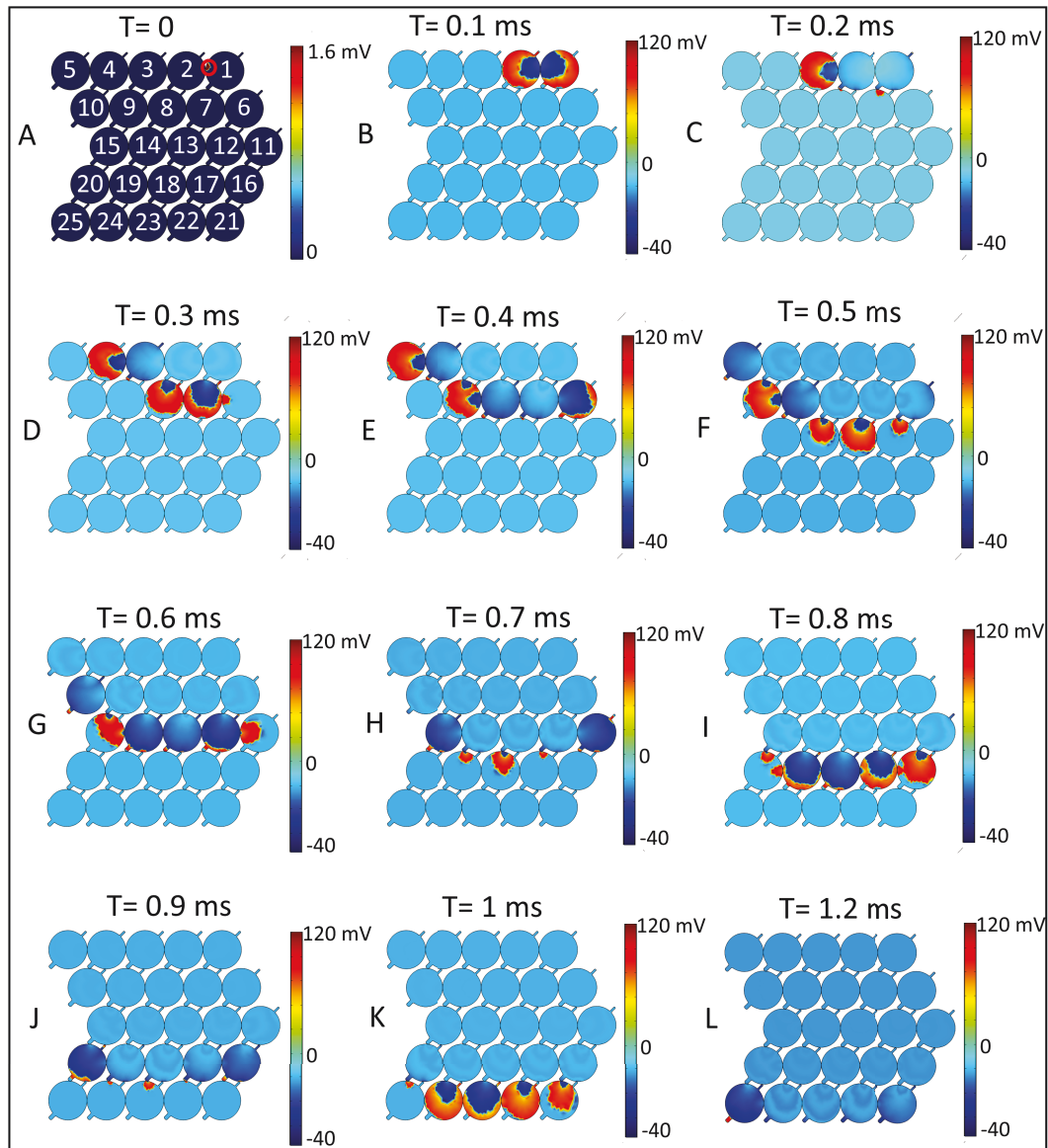


FIGURE 3.15: (A) Signal initiation site on the first SGN (red circle), (B)–(L) signal propagation in the adjacent SGNs due to ephaptic coupling.

and propagation in the computational domain. Due to the threshold voltage constraint, only 18 out of 25 SGNs are activated. Since the induced  $V_m$  is below the desired threshold value, remaining seven SGNs are not activated. This effect is comparable to the so-called cell packing effect discussed in [130]. Although far from the electrodes, a nerve signal was initiated at the contact point of SGN membranes in the clusters. Since the transmembrane potential is proportional to the cell volume, the induced  $V_m$  would reach its maximal value at the contact point of SGNs due to the cumulative volume of the cluster. From above results, it can be speculated that a cell cluster acts like a giant cell susceptible to easy activation. On the one hand, CI stimulation may readily activate these cell clusters which in turn would hinder the objective of selective stimulation. On the other hand, due to the presence of unmyelinated SGNs

in the human, the resultant giant cell could alter the temporal component of the auditory signal in a healthy ear. Since the cell clustering is prevalent in the elderly people [131], it can be assumed that the alteration in the temporal component of the signal could affect the hearing sensation. Perhaps, the incidence of age-related deafness could be attributed to the gradual formation of the cell clusters.

The worst-case scenario of cell clustering is shown in Figure 3.15 (A) where all SGNs from a single cluster. Figure 3.15 (B)–(L) shows the cross-excitation of SGNs in which only one SGN was allowed to excite initially. Since each SGN has at least one contact point with the adjacent SGN in a cluster, all SGNs consequently fired the action potentials due to the ephaptic coupling. In the present simulation case, adjacent SGNs fired action potentials in the interval of 1 ms after the excitation of the first SGN. This temporal delay in the generation of the signal may produce a persistence ringing sound or tinnitus effect in the ear [132]. In other words, an electric stimulation meant to excite a particular SGN could excite the remaining SGNs in a cluster. This unintended excitation of the SGNs could produce a noisy signal. Physiologically, this could be one of the factors for the lack of fine pitch perception in the CI users. However, thorough experimental validation is required to support this argument.

### 3.3.4 3D results

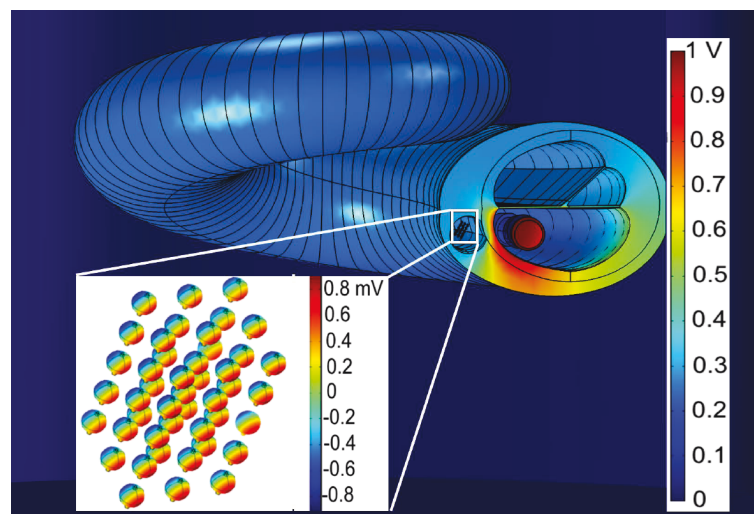


FIGURE 3.16: Electric potential distribution in the 3D computational domain and (inset) corresponding transmembrane potentials on the SGNs.

The bony labyrinth of the cochlea contains three fluid chambers separated by two membranes of low electric conductivity. Unlike the 2D model, the 3D model of the cochlea facilitates these additional computational domains in the simulation. Hence, the 3D modeling is helpful to visualize the realistic electric field distribution in the RC. Figure 3.16 shows the potential distribution in the 3D computational domain. The inset of Figure 3.16 shows the transmembrane potential of symmetrically arranged SGNs in the RC. In the case of electric



stimulation of SGNs in a homogeneous medium, additional computational domains in the 3D model provide additional pathways to the impressed current to reach the counter electrode. As a consequence, the 3D model gives quantitatively different simulation results compared to those of the 2D model. However, the effects of SGN orientation and cell clustering on the signal initiation suppose to remain qualitatively similar in both 2D and 3D models. Simulation results of the 3D model concerning the various aspects mentioned in previous sections are not presented here to avoid the redundancy and repetition of qualitatively similar 2D model results. Rather, the 3D cochlear model has been utilized comprehensively in the next chapter.

## 3.4 Summary

The extracellular electric stimulation of neural tissues has been both beneficial and challenging in clinical applications. Through experimental studies, it is not always possible to investigate the full spectrum of electric field effects on the tissues. Under some assumptions and simplifications, a mathematical model can provide some useful insights about a bioelectric phenomenon that is otherwise difficult to understand. For example, neural tissue activation due to extracellular stimulation in a homogeneous medium can be estimated by the AF. If the morphology of the neural tissue and the characteristic of the extracellular medium have to be considered, the sub-threshold transmembrane potential approximation could also be equally useful to estimate the neural tissue activation. Electric stimulation of the auditory nerve by cochlear implants is one such clinical application which needs to be understood down to the activation of the SGNs to efficiently treat the profound deafness. Experimental studies and modeling studies arguably suggest that the location of the signal initiation on the SGN is either on the AIS or on the neuronal cell body. In this chapter, through the sub-threshold transmembrane potential approximation, it has been shown that the orientation and the clustering of SGNs could affect the signal initiation and propagation in the auditory nerve.



## Chapter 4

# Modeling the Porosity of the Modiolus

In this chapter, two simple methods to model the porosity of the modiolus bone in the cochlea are introduced. Since the porosity of the modiolus bone was neglected in the existing *in silico* models while modeling the CI stimulation of the auditory nerve, the present study investigates whether the effect of modiolus porosity on the electric stimulation of the SGNs is negligible.

### 4.1 The Modiolus

The modiolus of the cochlea is a 100  $\mu\text{m}$  thin multi-layered porous bony wall that separates the perilymphatic duct from the RC [133, 134, 26]. Nevertheless, this interface is permeable to perilymph into the RC via modiolus pores. The transportation of perilymph is essential to keep the adequacy of ion concentration of the extracellular medium in the RC [134]. Notably, pores on the modiolus have no regular shape and no specific distribution pattern as shown in Figure 4.1. Morphological studies suggest that the porous modiolus is a prospective gateway for drug delivery for the artificial regrowth of the neural structures in the RC [134]. Further, Malherbe and colleagues [135] suggest that the electric conductivity of skull and other bony structures in and around the cochlea would profoundly affect the electric field distribution in the RC. Besides, the transportation process of the perilymph through the modiolus could also induce so-called streaming potentials similar to that in the femoral trabecular bone in humans [136]. Further, during the electrode insertion through the round window into the Scala tymphani, the tip of the electrode could disrupt the sensitive bony structure of the modiolus. This in turn not only induces the trauma but also could crack the porous modiolus wall. However, in the context of mathematical modeling, existing *in silico* models assumed the modiolus as a non-porous bone having isotropic electric conductivity. In the case of deafness induced by depletion of peripheral processes of the auditory nerve, the modiolus pores would be filled by perilymph and amputated neural tissues. In this pathology, the electric conductivity of multi-layered modiolus would not be equal to the conductivity of the bone alone. Instead, the effective conductivity of the porous modiolus would be

the combination of the electric conductivity of the perilymph and the bony material.

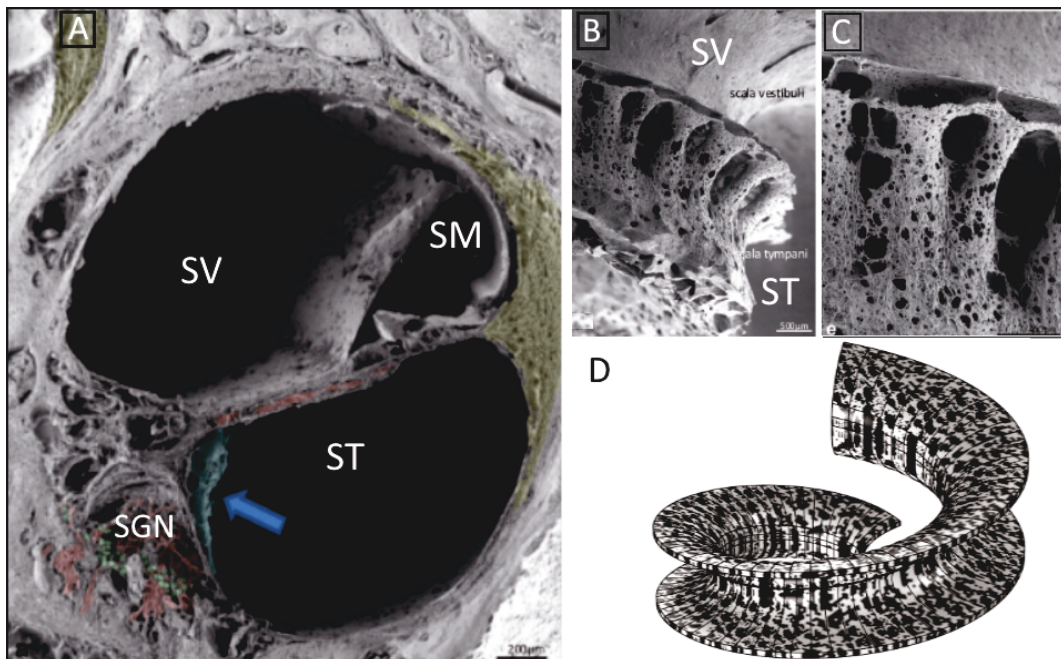


FIGURE 4.1: (A) "Possible trauma sites for cochlear implantation and position of neural elements in the human cochlea lower basal turn. Between scala tympani (ST) and the SGNs (colored green), a thin mesothelial sheet (arrow) spans between bony columns that guide nerve fibers (colored red) to the osseous spiral lamina, SV–Scala vestibuli, SM–Scala media". (B) and (C) The porous structure of the modiolus. (D) Qualitative representation of the porous modiolus conductivity mapped through image-based modeling. (Image courtesy: (A)–(C) are taken from [26] and adapted for the present study with the permission of Elsevier).

## 4.2 Modeling the modiolus porosity

Three dimensional reconstruction of the cochlea from micro computer tomography ( $\mu$ CT) images would not sufficiently capture the porous structure of the modiolus. Since the micro pores of the modiolus have no regular shape, size, and distribution, an empirical formula suggested in [137] to calculate the resultant electric conductivity of porous sheet is not applicable for modeling the modiolus porosity. Also, no generalized data are available for the volume fraction of the bone and pores of the modiolus.

Unless mentioned separately, all simulations in the present study are performed with the same boundary conditions, dielectric properties, and the governing equations those were implemented for the 3D cochlear model described in the previous chapter.

### 4.2.1 Image-based modeling

In the present study the gray scale pixel data of a SEM image shown in Figure 4.1 (C) was imported into COMSOL in which the pixel data are normalized between 0 and 1, and stored in  $Im(x, y)$  function. Through the linear extrusion of the pixel data obtained from the SEM image of the modiolus, the isotropic conductivity of the bone and the pores was mapped on the modiolus domain according to the conditional equation (4.1). Figure 4.1 (D) qualitatively represents the porosity of the modiolus of a portion of the cochlea. Here, all modiolus pores are assumed to be filled with perilymph.

$$\sigma_{modiolus} = \begin{cases} 0.0334 \text{ (S/m)}, & Im(x, y) > 0.5 \text{ (bone conductivity)} \\ 1.2 \text{ (S/m)}, & Im(x, y) \leq 0.5 \text{ (pore conductivity)}. \end{cases} \quad (4.1)$$

By this method, modeling the actual geometry of the modiolus pores which would demand an unprecedented number of mesh elements and computational cost during the simulation could be avoided without losing the generality of the problem. After mapping the conductivity of bony structure and the pores (perilymph), the effective conductivity of the modiolus was estimated by calculating the volume fraction of the bone and pores in the first stage of the numerical simulation. In the second stage, three simulation cases were considered to investigate how the non-porous modiolus with only bone conductivity ( $\sigma_{bone}$ ), the porous modiolus with mapped conductivity ( $\sigma_{map}$ ), and the non-porous modiolus with effective conductivity ( $\sigma_{eff}$ ) affect the transmembrane potential of the SGNs.

Another interesting question would be how the degree of porosity of the modiolus affects the transmembrane potential of the SGNs. The physiological relevance of this question is apparent from the fact that the porosity of the modiolus could change with the age and the pathology of the cochlea. For instance, if younger child were to carry a cochlear implant all his life, the functionality of the CI would vary with several age related-factors [138]. However, little is known by experimental studies and perhaps would be only possible through *in silico* investigations to find out how the variance of the degree of porosity of the modiolus would affect the stimulation profile of the SGNs. To do so, nine samples of incremental bone porosity were derived from Figure 4.1 (D) and equation (4.1). Figure 4.2 shows nine modiolus samples of the indicated porosity and effective conductivity.

### 4.2.2 Results

Figure 4.3 shows the induced transmembrane potential of five SGNs for the indicated electric conductivity of the modiolus. When the electric conductivity of the modiolus is assumed to be equal to that of a non-porous bone ( $\sigma_{bone} = 0.0334 \text{ S/m}$ ), the induced transmembrane potential of SGNs is below 1.2 mV. All state-of-the-art *in silico* models have often assumed this case [139]. However, in the second case of mapped electric conductivity of the modiolus

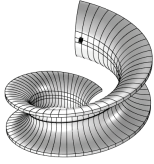
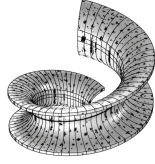
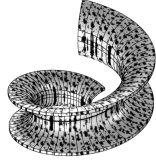
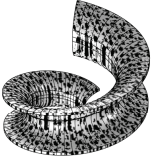

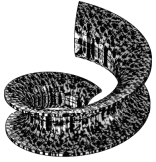



<p>S1</p>  <p>Porosity: 0% Eff.Conductivity: 0.0334 S/m</p>	<p>S2</p>  <p>Porosity: 8.5% Eff.Conductivity: 0.1325 S/m</p>	<p>S3</p>  <p>Porosity: 23.5% Eff.Conductivity: 0.3092 S/m</p>
<p>S4</p>  <p>Porosity: 33.1% Eff.Conductivity: 0.4202 S/m</p>	<p>S5</p>  <p>Porosity: 43.5% Eff.Conductivity: 0.5410 S/m</p>	<p>S6</p>  <p>Porosity: 56.3% Eff.Conductivity: 0.6911 S/m</p>
<p>S7</p>  <p>Porosity: 70.6% Eff.Conductivity: 0.8574 S/m</p>	<p>S8</p>  <p>Porosity: 84% Eff.Conductivity: 1.0136 S/m</p>	<p>S9</p>  <p>Porosity: 92% Eff.Conductivity: 1.1149 S/m</p>

FIGURE 4.2: (S1–S9) Samples of the modiolus porosity derived from the image base modeling. It is observable from these samples that the effective conductivity of the modiolus is proportional to the modiolus porosity

with a given porosity, the induced transmembrane potential of SGNs is between 2.8 mV to 3.8 mV which is 300% more than that in the first case. This result shows how profoundly the modiolus porosity affects the stimulation profile of the SGNs. For example, any *in silico* model with non-porous modiolus that predicts the excitation of the SGNs based on the potential distribution in the RC would certainly underestimate the magnitude of the electric potential in the RC. This implies, the number of stimulated SGNs would be much higher than those predicted in the existing *in silico* cochlear models.

Another usual method to implement the effect of porosity of a bone in a computational model without modeling the actual geometry of pores would be considering the effective conductivity of the porous bone. Several analytical methods are available to calculate the effective conductivity of a porous material [140, 141, 142, 143, 144]. However, in the present case, no data are available about the volume fraction or the pore size to estimate the effective conductivity of the modiolus. Nevertheless, after the liner extrusion of the pixel intensity data on the modiolus domain, the modiolus porosity was estimated by calculating the ratio of the volume occupied by the pixel intensity that represents the pores ( $Im(x, y) < 0.5$ ) to the total volume of the modiolus domain. The estimated porosity of the modiolus in the present study by this method is 46.5%. After assigning the electric conductivity of the modiolus domain using equation (4.1), the effective conductivity of the modiolus estimated

## 4.2. Modeling the modiolus porosity

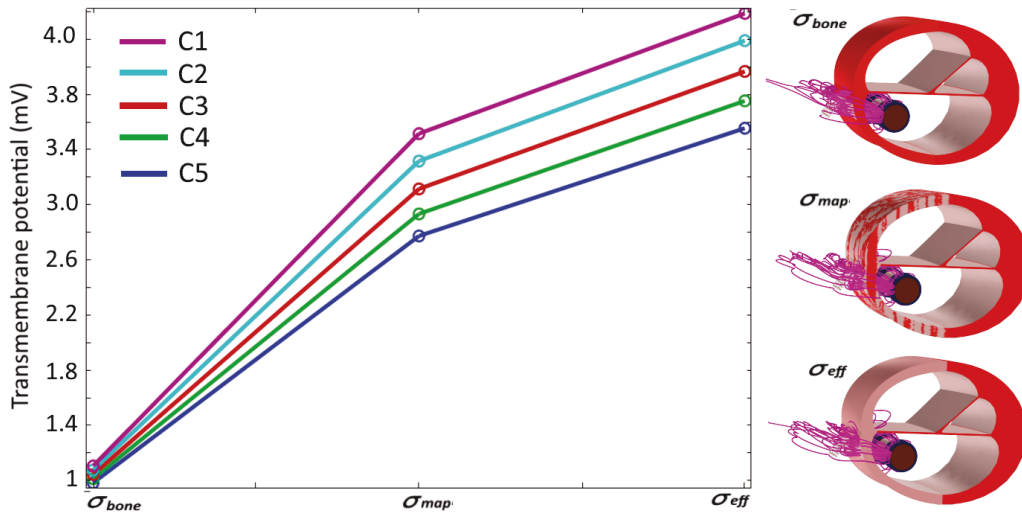


FIGURE 4.3: Induced transmembrane potential ( $V_m$ ) of five SGNs as a function of electric conductivity of the modiolus.  $\sigma_{bone}$ : Conductivity of non-porous bone,  $\sigma_{map}$ : Conductivity of porous bone mapped with image based method,  $\sigma_{eff}$ : Effective conductivity of non-porous bone obtained by volume fraction of the pores. On the right: The stream lines of current density across the modiolus for three indicated cases.

by the numerical simulation was approximately 0.576 S/m.

To check the correctness of the above method, the effective conductivity values estimated through COMSOL simulations for the given porosity of the modiolus were compared with the effective conductivity values calculated by the analytical expression given in equation (4.3). Here,  $P_1$  and  $P_2$  are the volume fractions of the sample where  $P_1 + P_2 = 1$ , and  $\sigma_1$  and  $\sigma_2$  are the respective electric conductivities.  $\sigma_{eff}$  is the effective conductivity of the sample between the lower ( $\sigma_L$ ) and upper ( $\sigma_U$ ) Wiener bounds. Here upper and lower Wiener bounds are the arithmetic mean and harmonic mean of the constituent conductivities weighted by the respective volume fractions (analogous to the network of resistors in parallel and series respectively) [145, 146].

$$\sigma_L \leq \sigma_{eff} \leq \sigma_U \quad (4.2)$$

Where

$$\begin{aligned} \sigma_U &= P_1\sigma_1 + P_2\sigma_2 \\ \sigma_L &= \left[ \frac{P_1}{\sigma_1} + \frac{P_2}{\sigma_2} \right]^{-1} \end{aligned} \quad (4.3)$$

From Figure 4.4, the effective conductivity values calculated by COMSOL have fairly satisfied the condition given in equation (4.2).

As the third case, this effective conductivity value was assigned to the modiolus. The induced transmembrane potential of the SGNs, in this case, is between 3.5 mV to 4.5 mV which is around 20% more than that in the second case. This implies, the assumption of the effective conductivity would

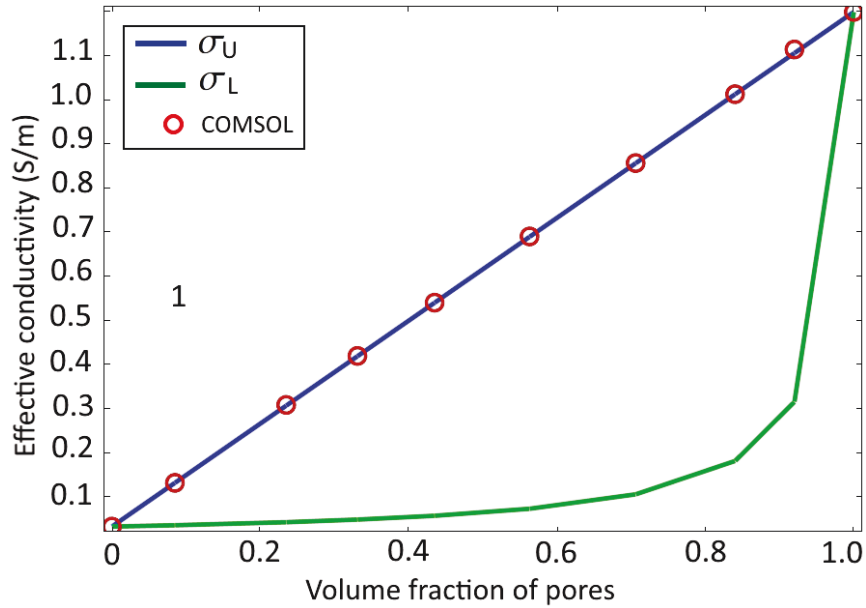


FIGURE 4.4: Effective conductivity of modiolus as a function of the volume fraction of pores obtained. Hard lines show the upper and lower Wiener bounds calculated by equation (4.3) and red circles show the effective conductivity values calculated by COMSOL.

overestimate the magnitude of the electric potential in the RC. Further, the simulation results suggest that up to 50% modiolus porosity, the effective conductivity of the modiolus would be as high as 0.6 S/m. This recommended conductivity value for the modiolus is much higher than the conductivity of the bone that had been implemented in the existing *in silico* models. Above results also suggest that the effective conductivity approach for the modiolus yields different results compared to those of the mapped electric conductivity approach in the presence of modiolus porosity.

Figure 4.5 (A) shows the induced transmembrane potential of five SGNs as a function of the modiolus porosity of nine samples. A steep growth in the induced transmembrane potential of the SGNs can be seen as the modiolus porosity increases from 8.5% to 56.3%. The variation in the porosity (S2–S6) could occur due to aging (data not available). If this were physiologically true, then the simulation results suggest that a very young CI recipients would experience undesirable inconsistency in the performance of the implant with the aging which in the worst case they may lead to a revision surgery. Surprisingly this scenario has been observed in many young CI recipients [147, 148]. However, the modiolus porosity could not be the only factor for the outcome of these studies. Further, a very high porosity indicated by S7–S9 could occur due to various cochlear diseases such as Paget’s disease in which bone mineral density alters with the progression of the disease [149]. However, if the porosity of the modiolus reaches above 70%, the modiolus would behave like a good conductor. In this case, most of the impressed current would spread in the RC and would reach the return electrode. However, this would



## 4.2. Modeling the modiolus porosity

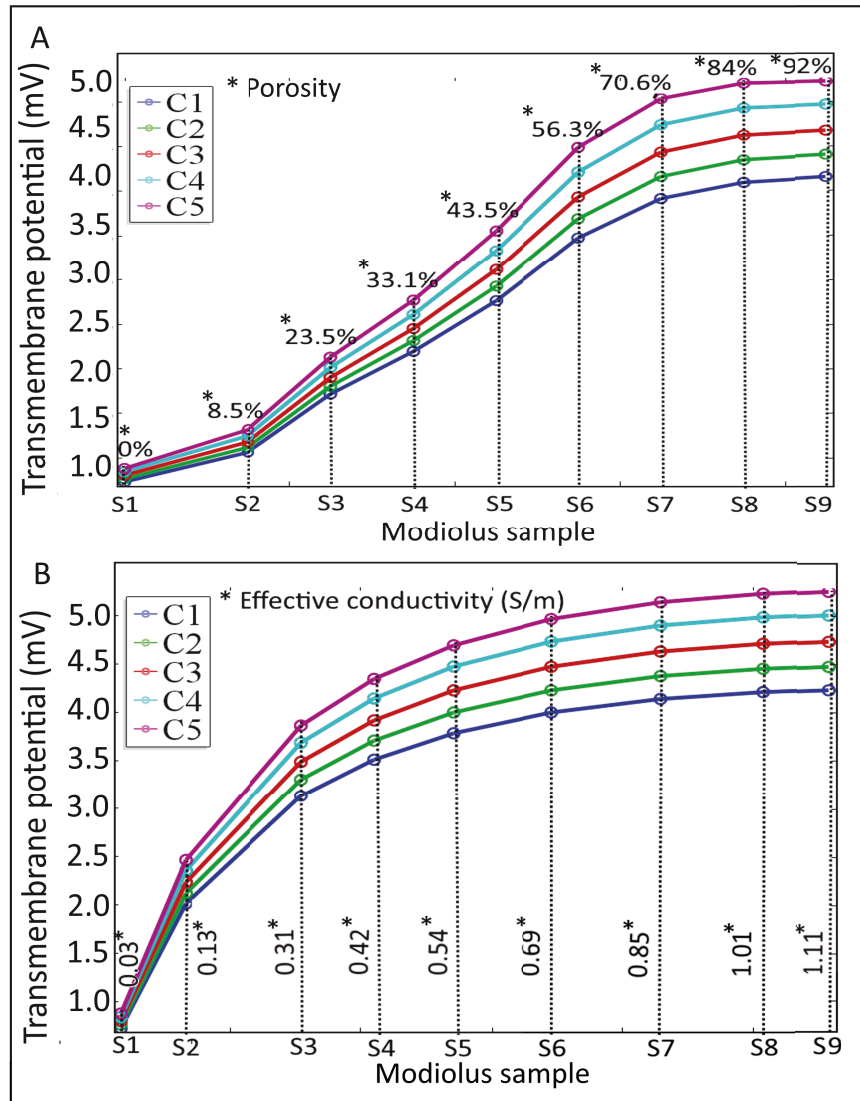


FIGURE 4.5: (A) Induced transmembrane potential ( $V_m$ ) as a function of mapped porosity. (B)  $V_m$  as a function of effective conductivity obtained by respective porosity. S1 through S9 indicate the modiolus sample numbers. The response of SGNs is not identical in both cases.

be a hypothetical case; where the extreme modiolus porosities (below 20% and above 60%) would only represent the worst case scenarios.

On the other hand, it is observable from Figure 4.5 (B) that the implementation of the effective conductivity of assumed realistic modiolus samples (S3–S6) in the model has predicted only 0.5 mV increment in the induced transmembrane potential of the SGNs. Further, for S7, S8, and S9, both cases predicted almost the same increment in the induced transmembrane potential of SGNs. For S1 and S2 where the modiolus porosity is low, the effective conductivity approach has yielded 200% increment in the induced transmembrane potential of SGNs. Whereas, for the same samples, mapped conductivity in the presence of the

modiolus porosity produced 50% increment.

To the best knowledge of the author, the present study is first of its kind *in silico* study that has investigated the effect of modiolus porosity on the induced transmembrane potential of SGNs. These results throw light on crucial pitfalls in cochlear modeling that intended to simulate the electric field distribution in the cochlea. For instance, if one intended to simulate the modiolus porosity using the parametric sweep of the effective conductivity values within the assumed realistic range (S4–S6), the results would not be significantly different from one another. Thus, from these results, one can deduce that the effect of modiolus porosity on the stimulation profile of the SGNs is negligible. Hence, neglecting the modiolus porosity in the cochlear modeling would appear as a reasonable modeling assumption. However, for the transmembrane threshold potential of 4 mV, the effective conductivity method predicts the stimulation of all SGNs in the RC for above-assumed modiolus conductivity values. This overestimation of the excitation of the SGNs contradicts the experimental studies which has been a matter of concern in *in silico* modeling of the electric stimulation of the auditory nerve [139].

However, by implementing the actual porosity of the modiolus through the conductivity mapping method, a steep variation in the simulation results can be seen. This implies, the 'latent' influence of the modiolus porosity can only be unraveled through the implementation of the realistic porosity in the model. This suggests that the small increment (even 10%) in the modiolus porosity caused by any internal or external factors such as the injury caused by the CI electrode insertion could disproportionately affect the stimulation profile of the SGNs. Hence, the electric stimulation of auditory nerve should be patient-specific, especially, customized according to the age of the CI recipient.

In the context of the present study, it is also important to investigate why the effective conductivity method and the mapped conductivity method yields different simulation results. One possible reason would be the local porosity of the modiolus. In the effective conductivity method, the implementation of a single isotropic and homogeneous conductivity value for the modiolus would not capture the local porosity. In the next section, the effect of local porosity on the induced transmembrane potential of the SGNs is investigated through a set of modiolus samples with similar volume fraction but different local porosities.

### 4.2.3 Equation-based modeling

A mathematical approach with a set of reaction-diffusion equations (R-D) to model the formation of skin strips on various animals was proposed by Alan Turing [150]. Turing's R-D equations elegantly form desired patterns with the aid of a few system parameters. Also, for each progressive time step these R-D equations form different patterns initiated by the previous pattern. Later, various analytical studies explored number of R-D equations to mimic the formation of symmetric as well as asymmetric patterns occurring in the nature [151, 152, 153]. In the light of these studies, one can assert that with

## 4.2. Modeling the modiolus porosity

---

the aid of relevant R-D equations the asymmetric microstructures such as the modiolus porosity can be modeled.

Dwight Barkley and colleagues [154, 155] proposed a set of robust R-D equations to simulate the wave pattern in three-dimensional excitable media as shown in equation (4.4).

$$\begin{aligned}\frac{\partial u}{\partial t} &= \frac{1}{c}(u(1-u)(u - \frac{(v+b)}{a})h(v)) + \Delta u, \\ \frac{\partial v}{\partial t} &= f(u, v) + D\Delta v, \\ h(v) &= 1,\end{aligned}\tag{4.4}$$

where  $f(u, v)$  defines the local reaction kinetics with the state variables  $u$  and  $v$ , and system parameters  $a$ ,  $b$ , and  $c$ .  $\Delta$  and  $D$  are the Laplace operator and the diffusion coefficient respectively. Originally, to represent the spiral wave fronts,  $f(u, v)$  is defined in [155] as :

$$\begin{aligned}f(u, v) &= g(u) - v \\ g(u) &= u\end{aligned}\tag{4.5}$$

However,  $g(u)$  could also be defined differently to qualitatively represent other wave forms such as spiral breakup and spiral turbulent waves [156]. In [157],  $g(u)$  was defined with lower and upper limiting values to represent the catalyst surface reactions as shown in equation (4.6).

$$g(u) = \begin{cases} 0, & u < \frac{1}{3} \\ 1 - 6.75u(u - 1)^2, & \frac{1}{3} \leq u \leq 1 \\ 1, & u > 1. \end{cases}\tag{4.6}$$

In the present study, a set of R-D equations obtained by modifying equations (4.4) and (4.6) has been proposed to model the pattern of non-deterministic distribution of the modiolus pores as shown in equation (4.7):

$$\begin{aligned}\frac{\partial u}{\partial t} &= \frac{1}{c}u(1-u)(u - \frac{(v+b)}{a}) + D\Delta u, \\ \frac{\partial v}{\partial t} &= g(u) - v - \alpha u,\end{aligned}\tag{4.7}$$

where

$$g(u) = \begin{cases} 0, & u < \frac{1}{3} \\ 1 - 9u(1-u)^2, & \frac{1}{3} \leq u \leq 1 \\ 1, & u > 1. \end{cases}$$

Here  $\alpha$  controls the porosity of a sample. One advantage of equation-based modeling over the image-based modeling is the flexibility of creating heterogeneous distributions of pores in all three spatial directions by controlling the diffusion coefficient ( $D$ ). In addition, for a given volume fraction, it is

also possible to model an asymmetric distribution of the pores which could result in local variability in the pore density. In other words, though several modiolus samples have the same global porosity, the variation in the local pore density could result in different local constituent porosities. Hence, the implementation of effective conductivity derived from the volume fraction of the modiolus would not represent the realistic scenario.

To study the effect of 'local porosity' of the modiolus on the transmembrane potential of SGNs, six modiolus samples of different local porosity patterns with similar volume fraction have been modeled as shown in Figure 4.6. These patterns are formed by equation (4.7) with  $D = 1$ ,  $a = 0.64$ ,  $b = 0.02$ ,  $c = 0.08$ , and  $\alpha = 0.2$ .

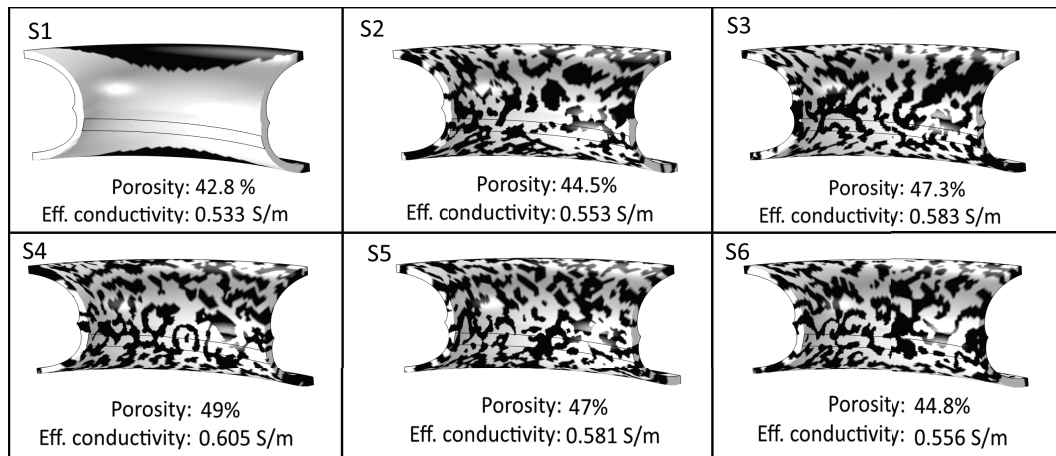


FIGURE 4.6: (S1–S6) Equation based modiolus porosity samples with similar global porosity and effective conductivity but different local patterns of pores.

Figure 4.7 shows on top the effect of local porosity on the induced transmembrane potential of the SGNs. Here, S2 and S6 have similar global porosity but different pore distribution. Hence, a definite difference in the response of the SGNs is apparent in two samples. Likewise, S3 and S5 also have the same porosity; however, the difference in the pore distribution resulted in different induced transmembrane potentials. It is also noticeable from S1 that though the modiolus porosity is around 43%, the induced transmembrane potential on all SGNs is around 1 mV (compare with S5 in Figure 4.5 (A)). On the other hand, though the modiolus porosity in S4 is 49% which is highest among all samples, the induced transmembrane potential of SGNs is not proportional to the porosity.

This investigation is also critical to explore some new parameters for patient-specific cochlear modeling. The variance in the anatomy of the cochlea and electrode position have been the main parameters for the patient-specific cochlear modeling [158]. Besides, global and local variations in the porosity of the modiolus would be an essential modeling parameter to represent a realistic cochlea. Since the porous modiolus could have an effective conductivity which is fifteen times more than the non-porous bone, the endosteal cochlear

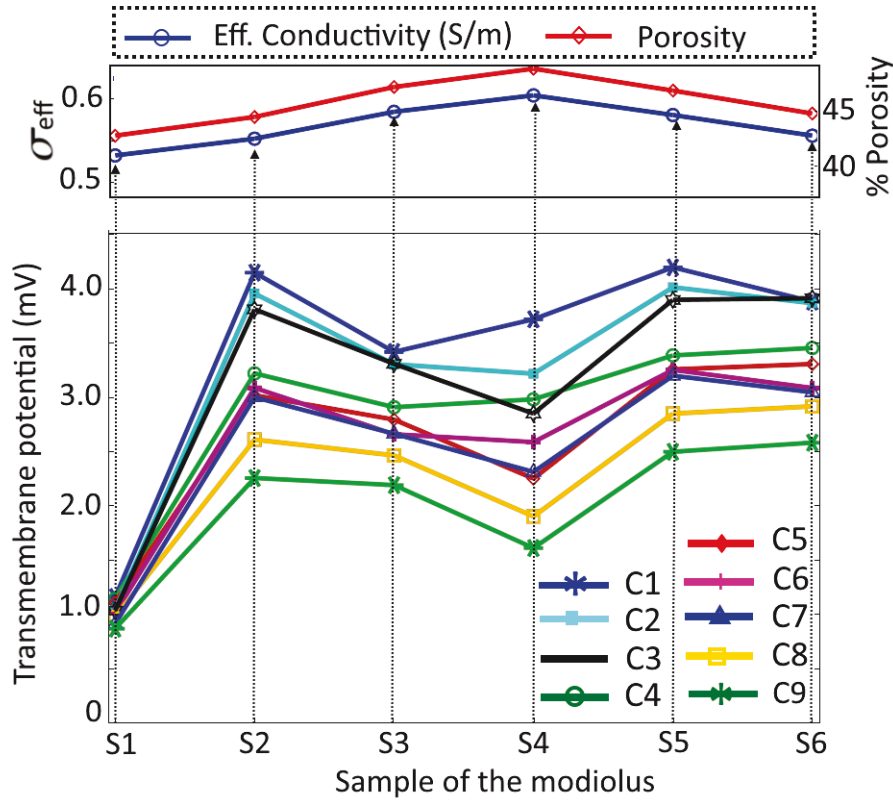


FIGURE 4.7: Top: Effective conductivity and corresponding porosity of each sample. Bottom: Induced transmembrane potential ( $V_m$ ) of indicated SGNs for six samples of the modiolus (S1–S6) with similar porosity but different pore distribution.

implants would be a feasible option for retaining the residual hearing [159, 160].

### 4.3 Summary

Modiolus in the cochlea is a porous interface that separates the scala tympani and the RC. During the electric stimulation of the auditory nerve by cochlear implants, the applied current distribution in the cochlea largely depends on the physiological and dielectric properties of surrounding interfaces. All state-of-the-art *in silico* models have assumed the modiolus a non-porous bone with very low electric conductivity. As a result, the activation threshold of SGNs has been underestimated. However, with the implementation of modiolus porosity using proposed innovative methods, the present *in silico* model results suggest that the induced  $V_m$  could be 300% higher than that in the case of a non-porous modiolus bone. The estimated effective conductivity of the porous modiolus in terms of volume fraction of the pores could be fifteen times more than the previously assumed conductivity of a non-porous bone. In addition, even with similar global porosity the heterogeneous distribution of modiolus pores could result in an asymmetric excitation of the SGNs. These

results suggest that the global and local modiolus porosity could serve as additional parameters for modeling the patient specific cochlea.

## Chapter 5

# Modeling Tissue Heterogeneity in the Rosenthal's Canal

In this chapter, an image based method to implement the tissue heterogeneity in the RC in a 2D finite element model is introduced. Subsequently, the effect of tissue heterogeneity on the induced transmembrane potential of type-1 SGNs and the clinical relevance of the simulation results are discussed. The content of this chapter closely resembles with our recent publication [161].

### 5.1 The Rosenthal's canal

A quick recapitulation about the composition of the RC excerpted from [162, 26] and [163, 164] is given below.

RC is a bony helical canal that extends up to one and half turn of the cochlea. It contains neuronal cell bodies of all efferent and afferent innervations of the auditory nerve. The peripheral processes of all SGNs protrude through the modiolus and connect to their respective hair cells. The central processes of all SGNs innervate towards the auditory cortex. Morphological studies of the human temporal bone suggest that 96% of SGNs are of the type-1 category which plays a crucial role in auditory transduction through their efferent innervations. Remaining 4% of SGNs fall under the type-2 category which connects the outer hair cells through the afferent innervations. Immunohistochemical studies suggest that type-1 spiral ganglion neuronal bodies in the human cochlea are unmyelinated, albeit loosely enwrapped by the satellite glial cells (SGCs). Furthermore, AIS of type-1 SGNs are covered with non-myelinated Schwann cells (NMSC), whereas the central processes of type-1 SGNs are myelinated. Besides, type-1 SGNs form cell clusters which share a common membrane at the contacting boundaries. Apparently, various tissues and cells asymmetrically envelop type-1 SGNs in the RC. As a result, each SGN encounters a different degree of tissue heterogeneity around it. Although all type-1 SGNs in a given accommodation have similar morphology per se, tissue heterogeneity could impel each SGN to respond uniquely to the applied electric field.

Satellite glial cells, on the other hand, form a non-uniform tissue layer that acts as a proxy membrane around each type-1 SGN. This SGC layer protects the

SGN cell body and facilitates the ion exchange via gap junctions. Experimental studies suggest that even a slight depletion of the SGC layer causes inflammation and pain that may lead to cell death [165]. In this context, it is necessary to investigate how the presence of the SGC layer influences the electric field distribution around each SGN and vice versa. Further, arbitrary spatial distribution of the myelinated central axons, the type-2 SGNs, and a few blood vessels could also influence the electric field distribution in the RC. Above stated tissue and cells stem from the basic crest cells. However, the dielectric properties of the tissues may vary considerably with the age and maturation of the crest cell. This implies that each tissue in the RC could contribute its characteristic dielectric properties to the system. Hence, the assumption of a homogeneous extracellular medium in the RC is not appropriate to model the electric field distribution in the RC.

## 5.2 Problem definition

The effects of tissue heterogeneity on the electric field distribution in several bioelectric phenomena have been reported in the literature [166, 167, 168, 169, 170]. In spite of evident tissue heterogeneity in the RC, existing *in silico* models have not considered it in the modeling. Conceivably, modeling the heterogeneity in the RC is challenging due to the microscopic topology of the tissues. Besides, most of the tissues had neither defined shape nor prescribed spatial distribution in the RC. Hence, the classical image segmentation methods based on the pixel data obtained by magnetic resonance tomography (MRT) or  $\mu$ CT may not be efficient to reconstruct the tissue geometry. Also, the author could not come across the resource of  $\mu$ CT image stock of the RC at the time of the present study. Moreover, to the best knowledge of the author, the published data about the tissues in the RC are obtained by immunohistochemistry or scanning confocal electron microscopy (SEM) or transmission electron microscopy (TEM) which need specialized methods for the direct implementation of the captured data in the simulations [171]. Further, the SEM and the TEM provide incredibly detailed data of a minuscule sample which is too tiny to model as a computational domain for the FEM.

Prospectively, immunohistochemistry of the RC provides the data of important tissues in the context of the present study. An immunohistochemical image of the RC contains various tissues delineated by false-color coding; the color code of different tissues not only unveils the physiology and morphology of the respective tissues but also visualizes the heterogeneous distribution of the tissues. For example, Figure 5.1 shows various tissues along with their respective color coding in the RC of the human cochlea. With the visual inspection, it can be discerned that type-1 SGNs in the RC are surrounded by randomly distributed myelinated central axons and type-2 SGNs and other tissues. Further, the SGNs have unmyelinated axonal initial segments and are loosely wrapped by SGCs. Once the tissues are classified, and the dielectric properties of concerned tissue are obtained, the resultant data could be manipulated to model the tissue heterogeneity in the RC. The spatial distribution



### 5.3. Method

of the tissues in the RC can be extracted according to the pixel intensities of a pertinent image.

However, all tissues in the present study are considered as passive and no electrophysiological activity is expected to take place on any tissue other than the SGNs membrane. Therefore, the continuity boundary condition is applicable on the boundaries of the heterogeneous tissues. This implies, if the complex geometry of the tissues were to be excluded in the model, the distribution of spatial coordinates of each tissue should be well known. Accordingly, instead of modeling the actual geometry of the tissues, respective spatial distribution of dielectric properties could be substituted in the computational domain without losing the generality of the problem.

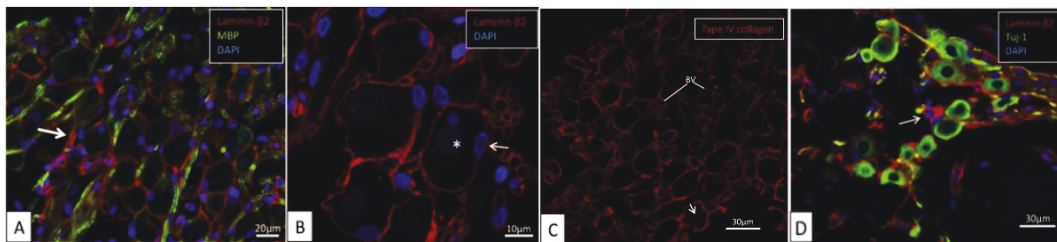


FIGURE 5.1: "Immunohistochemistry of the human spiral ganglion showing the immunoreactivity of laminin- $\beta$ 2 and myelin basic protein (MBP) through confocal microscopy. (A) Most type I SGNs are MBP-negative. Some non-myelinated perisomal segments show rich expression of laminin (arrow). DAPI, cell nuclei. (B) Laminin- $\beta$ 2 immunoreactivity of basement membrane lining the extracellular surface of the SGCs of the SGN bodies, nerve fibers and blood vessels (BV) (normal audiogram). Type I SGN cell nuclei are round and darkly stained (\*) while SGC nuclei are crescent-like (arrows) and more lucent. Their cytoplasm shows no laminin expression. DAPI, nuclear staining. BV, blood vessels. (C) Collagen IV immunoreactivity of basement membrane lining the extracellular surface of the SGCs of the SGN bodies, nerve fibers and blood vessels (BV). (D) A rendered confocal microscopy stack showing laminin- $\beta$ 2 immunofluorescence of the human spiral ganglion. A laminin expressing NMSC is seen (thin arrow) as well as a laminin-negative SGC (thick arrow)". *Reproduced and adapted from [93] with permission from Elsevier.*

## 5.3 Method

To implement the tissue heterogeneity in a 2D computational domain, an immunohistochemistry image of the RC shown in Figure 5.2 (A) was considered. The segmentation technique suggested in [172] was utilized to segment the image into two separate constituents *viz.* contours of the SGNs (Figure 5.2 (B)) and contours of all other tissues (Figure 5.2 (C)). The contours of SGNs are not only useful to restore the realistic geometry of the SGNs but also essential to calculate the transmembrane potential of the SGNs. Besides, the dimensions of SGNs cell body (diameter  $\approx 30 \mu\text{m}$ ) located at the basal end of the cochlea are large enough to model the cell geometry in the computational domain. However, modeling the geometry of various thin tissues such as

SGCs (thickness  $\approx 0.5 \mu\text{m}$  to  $1 \mu\text{m}$ ) in the RC is implausible. Since the geometry of tissues which contain multiple layers and sharp edges could result in discretization errors as well as a substantial number of mesh elements that would demand significant computational cost even for a 2D model. Figure 5.3 shows the final geometry of 2D computational domain.

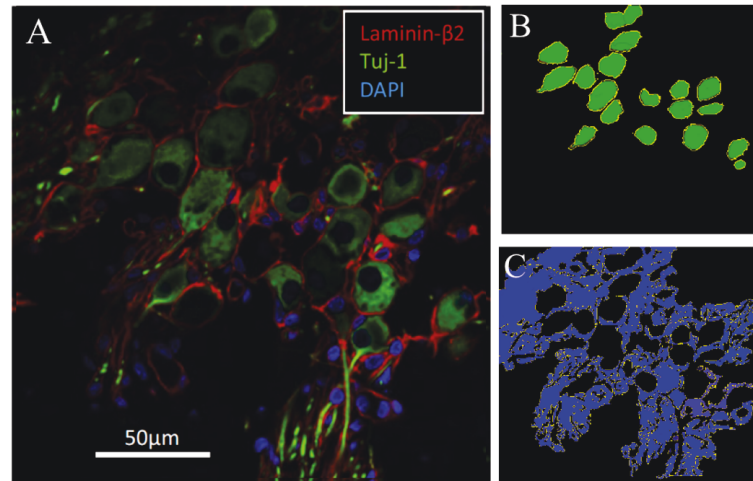


FIGURE 5.2: (A) "False- color representation of Laminin/Tuj-1 immunohistochemistry of human spiral ganglion in the RC: Green: SGNs labelled with Tuj-1, a neural marker, Red: SGCs labelled with Laminin- $\beta$ 2, a marker for basement membrane surrounding glial cells, Blue: cell nucleus labelled with DAPI, a DNA marker, Black: not labelled but defined as an extracellular medium" reproduced and adapted from [93] with permission from Elsevier, (B) Segmented SGNs, (C) segmented tissues.

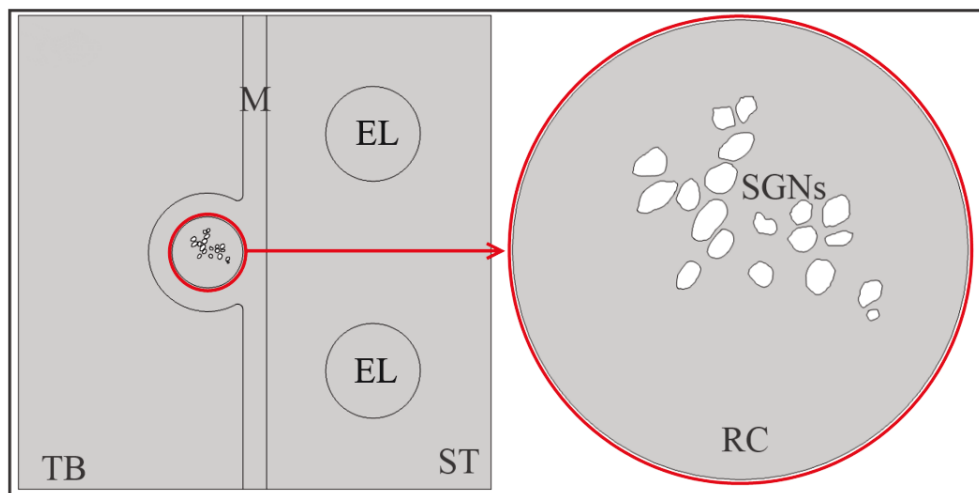


FIGURE 5.3: 2D computational domain embedded with contours of SGNs in the RC (shown in the magnified red circle). M-Modiolus, EL-Electrode, ST-Scala tympani, TB-Temporal bone, SGNs-Spiral ganglion neurons, RC-RC.

### 5.3.1 Allocation of electric conductivities to the tissues

Electric conductivities are assigned to various tissues according to their color code in the selected image. To do so, an immunohistochemistry image of the RC shown in Figure 5.2 (A) is imported into COMSOL using an inbuilt 'image import' function. This function, indicated by  $Im(x, y)$  in equation (5.1), converts pixel intensity data of the input image into normalized RGB (Red-Green-Blue) color code as shown in Figure 5.4. After obtaining the color threshold of each tissue, the electric conductivity of each indicated tissue is assigned as shown in equation (5.1).

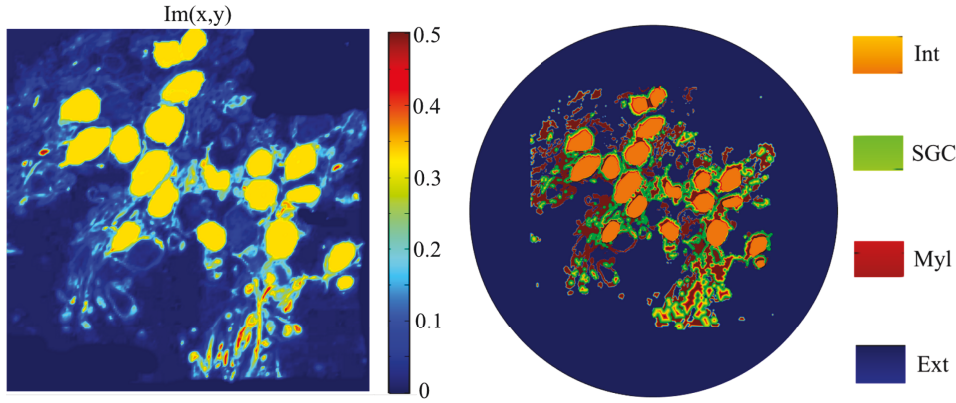


FIGURE 5.4: (Left) Rainbow representation of the imported image in COMSOL where the pixel data of the image are stored as normalized RGB values in  $Im(x, y)$ . (Right) Electric conductivity distribution of corresponding tissues in the RC as per equation (5.1).

$$\sigma_{tissue} = \begin{cases} \sigma_{int}, & 0.3 < Im(x, y) \leq 0.5 \\ \sigma_{SGC}, & 0.15 < Im(x, y) \leq 0.3 \\ \sigma_{Myl}, & 0.05 < Im(x, y) \leq 0.15 \\ \sigma_{Ext}, & Im(x, y) \leq 0.05 \end{cases} \quad (5.1)$$

Here  $\sigma_{int}$ ,  $\sigma_{SGC}$ ,  $\sigma_{Myl}$ , and  $\sigma_{Ext}$ , indicate the electric conductivities of intracellular medium, satellite glial cell layer, myeline layer, and the extracellular medium respectively.

#### Electric conductivity of satellite glial cells

As discussed earlier, SGCs form a non-uniform layer that could act as an additional membrane around each SGN. As a consequence, the electric conductivity of the SGC layer could profoundly affect the induced transmembrane potential and thereby the stimulation profile of the SGNs. Therefore, the allocation of proper electric conductivity to the SGC layer is crucial. However, the unique conductivity values for the human sensory glial cells, especially for the SGCs in the RC, are not readily available in the literature. Even though

TABLE 5.1: Electric conductivity values of sub-domains.

Sub-domain	Electric conductivity (S/m)
Platinum electrode	$9 \times 10^6$
Tympanic medium	1.43
Modiolus bone	0.0334
Temporal bone	0.016
$\sigma_{int}$	0.31
$\sigma_{Myl}$	$3.45 \times 10^{-6}$
$\sigma_{Ext}$	1.2

general dielectric properties of various glial cells are available in the literature, large discrepancies in the electric conductivity values are persistent. For example, in [173, 174, 175] authors suggest that the electric conductivity of glial cells is two to ten times lower than that of the neuronal soma. But it was reported in [176] that the cultured human glial cells show much higher electric conductivity than that of the soma membrane. As suggested in [177], diverging experimental setups with different sample preparation methods, and various measuring errors could have arguably resulted in the discrete conductivity values.

Three hypothetical cases have been considered to study the effect of discrete conductivity values of the SGCs on the transmembrane potential of SGNs. The electric conductivity of an SGC layer is assumed to be ten times lower, equal, and ten times higher than that of the soma. The electric conductivity values of remaining computational sub-domains are given in Table 5.1.

$$\sigma_{SGC} = \begin{cases} 0.4 \times 10^{-8} \text{ (S/m)}, & \text{Case1,} \\ 4 \times 10^{-8} \text{ (S/m)}, & \text{Case2,} \\ 40 \times 10^{-8} \text{ (S/m)}, & \text{Case3.} \end{cases}$$

### 5.3.2 Tissue classification in the Rosenthal's canal

In the present study, the tissues delineated by typical protein markers in Figure 5.2 (A) are classified into two groups based on their vicinity to the SGNs. The SGCs which enwrap the SGNs are classified as Group-1 tissues. All remaining tissues such as myelinated central axons, Schwann cells, and

type-2 SGNs are classified as Group-2 tissues. This classification allows categorical investigations to find how each tissue group affects the electric field distribution in the RC. This approach is also useful to estimate the effect of tissue density on the electric field distribution in the RC. Following three Scenarios have been considered for the systematic study:

- **Scenario1:** In this Scenario, a homogeneous extracellular medium has been considered in the RC. This Scenario is generally useful to qualitatively replicate the state-of-the-art *in silico* model predictions.
- **Scenario2:** In this Scenario, the extracellular medium contains only Group1 tissues. This Scenario investigates whether the SGC layer alone affects the induced transmembrane potential of SGNs. Since the pathology, aging or injury to the cochlea could cause the depletion of SGC. As a consequence, the resultant change in the dielectric properties of the SGC layer could alter the firing behavior of SGNs.
- **Scenario3:** In this Scenario, the extracellular medium contains both Group1 and Group2 tissues. In addition to the SGC layer, the tissue mass present in the extracellular medium could also alter the electric field distribution in the RC. Further, the pathology, drugs, age and electric stimulation could modify the density of tissues in the RC. As a consequence, any change in the firing pattern of the SGNs could influence the hearing sensation of CI recipients.

## 5.4 Simulation

Mapping the electric conductivity in the computational domain based on the color code of the tissues enables the implementation of tissue heterogeneity in the model. A major advantage of this method is the ease of inclusion of dielectric properties of complex microstructures in the simulation which would be cumbersome in any other way. However, since the edges of the microstructures are not present in the model, the conductivity mapping based on equation (5.1) could result in interpolation of conductivity values at the interface of the two tissues. Nevertheless, to some extent, the finest mesh could avoid the interpolation of tissue conductivity values in the domain. Further, utmost care has been taken to retain the realistic shape of the SGNs by manually seeding the required number of elements on the boundaries of SGNs. The element growth rate is kept minimum to ensure a dense mesh at the vicinity of SGN boundaries. All domains are meshed by using a predefined-mesh option in COMSOL. Figure 5.5 shows the resultant mesh of the computational domain. Though extremely fine, the automatic free mesh generated by COMSOL could not ensure enough mesh points at the vicinity of spatial coordinates of the randomly distributed tissues. As a result, an obvious interpolation incurred especially on the tissue interfaces that are far from the boundaries of the SGNs (shown by the white boxes in the zoomed RC in Figure 5.5).

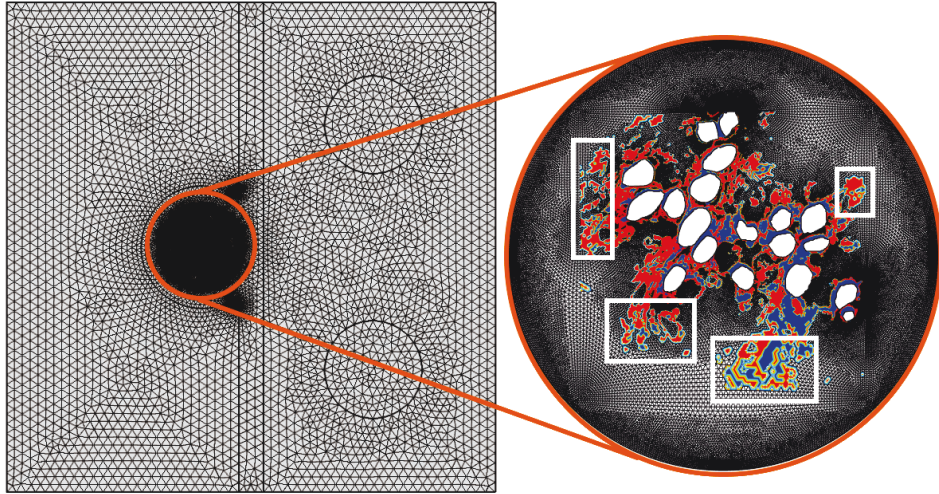


FIGURE 5.5: An automatic free mesh generated by COMSOL resulted in 251,030 mesh elements in the computational domain. White boxes in the zoomed RC show the interpolation of the electric conductivity at the tissue interfaces.

To handle this issue more efficiently, a customized local mesh refinement on the thin tissues was performed with the following constraints.

$$\text{Mesh size} = \begin{cases} \text{Extremely fine on SGC layer,} & 0.15 < Im(x, y) \leq 0.3, \\ \text{Fine on myeline layer,} & 0.05 < Im(x, y) \leq 0.15, \\ \text{Normal on Extracellular medium,} & Im(x, y) \leq 0.05. \end{cases} \quad (5.2)$$

The final mesh of the computational domain using equation (5.2) is shown in Figure 5.6 (Fm). Further, a few more test trails with different mesh parameters have been performed based on equation (5.2). Mesh statistics of all test trails along with the resultant meshes are shown in Figure 5.6 (m1)–(m5). The effect of conductivity interpolation on the transmembrane potential of an SGN in three stated Scenarios is shown in Figure 5.6 (A) and (B).

The finite element mesh at the vicinity of the SGNs remained dense in all mesh cases due to numerous mesh points on the cell boundaries. As a results, in Scenario1 where the extracellular medium is homogeneous, all mesh cases have yielded the same transmembrane potential on the SGN. However, with each successive mesh case in Scenario2 and Scenario3, the coarser the mesh becomes, the larger the interpolation errors occurred. As a result, the induced transmembrane potential of the SGN varied significantly. This implies, the minimization of the interpolation of conductivity values in the model is necessary to obtain a reliable solution. The simulation results obtained by the best mesh (Figure 5.6 (Fm)) that could minimize the interpolation of the tissue conductivity are presented in the results section. Simulation parameters such as boundary conditions for the present study are similar to those described in previous chapters.

## 5.4. Simulation

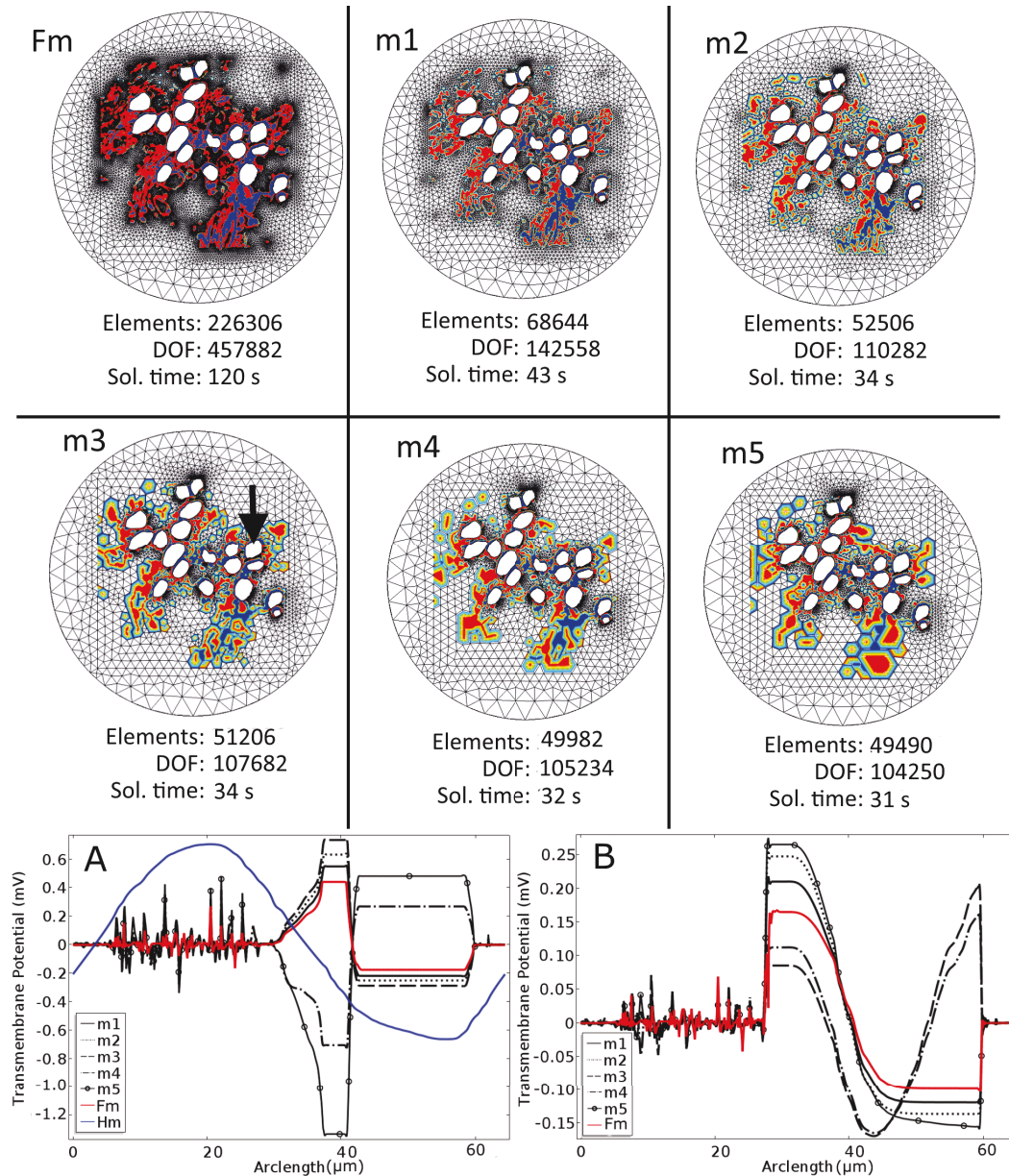


FIGURE 5.6: Customized local mesh refinement on the thin tissues for different mesh cases. Mesh statistics are given for the whole computational domain. (Fm) Final mesh accepted for the simulations. (m1–m5) Five different mesh cases obtained by the successive increment of minimum element size by the factor of 2 on the SGC layer, and by the factor of 4 on the myeline layer. Conductivity distribution of the myeline tissues and the SGC layers is shown in *red* and *blue* color code, respectively, while all other intermediate colors in m1–m5 indicate interpolation errors. (A) and (B) show the induced transmembrane potential of an SGC (marked by the black arrow in m3) for Scenario3, and for Scenario2, respectively. (Hm) Transmembrane potential induced on the SGN in all mesh cases for Scenario1.

## 5.5 Results

The simulation results for each stated Scenario are presented in the following sections.

### 5.5.1 Scenario1

Figure 5.7 (A) and (B) shows the electric potential distribution and electric field distribution in the RC. The electric potential in the RC is varied from 0.431 V to 0.441 V. Since the RC contains a homogeneous extracellular medium, all SGNs respond like suspended biological cells exposed to the uniform electric field (compare the streamline plot). In this Scenario, the induced transmembrane potential depends explicitly on the cell morphology. This can be seen from Figure 5.7 (C) where C1–C4 are located at roughly 400  $\mu\text{m}$  from the electrode. The corresponding maximal transmembrane potential induced on the SGNs, for example on C1 and C4 (0.2 mV and 0.7 mV respectively), varied proportionally to their effective radius (3.9  $\mu\text{m}$  and 10.3  $\mu\text{m}$  respectively). Here the 'effective radius' of a cell is defined as the radius calculated by assuming the arc length of an arbitrary cell as the perimeter of a circle. An analytical expression to estimate the transmembrane potential of biological cells having arbitrary shapes, such as the shape of SGNs in the present study, is not available. Nevertheless, the proportionality between the effective radius of a cell and the corresponding induced transmembrane potential is apparent from the above results.

Further, the placement of CI electrode in the scala tympani which determines the SGN–electrode distance was considered as one of the most influencing factors of the CI output [159, 178, 179, 180, 181]. Since any accidental electrode insertion into the scala vestibule could damage the microstructure of the cochlea, the possibility of endosteal cochlear implants was discussed in [159, 182]. Figure 5.7 (D) shows the proportionality between the induced transmembrane potential and the SGN–electrode distance. Since C2, C8, and C10 have similar shape (effective radius  $\approx 8.5 \mu\text{m}$ ), the variance in the maximal transmembrane potential induced on these SGNs (0.65 mV, 0.52 mV, and 0.41 mV, respectively) can be attributed to the variance in the SGN–electrode distance (414  $\mu\text{m}$ , 486  $\mu\text{m}$ , and 533  $\mu\text{m}$ , respectively).

Figure 5.8 (A)–(D) show the effect of cell shape on the induced transmembrane potential. For example in Figure 5.8 (A), and (B) the induced transmembrane potential on ellipse-like SGNs (C3, C14) is different from that on circle-like SGNs (C7, C13). Theoretical, experimental, and numerical studies suggest that the induced transmembrane potential may vary with the shape and orientation of the cells [105, 107, 183]. Further, in spite of having the same shape and size, the induced transmembrane potential on C11 is more than that on C10. This could be due to the mutual electric shielding observed in closely packed cells [184].

To summarize, in the presence of a homogeneous medium in the RC, the induced transmembrane potential on SGNs depends on (a) size of the SGNs,



## 5.5. Results

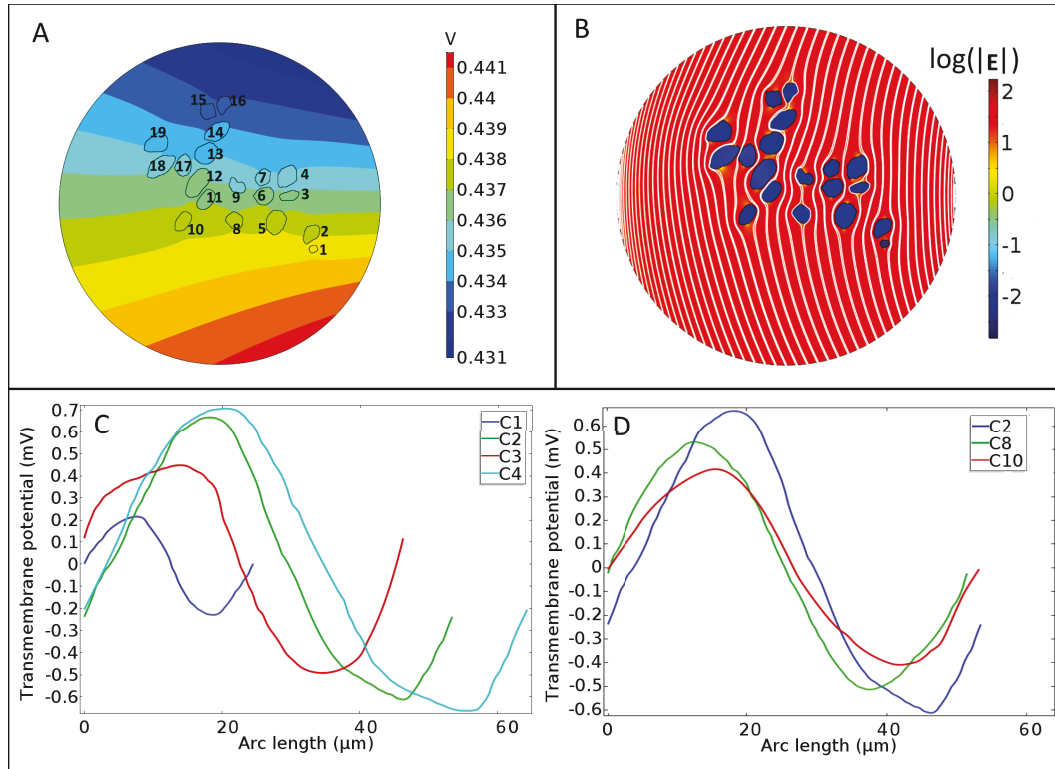


FIGURE 5.7: Simulation results for Scenario1 in which the RC contains a homogeneous extracellular medium. (A) Electric potential distribution in the RC and numbers 1–19 indicate the reference numbers for SGNs. (B) The surface plot represents the electric field distribution while white streamlines show almost uniform field in the RC. (C) The induced transmembrane potential on C1–C4; though the cells are situated in the same distance from the electrode, the maximal transmembrane potential on each SGN varied proportionally to the respective cell size. (D) The induced transmembrane potential on C2, C8, and C10; though the cells have the same size, the maximal transmembrane potential on each SGN varied proportionally to the distance of respective cell from the electrode.

(b) electrode–SGN distance, (c) cell shape and orientation, and (d) cell packing. In addition to the simulation results discussed in Chapter 3, these results provide a detailed picture of the sub-threshold phenomenon which has not been considered in the state-of-the-art models.

### 5.5.2 Scenario2

In this Scenario, number of SGCs envelop an SGN depending on its surface area in the RC. As suggested in [185], a discontinuous SGC layer of non-uniform thickness composed of gap junctions plays a crucial role in the survival of SGNs. In the context of present *in silico* modeling, not only the discrete dielectric properties of the SGC layer but also its nonuniform thickness could affect the transmembrane potential of an SGN. Moreover, no two SGNs may have the same nonuniform SGC layer with same thickness. Hence, the simulation results represent the cumulative effect of the electric conductivity

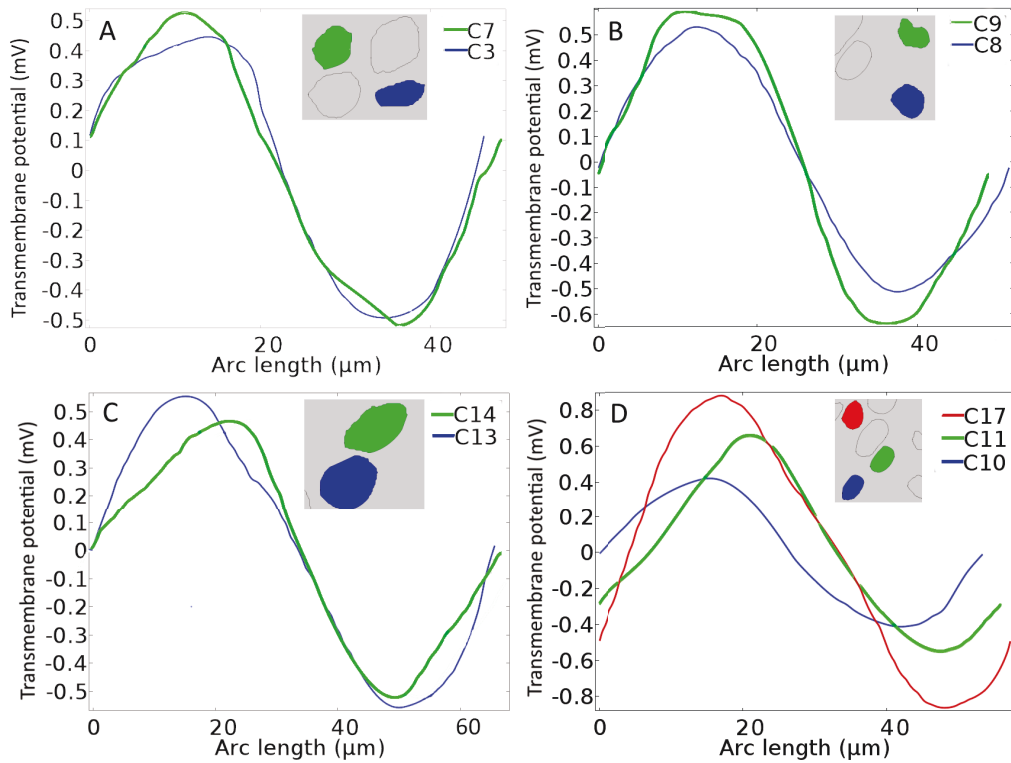


FIGURE 5.8: Effect of SGN shape on the induced transmembrane potential ( $V_m$ ) of indicated SGNs in Scenario1. (A) and (C) Maximal  $V_m$  on ellipse-like cells is lesser than that on circle-like cells. (B) and (D) The induced  $V_m$  on irregular shape SGNs is more than that on the regular shape SGNs. Corresponding cell shapes are depicted by color coded SGNs in the inset.

and the characteristic nonuniform thickness of the SGC layer around the SGNs. Figure 5.9 (A), (B), and (C) show the potential distribution, electric field distribution, and conductivity distribution in the RC. Unlike in Scenario1, the presence of SGCs around SGNs in Scenario2 resulted in nonuniform electric field distribution (compare the streamlines of the electric field in (C) with Figure 5.7 (B)) which could affect the induced transmembrane potential.

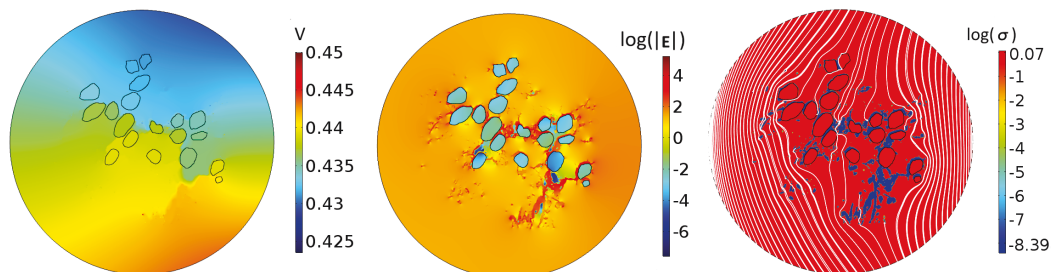


FIGURE 5.9: (A) and (B) Potential distribution and electric field distribution, respectively, in the RC for Scenario2. (C) Conductivity distribution in the RC. White lines represent the electric field streamlines.

The effect of electric conductivity of the SGC layer on the induced transmembrane potential of the SGNs for the three stated cases is shown in Figure 5.10. Three SGNs *viz.* C4, C5, and C6 which have similar size, shape, and vicinity to the electrode have been chosen to interpret the results. From Figure 5.10 (A), since the induced transmembrane potentials on C4–C6 are also almost the same in Scenario1, the apparent effects of cell morphology would be negligible in the comparative study. Figure 5.10 (B), and (C) shows a noticeable increase in the transmembrane potential induced on C4 and C5 for case3 where the conductivity of the SGC is assumed ten times higher than that of the cell soma. However, in case1 and case2 where the conductivity of SGC was assumed ten times lower, and equal to that of the SGN, respectively, the induced transmembrane potential has not changed significantly.

A direct study relevant to the present *in silico* model is not available in the literature to compare the stated results. Nevertheless, Klee and Plonsey [186] numerically and analytically studied the effect of extracellular stimulation of a spherical cell having a non-uniform membrane patch. They argued that a low resistive membrane patch shifts the intracellular potential towards the extracellular potential which increases the transmembrane potential of the cell. In [186] the authors assumed a single isolated spherical cell with the intracellular and extracellular medium having equal conductivity where the low resistive patch occupies only 0.3% of the total cell area. Though the model assumptions in [186] differ a number of ways with the present model, the results of the present study are qualitatively consistent with the referred study results. This implies that the presence of a low resistive membrane layer or membrane patch such as nonmyelinated Schwann cells at pre and post somatic regions of the SGN [93] could favor the signal initiation.

In contrast to above results, from Figure 5.10 (D) a high conductive SGC layer has little effect on the maximal transmembrane potential of C5 in case3. As discussed in [186], the current entering through a high conductive patch should pass out from the remaining low conductive membrane. Thus, the low conductive cell membrane controls the overall behavior of the cell and allows only a small amount of inward current to maintain the continuity. This implies, the nonuniform SGC layer with variable thickness, and the surface area it occupies on an SGN could profoundly affect the response of the SGN to the applied electric field. Figure 5.10 (E) shows the distribution of the SGC layer around the SGNs and a very fine mesh on the SGC layer indicates the absence of interpolation errors.

### 5.5.3 Scenario3

In this Scenario the SGNs in the RC are surrounded by group1 and group2 tissues. The proximal tissues to the SGNs (group1 tissues) show a profound effect on the induced transmembrane potential of the SGNs. Most of the SGNs are often run over by randomly distributed central axons in such a way that they leave longitudinal impressions on the cell body (Figure 6 in [93]). Since the electric conductivity of myelinated central axons is different from that

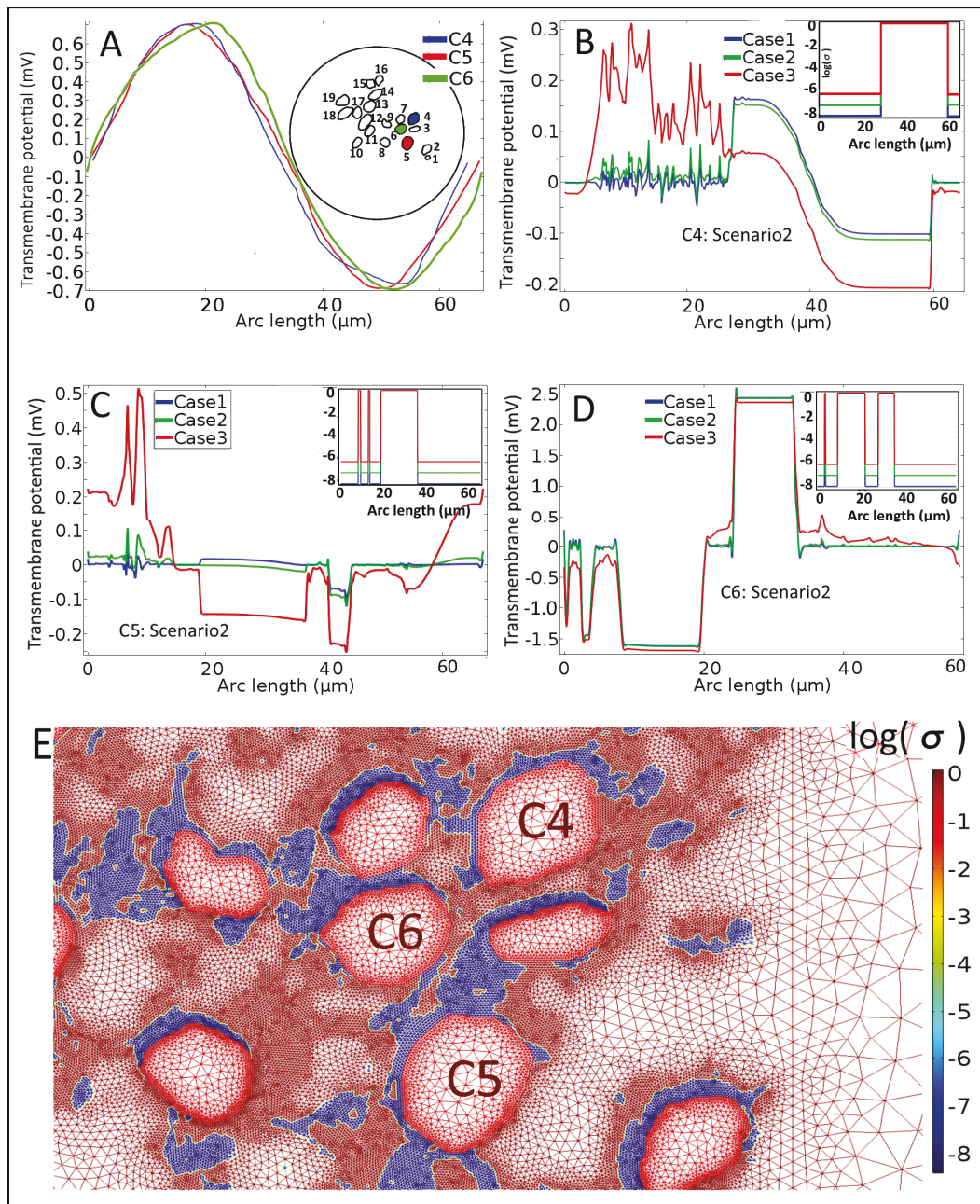


FIGURE 5.10: Effect of SGC conductivity on the transmembrane potential ( $V_m$ ) of SGNs. (A)  $V_m$  induced on C4, C5, and C6 in Scenario1. (B)–(D) Induced  $V_m$  on C4, C5, and C6 respectively in three stated cases; the induced  $V_m$  is different in case3 due to the high conductive SGC layer around the SGNs. (E) SGC layer distribution (blue) around the SGNs. High quality mesh at the interfaces ensures the absence of conductivity interpolation.

of group1 tissues, the conductivity distribution around each SGN would be different from that of its neighboring SGNs.

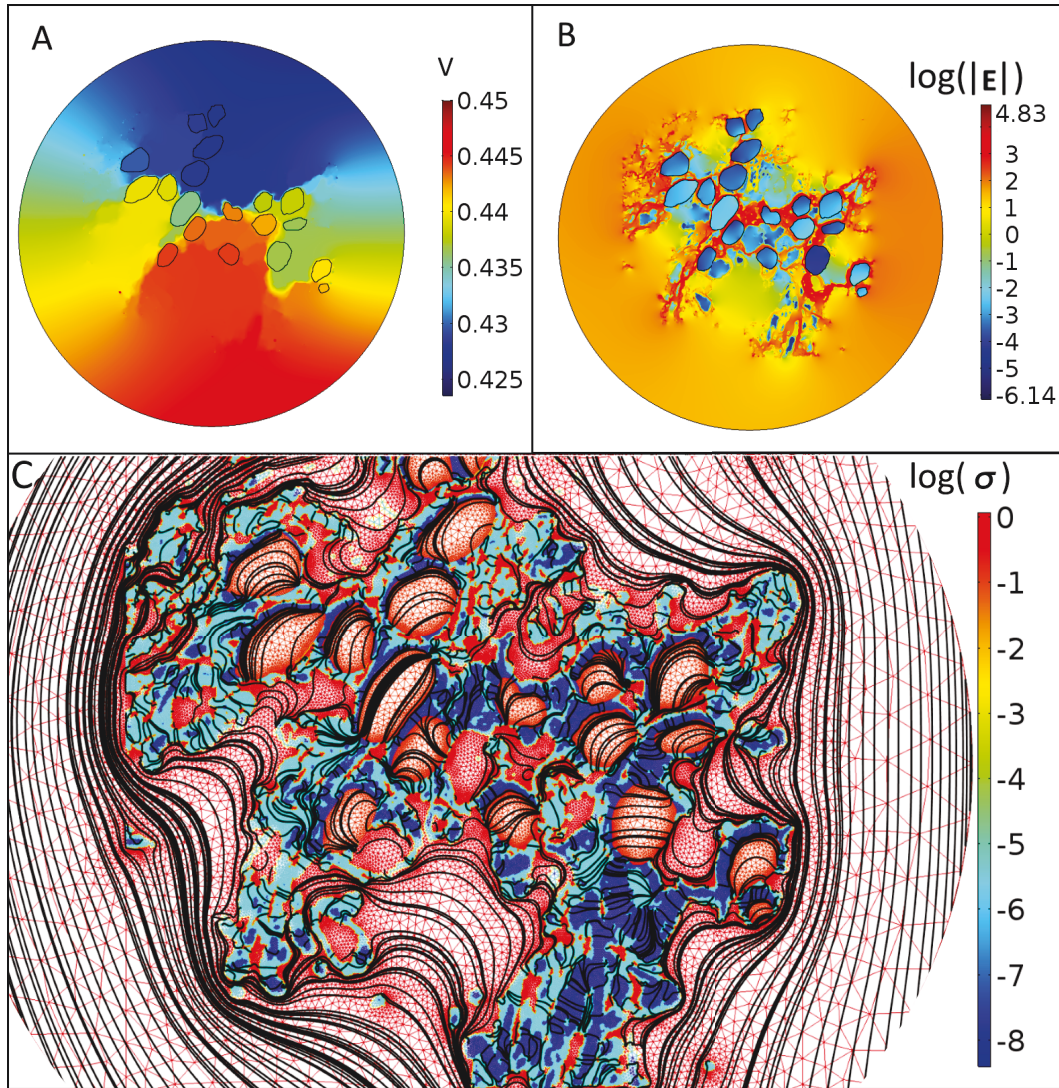


FIGURE 5.11: (A) and (B) Electric potential and electric field distribution (shown on the logarithmic scale) respectively in the RC for Scenario3. (C) Heterogeneous spatial distribution of group1 and group2 tissues and respective electric conductivity values (shown on the logarithmic scale). Black stream lines represent the electric field lines in the RC for Scenario3.

In other words, an SGN responds against the applied electric field like as if the cell membrane has multiple patches of different conductivity *viz.* SGC, cell membrane, group2 tissues, and extracellular medium. As discussed in the previous section, the active area occupied by each patch on the membrane determines the stimulation profile of that SGN. Since group2 tissues have a random distribution in the RC, no two SGNs would experience the same conductivity matrix around them. This could be one of the reasons for the dynamic firing behavior of SGNs.

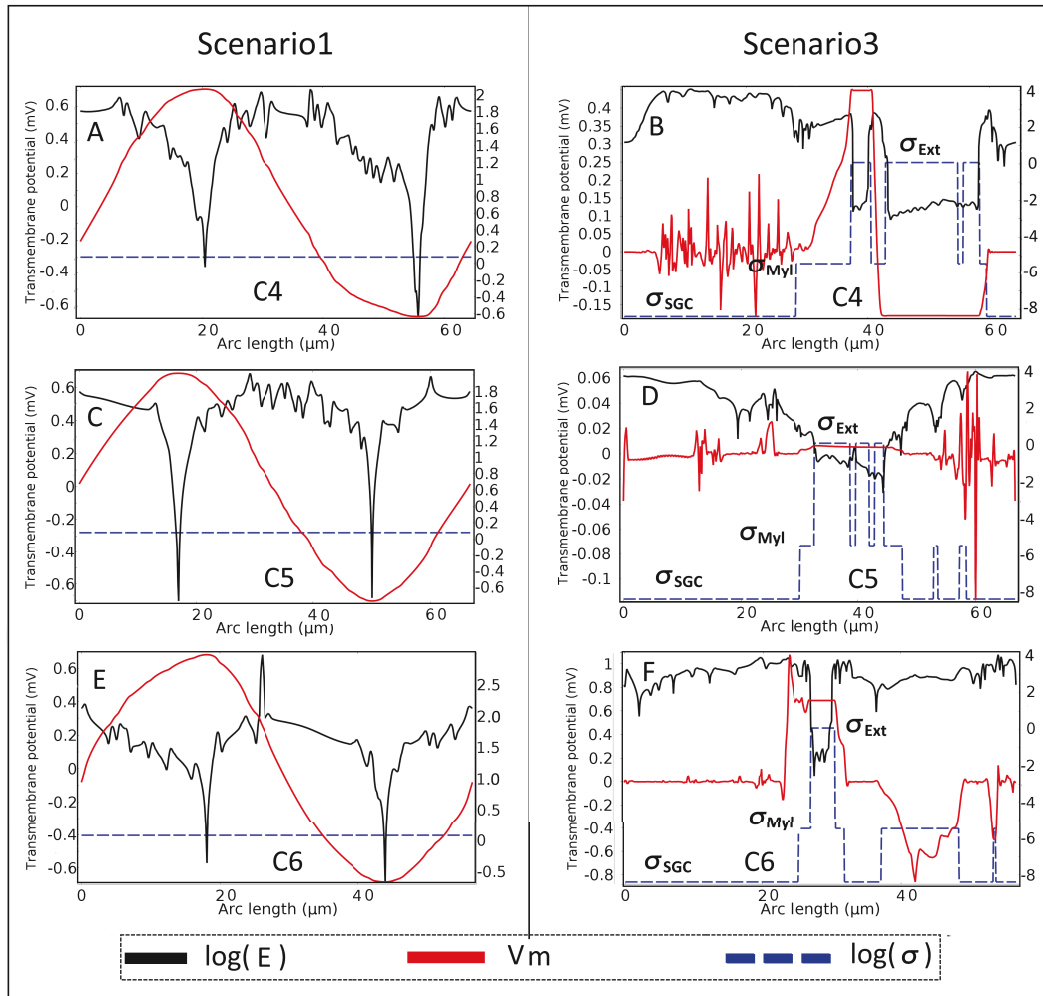


FIGURE 5.12: A comparative depiction of the induced transmembrane potential ( $V_m$ ) in Scenario1 and Scenario3. Notably, the maximal  $V_m$  in Scenario3 is completely different from that in scenario1 in terms of magnitude and location on C4, C5, and C6.

Figure 5.11 (A), (B), and (C) depict the potential distribution, electric field distribution, and the conductivity distribution, respectively, in the RC for Scenario3. A significant change in the potential distribution and the electric field distribution is observable in Scenario3 compared to Scenario1. Since the dense mesh at the tissue interfaces ensures the absence of conductivity interpolation errors, the substantial variation in the electric field distribution around the SGNs could be attributed to the sudden change in the electric conductivity at the tissue interfaces. Besides, many field 'sinks' and 'hot spots' are formed around the SGNs due to the heterogeneous distribution of the tissues. This atypical electric field distribution in Scenario3 is critical to understand the CI functionality. Since the impressed current chooses the least resistive path to reach the counter electrode, dense electric field lines (black lines in Figure 5.11 (C)) away from high resistive tissues can be seen in the extracellular medium. Further, the effective conductivity of heterogeneous tissues around each SGN would form a shunt-like low resistive path that

could result in strong density variation in the electric field lines across the SGNs.

Figure 5.12 shows the essential differences between the simulation results of electric stimulation of intact SGNs obtained by assuming a homogeneous medium and a heterogeneous medium in the RC. For example, from Figure 5.12 (A), (B), and (C), since the induced transmembrane potential on C4, C5, and C6 is almost the same in the case of a homogeneous medium in the RC, the model predicts the uniform excitation of all three cells for Scenario1. For instance, if 0.4 mV is assumed as the sub-threshold potential that could cross the excitation threshold, then all three SGNs would fire action potentials in Scenario1. However, due to the heterogeneous distribution of group1 and group2 tissues in the RC, the SGNs experience distinct electric conductivity matrix and thereby different electric field distribution around them in Scenario3. As a consequence, only one SGN (C6) could fire the action potential in Scenario3. Also, from Figure 5.13 and Figure 5.14, only eight out of nineteen SGNs fire action potentials in Scenario3 whereas almost all SGNs would fire action potentials in Scenario1 for the sub-threshold potential of 0.4 mV. Further, though C1, C2, C3, and C7 are nearer to the electrode, the induced transmembrane potential on them is lesser than that on C17, and C18 which are farther to the electrode. This implies that the proportionality of the induced transmembrane potential with the cell morphology, and the electrode distance does not always hold in case of Scenario3.

Above results could also explain the 'dynamic firing' behavior of SGNs observed in *in vitro* studies [187, 188, 189, 190, 191]. For example, the referred studies state that the SGNs with similar kinetic features such as AP duration, peak voltage could substantially differ with their threshold voltage.

In other terms, two SGNs taken from two different accommodations may not have a similar excitement profile for a given stimulation. These endogenous firing properties of SGNs are attributed to the heterogeneous distribution of slow and fast voltage gated sodium (Nav) and potassium (Kv) ion channels on the SGNs with respect to the cell accommodation. However, they could not explain the endogenous firing properties of SGNs in the same accommodation observed in *in vivo* studies. Apparently, the stated *in vitro* studies could not capture the tissue heterogeneity, since those studies are conducted on isolated SGNs. Within the scope of the present study it can be stated that even though the electrophysiological properties such as ion channel distribution of the SGNs are similar in a given accommodation, the excitement of SGNs could significantly vary with the degree of heterogeneity around each SGN.

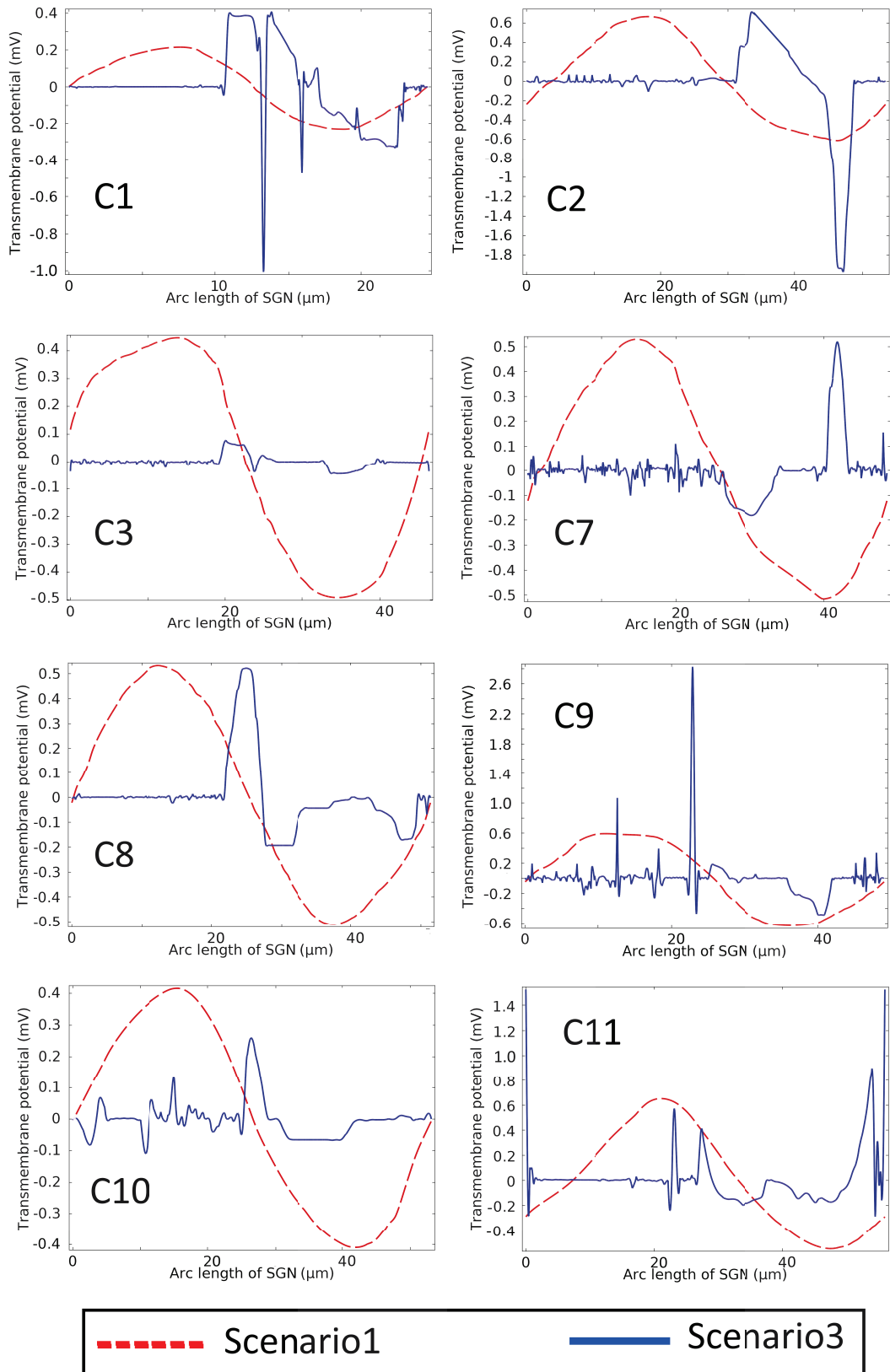


FIGURE 5.13: Comparison of the induced transmembrane potential of indicated SGNs in Scenario1 and Scenario3. Stochastic response of the SGNs to the applied electric field can be seen in Scenario3.



## 5.5. Results

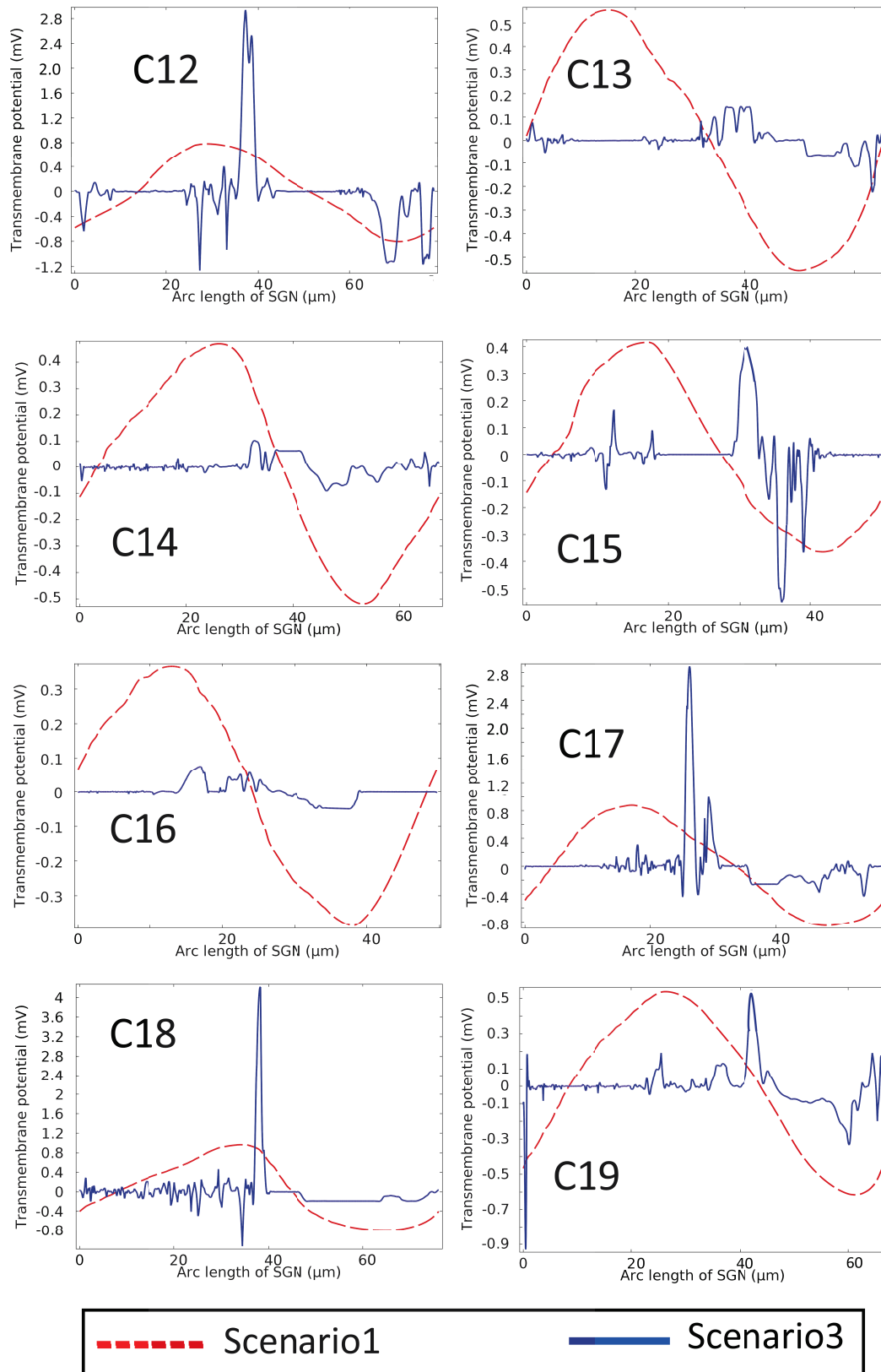


FIGURE 5.14: Comparison of the induced transmembrane potential of indicated SGNs in Scenario1 and Scenario3. Stochastic response of the SGNs to the applied electric field can be seen in Scenario3.

Another important observation from the comparative study of Scenario1 and Scenario3 is the shifting of signal initiation sites on the SGNs. If a point where the induced transmembrane potential is maximal on the SGN is assumed as the signal initiation site, then the signal initiation sites for C4, C5, and C6 were located at 20  $\mu\text{m}$ , 19  $\mu\text{m}$ , and 19  $\mu\text{m}$  of arc length, respectively, in Scenario1. However, the signal initiation sites are shifted to 40  $\mu\text{m}$ , 60  $\mu\text{m}$ , and 23  $\mu\text{m}$  arc lengths of respective SGNs in Scenario3. The shifting of signal initiation sites on the SGNs could be due to the modified electric field distribution around the SGNs in Scenario3. Electric conductivity distribution around the SGNs in three step values on the logarithmic scale is shown in Figure 5.12 (B), (D), and (F). The lowest step represent the conductivity of SGC ( $\sigma_{SGC} = 4 \times 10^{-9}$  S/m as in case1), the middle step represents the conductivity of myeline tissues ( $\sigma_{Myl} = 3.45 \times 10^{-6}$  S/m), and the highest step value represents the conductivity of extracellular medium ( $\sigma_{Ext} = 1.2$  S/m). From Figure 5.12, it can be observed that the electric field has reached its extreme value where the SGN membrane is exposed to extracellular medium. The contact point of the extracellular medium and the SGN membrane could represent the high conductive membrane patch such as a gap junction as reported in [185]. The gap junctions are believed to regulate the ion exchange in the neural cells and thereby lower the sensory thresholds [192, 193]. Hence, the formation of a field 'hot spot' near a gap junction could increase the probability of cell excitation by inducing the maximal transmembrane potential on the SGN (please refer Figure 5.12 (B), (F)). In this case, a 'favorable' orientation of SGN to the applied electric field would play a vital role in determining the fate of the cell excitation. This can be seen from Figure 5.12 (D) where the 'unfavorable' orientation of C5 hindered the possibility of inducing the maximal transmembrane potential at the interface of a gap junction and a 'hot spot'. Above results could provide some new insights into the knowledge of signal initiation sites on the auditory nerve during CI stimulation.

#### 5.5.4 Anisotropic conductivity of group2 tissues

The simulation results show the sensitivity of the model towards the accuracy of the input conductivity values for various tissues. In Scenario2, the assumed variation in the SGC conductivity did not drastically affect the electric field distribution around the cell but significantly altered the induced transmembrane potential. This implies that the response of an SGN to the applied electric field largely depends on the conductivity matrix around it. In this context, when the SGNs are surrounded by a large mass of group2 tissues, the effect of anisotropic conductivity plays a crucial role in determining the excitation profile of an SGN. However, group2 tissues in the present case mainly consist of myelinated central axons which are composed of myelin sheaths and nodes of Ranvier, Schwann cells, and type2 SGNs. Each stated tissue has different anisotropic conductivity ratios, for example, the longitudinal conductivity of a node of Ranvier is ten times higher than its transversal conductivity whereas the myelin sheath has different conductivity ratio. On the one hand, the constituents of group2 tissues are not modeled as geometric subdomains;

## 5.5. Results

---

so the anisotropic conductivity of each tissue cannot be modeled. On the other hand, any specific data such as diffusion tensor imaging data (DTI) in the case of brain tissues which has been serving as a basis for modeling anisotropic conductivity of the tissues [194, 195, 196] are not available for the present study. For these reasons, modeling the accurate anisotropic conductivity of group2 tissues is untenable. However, as a worst case Scenario, a hypothetical conductivity ratio of group2 tissues can be assumed to investigate the qualitative effect of anisotropic conductivity of the tissues on the stimulation profile of the SGNs.

In the present study the isotropic conductivity ( $\sigma_{iso}$ ) of group2 tissues is taken as  $3.45 \times 10^{-6}$  S/m. Since the model is in 2D and the conductivity tensor data of the tissues are not available, a hypothetical diagonal anisotropic conductivity is implemented in the model as defined below

$$\frac{\sigma_{hk}}{\sigma_{iso}} = \begin{cases} \{0.1, 1, 10\}, & \text{if } h = k \\ 0, & \text{otherwise} \end{cases} \quad (5.3)$$

where the indexes  $h$  and  $k$  indicate x- and y- components of the coordinate axis, respectively. From equation (5.3),  $\sigma_{xx}$ , and  $\sigma_{yy}$  stand for the conductivity of the tissues in x-direction, and y-direction respectively in a global Cartesian coordinate system. Further, as a consequence of equation (5.3), two simulation cases would arise *viz.*  $\frac{\sigma_{xx}}{\sigma_{yy}} = 1$  and  $\frac{\sigma_{xx}}{\sigma_{yy}} \neq 1$ . Here  $\frac{\sigma_{xx}}{\sigma_{yy}} = 1$  does not represent the anisotropic conductivity of the group2 tissues per se. Nevertheless, the effect of conductivity variation of group2 tissues on the induced transmembrane potential of SGNs has been studied as the first case. Figure 5.15 (A) shows the transmembrane potential induced on C4 and C6 for one tenth, equal, and ten times of  $\sigma_{iso}$  value taken for group2 tissues. It should be noted that the change in the maximal induced transmembrane potential due to the isotropic conductivity variance of group2 tissues is not identical for C4 and C6. Notably, when the conductivity is taken ten times of  $\sigma_{iso}$ , the maximal induced transmembrane potential increased from 0.45 mV to 0.5 mV for C4 and 1 mV to 3.25 mV for C6. This can be due to the different degree of tissue heterogeneity around the SGNs.

Considering  $\frac{\sigma_{xx}}{\sigma_{iso}} = \{0.1, 1, 10\}$  with  $\sigma_{yy} = \sigma_{iso}$ , and considering  $\frac{\sigma_{yy}}{\sigma_{iso}} = \{0.1, 1, 10\}$  with  $\sigma_{xx} = \sigma_{iso}$ , the variation in the transmembrane potential of C4 and C6 is studied. The simulation results for above-mentioned two different modeling cases of anisotropic conductivity is shown in Figure 5.15 (B) and (C).

These results once again highlight the decisive role of dielectric properties of biological tissues in the *in silico* modeling. It should be noted that the variation of electric conductivity of the tissues in x-direction did not yield the same results when the same variation of the electric conductivity is assumed in y-direction. For example, from Figure 5.15 (B) when  $\sigma_{xx} = 10(\sigma_{iso})$  and  $\sigma_{yy} = \sigma_{iso}$ , the maximal induced transmembrane potential of C4 and C6 is 0.6 mV and 3 mV, respectively. However, from Figure 5.15 (C) when  $\sigma_{yy} = 10(\sigma_{iso})$  and  $\sigma_{xx} = \sigma_{iso}$ , the maximal transmembrane potential induced on C4 and

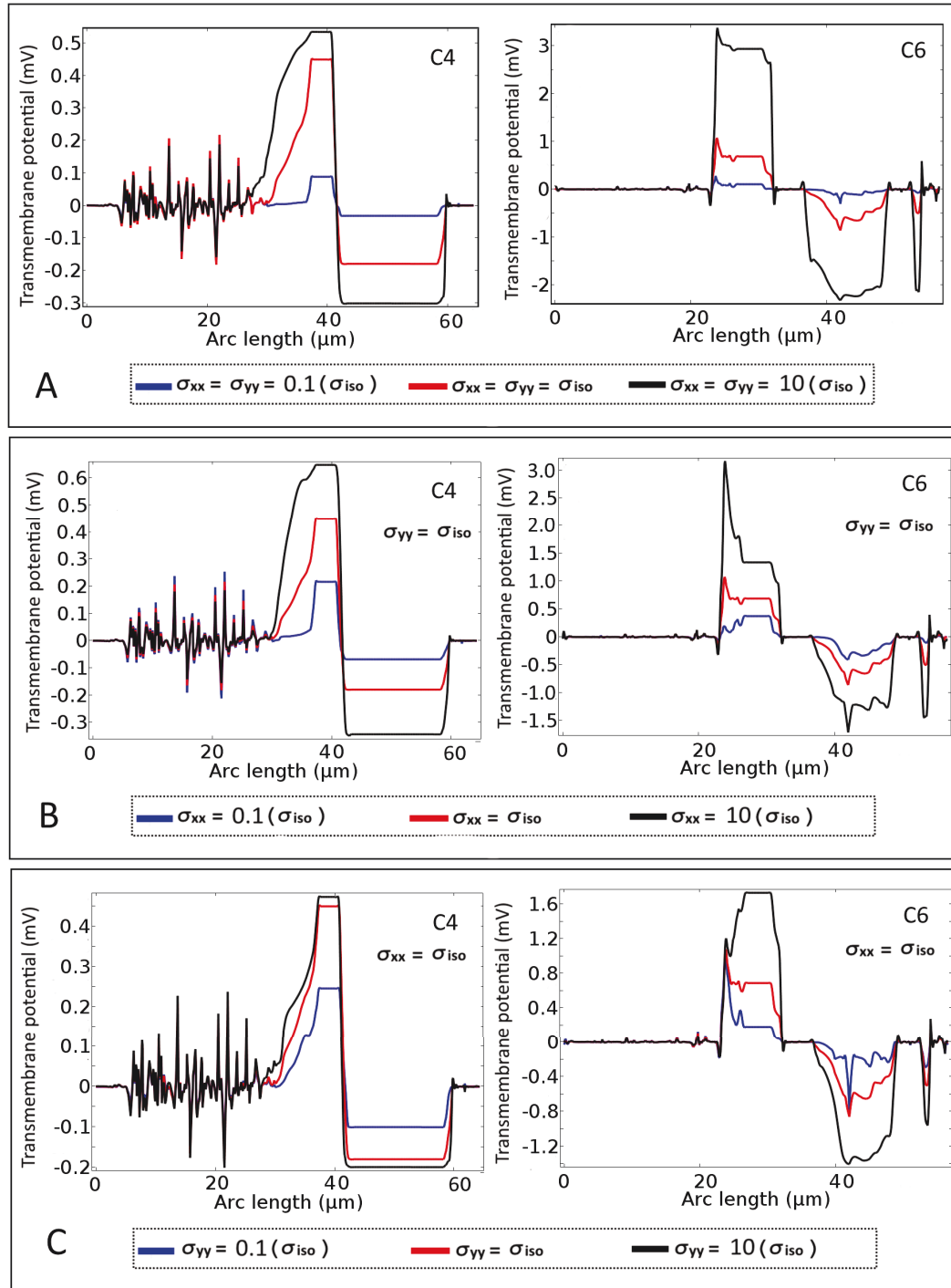


FIGURE 5.15: (A) Induced transmembrane potential ( $V_m$ ) as a function of incremental isotropic conductivity of group2 tissues. (B) and (C)  $V_m$  as the function of incremental anisotropic conductivity assumed for  $\sigma_{xx}$  and  $\sigma_{yy}$  of group2 tissues, respectively, on C4 and C6.

C6 is 0.45 mV and 1.6 mV, respectively. In addition, the depolarized area of cell membrane is also altered in both cases. Apart from tissue heterogeneity, the orientation of tissues could also influence the simulation results [197, 198,

## 5.5. Results

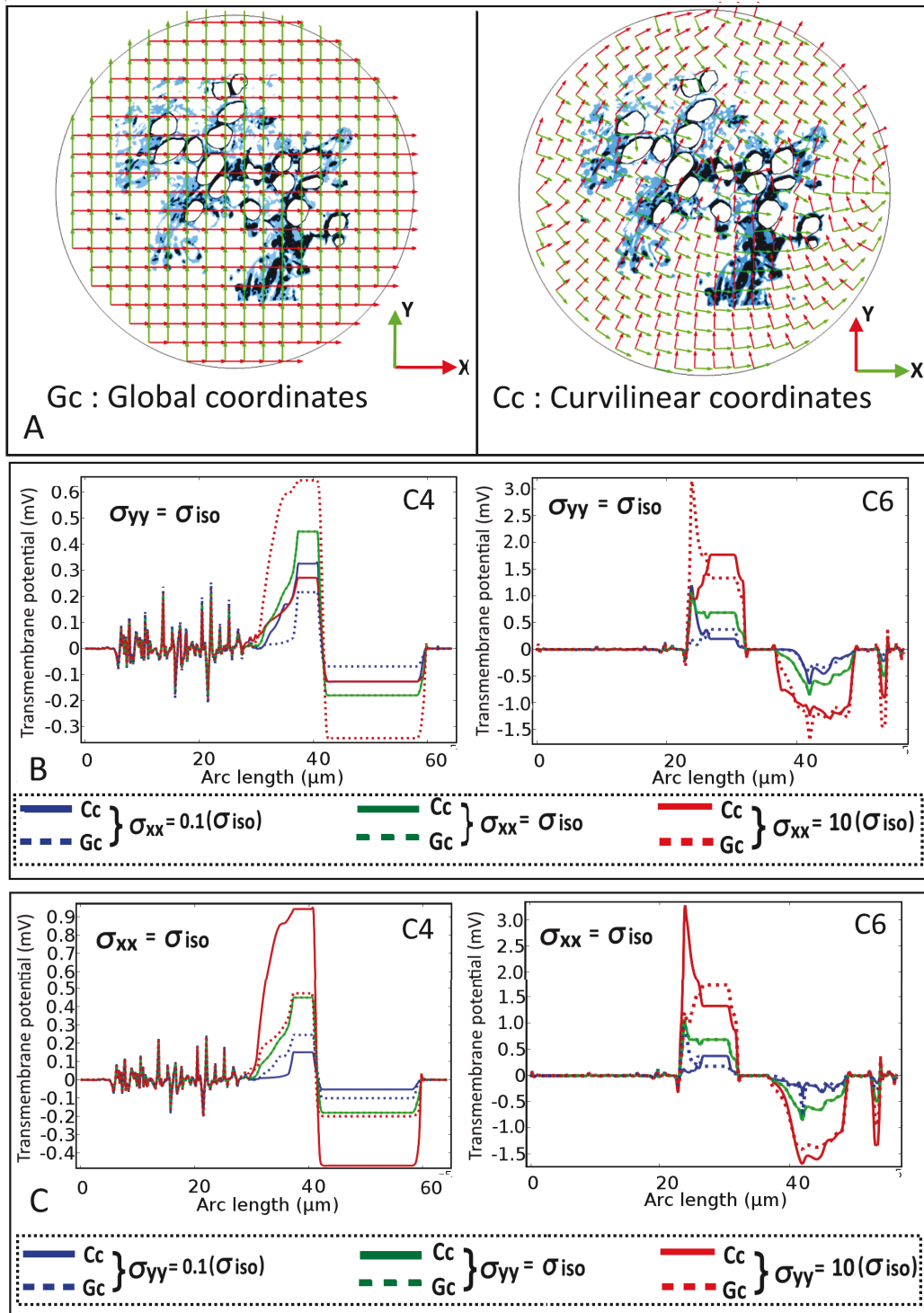


FIGURE 5.16: (A) Global Cartesian coordinates and local curvilinear coordinates in the RC. (B) and (C) Transmembrane potential induced on C4 and C6 when an incremental change is assumed for  $\sigma_{xx}$  and  $\sigma_{yy}$  respectively in both coordinate systems.

146].

Since the anisotropic conductivity is a tensor quantity, the heterogeneous spatial distribution of neural structures may not comply with the global coordinate system. To address this problem, COMSOL offers an option for modeling a local coordinate system namely, a curvilinear coordinate system. The knowledge base and the relevant documentation of the COMSOL software state that a computationally inexpensive method for the implementation of the curvilinear coordinate system is solving the Laplace equation in the domain. The gradient of the scalar quantity that follows the curvature of the area of interest serves as the basis for the curvilinear coordinate system. For further details and examples please refer [199, 200].

Figure 5.16 (A) shows the coordinate mapping of both Cartesian global coordinate system and curvilinear coordinate system in the area of interest. Though the group2 tissues have no specific topology and orientation, unlike the global coordinates the curvilinear coordinates have concurred the distribution of the tissues to some extent. Figure 5.16 (B) and (C) show a comparative depiction of the qualitative and quantitative difference in the induced transmembrane potential on C4 and C6 in both coordinates systems. For example, the incremental change in the conductivity in two cases *viz.*  $\sigma_{xx}$  and  $\sigma_{yy}$  has induced an incremental transmembrane potential on C4 in the global coordinate system. However, for the same change in conductivity, the induced transmembrane potential is decremental in the first case and incremental in the second case in the curvilinear coordinate system. Also, the response of C6 in the cases mentioned above is dissimilar compared to the response of C4. The difference between the results obtained by global and local coordinate systems can be due to the orientation of the tissues. The stochastic response of SGNs has been attributed to the intrinsic heterogeneity of SGNs such as the asymmetric distribution of voltage specific ion channels [185, 201, 190, 191]. Nevertheless, the present study suggests that the anisotropic conductivity and the spatial heterogeneity of group2 tissues could also profoundly affect the cell response to the applied electric field.

### 5.5.5 Tissue depletion in Rosenthal's canal

The pathology of the cochlea that incites the tissue depletion could cause a change in the density of the tissues which would alter the degree of tissue heterogeneity around the SGNs in the RC. Since the dynamic excitation of the SGNs in the presence of heterogeneous tissues would be considered, any change in the tissue density in the RC would implicate a change in the excitation profile of the SGNs.

Six samples of incremental depletion of group2 tissues have been considered to study the effect of tissue depletion on the induced transmembrane potential of the SGNs. Figure 5.17 (A) shows the tissue depletion in the RC for six samples (numbered 1 to 6). The asymmetric depletion of group2 tissues has been considered in the modeling which indicates the death of the neighboring SGNs to the modeled nineteen cells in the RC. Figure 5.17 (B) shows the response of

## 5.5. Results

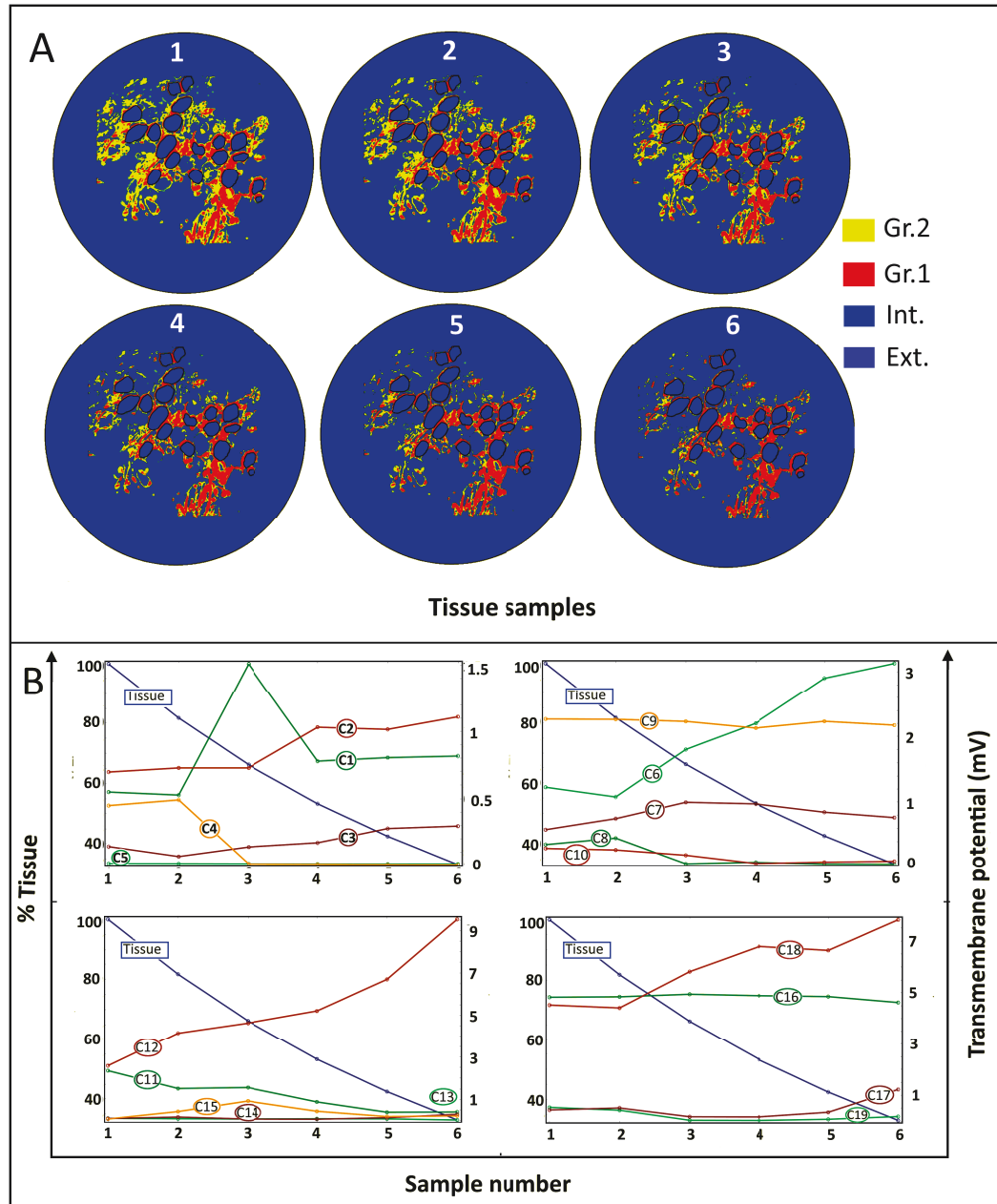


FIGURE 5.17: (A) Six samples of the RC depicting the gradual depletion of group2 tissues. Gr.2–group2 tissues, Gr.1–group1 tissues, Int.–Intracellular medium, Ext.–Extracellular medium. (B) Maximal induced transmembrane potential on the indicated SGNs (inside the circles on the curves) as a function of tissue depletion.

all indicated SGNs for each sample. The maximal transmembrane potential of SGNs varied stochastically with the depletion of the tissues. This indicates that the functionality of the CI would be altered when the density of a tissue varies. Eventually the change in the density of the tissues, especially group2 tissues is inevitable due to the progressive deterioration of the cells [202, 203, 204]. Experimental studies suggest that electric stimulation of the auditory nerve also causes tissue growth as well as tissue depletion in the RC [205].

The performance of the CI would change with the time due to the formation of an unwanted tissue layer around the stimulating electrode that alters the impedance of the electrode [206, 207, 208]. Nevertheless, present results suggest that the performance fluctuations of CI could be the result of the gradual change in the tissue density. For example, considering the tissue density in the sample1 is 100%, for 1 mV of threshold potential, only 4 out of 19 SGNs that is 20% of SGNs would be active. In sample2 where the tissue density is 80%, only 3 out of 19 SGN would be active (18%). However, in sample3 where the tissue density is around 60%, 7 out of 19 SGNs would active. In samples 4, 5, and 6 where the tissue density is 50%, 40%, and 35% respectively, the number of active SGNs would be 7, 6, and 8 for respective samples. If these results are translated to the whole cochlea, the degeneration and the heterogeneity of the tissues could also be considered as the influential factors for the apparent inconsistency in the performance of the CI.

## 5.6 Discussion

The comparative study of Scenario1 and Scenario3 had shown the shortcomings of state-of-the-art *in silico* models in which a homogeneous extracellular medium was assumed in the RC. Unlike Scenario1 where the response of the SGNs to an applied electric field depends primarily on the SGN morphology and SGN–electrode distance whereas in Scenario3 the stimulation profile of the SGNs varies with the degree of tissue heterogeneity, tissue density and the electric properties of tissues around the SGN. Nevertheless, cell orientation plays a pivotal role in both Scenarios. In the scope of the present study, it can be concluded that the presence of various tissues in the RC is not negligible, indeed, should not be neglected if an *in silico* model intends to replicate the actual phenomenon of CI stimulation.

Variation in the electric conductivity values of the SGC layer around the SGN which was studied under three hypothetical cases in Scenario2 also profoundly affects the induced transmembrane potential of SGNs especially when the SGC layer behaves like a low resistive layer. This prompts the importance of implementing accurate dielectric properties of tissues in the model. Since diverse biochemical and biophysical components exist across the human samples, determining unified dielectric properties of various tissues with universal applicability demands large data. Nevertheless, a few analytical and numerical methods in the electric stimulation paradigm to quantify the effect of uncertainties in the input parameters such as electric conductivity of neural tissues are available in the literature [209, 195].

Interestingly, the interpolation of electric conductivity can be quantized by assuming a low conductive layer similar to the electrical double layer at the interfaces of various tissues in the RC. A rigorous theoretical framework for such assumption is not available for the present case, but the concept of an electric double layer at the interface of tissue membrane and the electrolyte in the extracellular matrix has been discussed in the literature [210, 211, 212, 213].



## 5.6. Discussion

The electric conductivity distribution of heterogeneous tissues can be modeled as a continuous function of pixel intensities as shown in Figure 5.18 (A). The steep dip at the tissue boundaries indicates an electric double layer with the conductivity of minimum two orders of magnitude lower than the least conductivity of the tissues at the interface. This approach is also useful to apply other boundary conditions whenever necessary on the tissue boundaries without modeling the actual geometry of the tissues. The simulation results obtained by implementing the electric conductivity of tissues as a continuous function of the pixel data of the input image in comparison with the implementation of the conductivity values of the tissues based on equation (5.1) is shown in Figure 5.18.

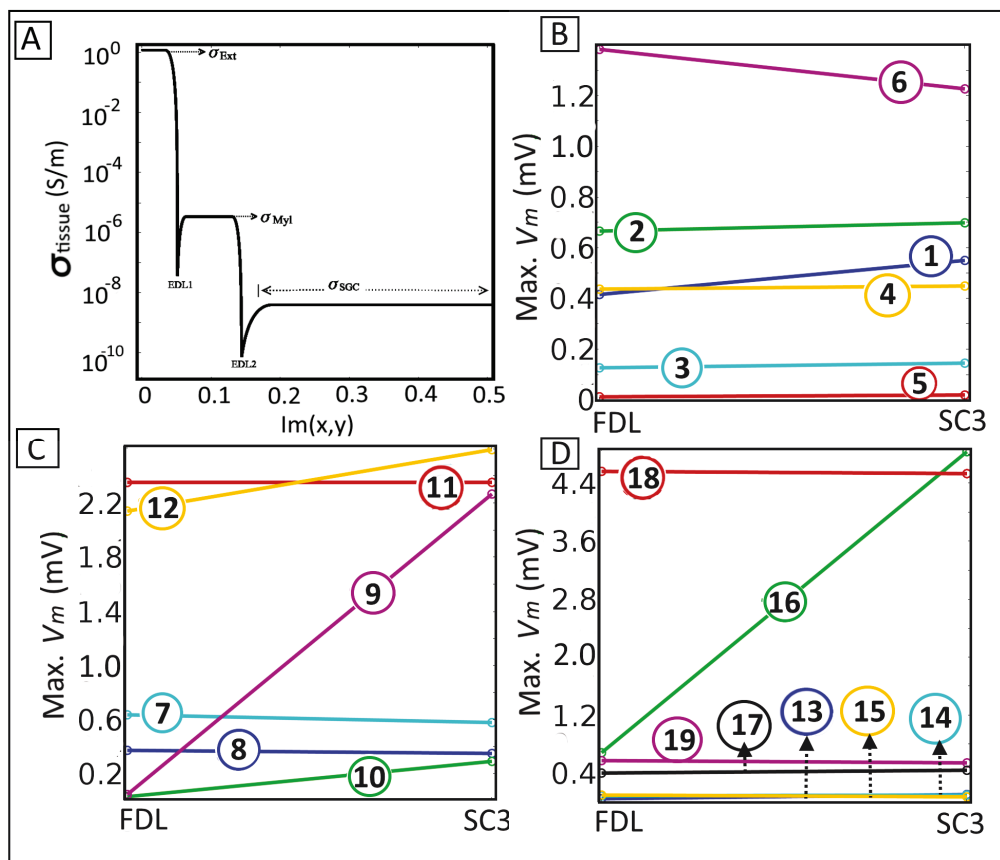


FIGURE 5.18: (A) Conductivity of the tissues expressed as a continuous function of the pixel data of the input image. The steep dip at the interface of the extracellular medium and the myeline tissues (EDL1), and at the interface of the myeline tissues and the SGC layer (EDL2) indicates an assumed electric double layer. (B)–(D) Maximal transmembrane potential induced ( $\text{Max. } V_m$ ) on the indicated SGNs (cell numbers are marked inside the circles on the curves) in the presence of assumed electric double layer in the continues function (FDL) and in Scenario3 (SC3). Notably, the variation in maximal  $V_m$  of SGNs in both cases indicates that the induced  $V_m$  could be different in other modeling scenarios which fall between FDL and SC3.

In the context of above assumption, an analytical expression to calculate the potential distribution in an inhomogeneous medium was given by Plonsey

and Heppner in [77]. The scalar potential ( $\Phi$ ) distribution in a piecewise inhomogeneous medium was obtained by solving the Helmholtz equation

$$\nabla^2\Phi + k^2\Phi = \frac{\nabla \cdot \mathbf{J}_s}{j\omega\epsilon_c} = \frac{-\rho}{\sigma + j\omega\epsilon} \quad (5.4)$$

where

$$k^2 = -j\omega\mu\sigma(1 + j\omega\epsilon/\sigma)$$

If each constituent sub-region is homogeneous with constant conductivity ( $\sigma$ ) and permittivity ( $\epsilon$ ), then the solution of equation (5.4) at field point  $p$  that satisfies the conditions for quasistatic approximation will be,

$$\Phi(p) = \frac{1}{4\pi} \int_{V'} \frac{\rho'}{\sigma \mathbf{R}} dV' - \frac{1}{4\pi} \sum_i \int_{S_i} \frac{\mathbf{E}_{n1} - \mathbf{E}_{n2}}{\mathbf{R}} dS_i, \quad (5.5)$$

where  $S_i$  is the surface component which separates region 1 and region 2. The second term in equation (5.5) indicates the secondary equivalent sources at the phase boundaries.

This implies that the assumption of a homogeneous medium in the RC would not capture the essential bioelectric phenomena such as the formation of secondary sources which would profoundly affect the stimulation profile of the SGNs. As a result, any *in silico* model describing the electric field distribution in the RC in the presence of a homogeneous medium would not replicate or justify the stochastic and dynamic firing behavior of the SGNs. For example, such model could not predict the mismatch between the surviving SGNs and the hearing quality in terms of word recognition reported in [214, 215, 216].

The spatial heterogeneity of the myelinated central axons could result in an asymmetric distribution of the nodes of Ranvier in the basal end of the cochlea. The length of the myelinated sheath would be around 400  $\mu\text{m}$  [65] for the central axons, it can be speculated that very few nodes would come under the influence of the stimulation. However, at the apical end, the RC tend to be one turn shorter than the total cochlea, and a dense population of the nodes could be expected. In this case, the presence of nodes would significantly alter the stimulation profile of apical SGNs.

## 5.7 Summary

The assumption of a homogeneous medium in the RC is prevalent in the existing *in silico* models of the cochlea. However, the RC contains various heterogeneously distributed tissues around the SGNs. As a result, the electric field distribution in the RC would differ significantly from that in the case of a homogeneous medium in the RC. The irregular SGCs layer around the SGNs profoundly affects the induced  $V_m$  of the SGNs. The gap junctions in the

## 5.7. Summary

---

SGC layer also play a prominent role in the stimulation of SGNs. Along with the SGCs layer, the mass of heterogeneously distributed myelinated central axons and other tissues in the RC significantly alter the stimulation profile of the SGNs. Further, any variation in the tissue density in the RC could asymmetrically affect the induced  $V_m$  of the SGNs. Notably, the dielectric properties of the tissues also play an essential role in the modeling. This study suggests that in the presence of a heterogeneous medium in the RC, the cell morphology and the SGN-electrode distance would not remarkably affect the stimulation of the SGNs. Instead, the degree of heterogeneity around the SGNs determines the stimulation probability of the SGNs.



## Chapter 6

# Conclusion

Persistent efforts of various *in vivo*, *in vitro*, and *in silico* studies have been improving the functionality of the CIs. Especially, *in silico* models have been efficiently harvesting the data from experimental studies and simulating the complex bioelectric scenarios related to the electric stimulation of the auditory nerve. The availability of overwhelming computational power and robust numerical methods is facilitating the inclusion of intricate biophysical parameters in the modeling. For instance, an automatic patient-specific cochlear modeling work flow with numerous realistic features has been proposed and tested for its clinical relevance in [217, 158, 218]. However, almost all cochlear models have considered the macro anatomy of the cochlea embedded with overly simplified auditory nerve fibers [50]. As a consequence, the outcome of various state-of-the-art *in silico* models of the cochlea are not different from one another and could not satisfactorily match the *in vivo* observations [139].

Moderate simplifications and justified assumptions are prerequisites to model a bioelectric phenomenon. However, it is apparent from the existing *in silico* models of the cochlea that a few assumptions and simplifications have been adapted without justification and proper explanation. The validity of three such model assumptions and simplifications has been studied in this thesis.

Firstly, the random spatial arrangement of SGNs and neuronal clusters in the RC which are evident from morphological studies of the temporal bone have not been considered in the existing *in silico* models. Instead, many state-of-the-art *in silico* models have used linearly aligned nerve fibers based on the compartment model [65] or the generalized Schwarz–Eikhof–Frijns (gSEF) model [60, 219]. In such auditory nerve fiber models, the AF has attained the maximal value on the AIS. Hence, it has been concluded that the probability of signal initiation is higher at the AIS of the spiral ganglion neuronal body. However, the AF is prone to the disproportionate geometric irregularities [220, 221] which are intrinsic in the compartmental nerve fiber model or gSEF model. Nevertheless, a few models [63, 222] implemented realistic nerve fiber trajectories in the RC and expressed the spatial selectivity of electric stimulation in terms of excitation density of the nerve fibers. Since the AF does not account for the presence of nerve fibers in the electric field, a few theoretical studies [92, 87] suggested the sub-threshold membrane potential approach to predict the neural excitation.

In this context, a two-dimensional finite element model containing the stimulating electrodes in the scala tympani and SGNs in the RC has been considered for the simulation. In case of a symmetrical arrangement of the SGNs in the RC filled with a homogeneous extracellular medium, both the AF and the sub-threshold potential approach have predicted similar signal initiation sites *viz.* peripheral axonal initial segments. However, in the presence of randomly oriented SGNs in the RC, the AF predicted the probability of signal initiation on the AIS irrespective of the SGNs orientation. On the contrary, the maximal sub-threshold transmembrane potential was induced on different sites of the SGNs depending on the cell orientation with respect to the applied electric field. If a high concentration of voltage-dependent sodium and potassium ion channels on the AIS [94, 223] of a myelinated soma is considered, the signal initiation would always take place on the AIS which is consistent with the predictions of the AF. However, for randomly oriented SGNs in the human cochlea, above argument does not hold true. Since the concentration of the voltage-dependent sodium and potassium ion channels on the unmyelinated soma and AIS was found to be similar [95], the signal initiation would take place where the maximal transmembrane potential crosses the cell-specific threshold potential. This implies the signal initiation sites could vary with the orientation of the SGNs. In this case, even if the signal is initiated at the AIS, the hyperpolarized and depolarized regions on the cell soma would block the signal propagation [122]. Hence, the present study suggests that the signal initiation and propagation would also depend on the SGNs orientation along with various other physiological factors.

An increased number of cell clusters has been observed in the older people [131]. The utility of the SGNs clusters in the RC has not been understood well. It is also not known how the cell clusters respond against the electric field induced by the CI. In the present study, signal generation and propagation in the cell clusters is modeled using the FitzHugh-Nagumo nerve pulse equations. The simulation results suggest that a cell cluster in the RC behaves like a single giant cell in response to the applied electric field. Since the SGN cell soma is unmyelinated in humans, a delay in the signal propagation would take place [65]. This expected delay would cause a persistent noise when the signal propagates through a cell cluster. The present study suggest that the cell clusters are easily prone to the electric stimulation due to the effective cell size of the cluster. Hence, the persistence noise or tinnitus would be affected in the cochlear implant recipients [132, 224].

Secondly, the modiolus that separates the scala tympani and the RC is a highly porous and multi-layered bony wall. However, existing *in silico* studies assumed the modiolus as a non-porous bone. Further, the electric conductivity of the modiolus was considered to be equal to that of the temporal bone which has very low conductivity [135]. As a result, the existing *in silico* models have predicted the spreading of most of the applied current in the scala tympani. Hence, with this assumption, the simulation models would have underestimated the stimulation probability of the SGNs. In this context, in the present study, a three-dimensional parametric model of the cochlea has been

considered to model the modiolus porosity. Two innovative methods have been proposed to address the typical modeling issues while implementing the bone porosity in an *in silico* model.

In the first method, the modiolus porosity was modeled through the linear extrusion of the pixel data of the modiolus obtained by a SEM image. Through a set of constraints, respective electric conductivities of the bone and the pores which are filled with perilymph was mapped on the modiolus domain. The simulation results suggest that the induced transmembrane potential of the SGNs with the porous modiolus is around 300% higher than that with the non-porous modiolus. The obvious reason for this discrepancy would be the resultant effective conductivity of the porous modiolus which is fifteen times higher than the assumed conductivity of the non-porous bone. A systematic study to estimate the impact of gradual increment of the modiolus porosity revealed that within the physiological range of the porosity (between 20% and 60%), the stimulation profile of the SGNs would change asymmetrically. This suggests that the functionality of a CI of a very young child would change with the aging. Further, the implementation of the effective conductivity obtained by the volume fraction of the pores would overestimate the stimulation probability of the SGNs. Further, the effective conductivity approach would not address the effect of local porosity on the stimulation profile of the SGNs.

In the second method, a set of reaction-diffusion equations is proposed to model the modiolus of desired global porosity with different local pore distribution. This method is useful for modeling a patient-specific cochlea. The proposed equation based method is applicable on any computer aided cochlear model. The simulation results of this method suggest that the local porosity would also affect the stimulation of the SGNs. This also suggests that any change in the local porosity induced by cochlear pathology or physical damage caused by the CI electrode would affect the hearing performance. Therefore, a substantial difference in the performance of CI recipients in terms of pitch perception, comfortable stimulation levels, and implant performance [225] can be arguably linked to the indeterministic variation in the modiolus porosity of individuals. The present study stresses the importance of a prospective study to find out the relation between the stimulation levels and the modiolus porosity. Further, present simulation results would support the feasibility of endosteal cochlear electrodes for the auditory nerve stimulation.

To this end, the assumption of plane symmetry in the 2D model geometry and the implementation of isotropic material properties in simulations is not robust enough to replicate the realistic scenario. Nevertheless, this assumption has provided a qualitative estimation of the electric field distribution similar to that in the state-of-the-art *in silico* models which have assumed a homogeneous extracellular medium in the RC.

Throughout the stated cases in the present study, isotropic electric conductivity was considered for all tissues. Admittedly, the anisotropic conductivity of neuronal tissues does alter the electric field distribution. Moreover, the CIs

operate on low-frequency stimulation in which the anisotropic conductivity may play a prominent role. Hence, the implementation of isotropic electric conductivity is erroneous to model a realistic biological scenario. However, the capacitive effects of biological tissues would be of negligible magnitude [226, 227] in a low-frequency stimulation.

Further, the electric double layer at the interface of the electrode and the tympanic fluid as well as at the interface of neural components and the extracellular medium which could cause a charge imbalance in the system [77] was not modeled. Moreover, the endocochlear potentials in the tympanic chambers [228] are not considered in the study.

The most serious limitation in the above study is the implementation of the homogeneous extracellular medium in the RC. Since the RC is situated very near to the electrodes, the SGNs respond like biological cell suspensions in a homogeneous medium exposed to a uniform electric field. In this case, the cell morphology prominently affects the induced transmembrane potential there by the signal initiation. Hence, all contextual state-of-the-art *in silico* models have focused on how the SGN shape, size, and vicinity to the stimulating electrode affect the electric stimulation of the auditory nerve. In the same context, the present study has shown that the cell orientation and cell clustering also affect the induced transmembrane potential of SGNs. Further, the assumption of a homogeneous medium in the RC was utilized to single out the effect of modiolus porosity on the stimulation profile of the SGNs.

Thirdly, the extracellular medium in the RC contains not only SGNs but also a variety of other cells and tissues. Of those, the SGCs form a loose encapsulation layer around each SGN. Also, all other tissues such as myelinated central axons could affect the electric field distribution. However, all existing *in silico* models have assumed a homogeneous extracellular medium in the RC. Understandably, modeling the heterogeneous tissues in the RC is both cumbersome and implausible in terms of modeling capabilities and computational expenses. However, this would not justify the exclusion of the significant tissue mass from the modeling. To address the modeling issues, an immunohistochemical image of the Rosenthal's canal in which most of the tissues are stained with respective neural markers has been considered. The electric conductivity was mapped in the RC according to the pixel data of each delineated tissue. The realistic geometry of SGNs was restored with image segmentation. This method allowed the implementation of required tissues in the RC with unprecedented detail in a 2D finite element model. The simulation results suggest that the irregular encapsulation layer of the SGCs around each SGN act as a proxy membrane which could determine the excitation of that SGN. This implies any inflammation or injury to the SGC layer would severely affect the excitation of the SGNs. Further, the presence of all other myelinated tissues around the SGNs also profoundly affected the electric field distribution in the RC. The simulation results considering all tissues in the RC significantly contradicted the simulation results obtained by assuming a homogeneous medium in the RC. Importantly, the impact of SGN-electrode distance and SGN morphology on the induced transmembrane potential was



trivial compared to the effect of tissue heterogeneity. This implies that the electrode placement in the scala tympani more towards the modiolus through modiolus-hugging electrodes may not improve the auditory nerve stimulation. This also suggests that the successful stimulation of the SGNs depends on the degree of heterogeneity and the favorable orientation of SGNs but not on the total number of SGNs present in the RC.

In the modeling perspective, electric conductivity values assigned for the SGC layer also showed a significant effect on the induced transmembrane potential of the SGNs. Additionally, the implementation of anisotropic conductivity of the myelinated tissues has altered the electric field distribution in the RC. The simulation results show that the implementation of the anisotropic conductivity is sensitive towards the chosen coordinate system.

The present modeling study can be improved prospectively in a number of ways. The SGC layer around the SGNs was assumed as a passive layer with constant electric conductivity. However, the SGCs show a rich ion pumping activity in coordination with the soma [229]. Also, the SGCs contain various ion channels including sodium and potassium ion channels [230, 231]. The dynamic activity of the ion channels would not produce action potentials in the SGCs [232] but result in higher resting potentials than the cell soma. Hence, the active SGNs coupled with the dynamic ion channel of the SGCs in the Hodgkin-Huxley modeling framework would be the most comprehensive auditory nerve model. With such models, a more in-depth understanding can be achieved about the nerve-electrode interactions.

In the present study, heterogeneous tissues are modeled in a simplified two-dimensional cochlear model. However, the model can be extended to a three-dimensional model with a stock of immunohistochemical images of the RC using the proposed image-based method. Further, the implementation of the modiolus porosity in such three-dimensional model of the cochlea embedded with above mentioned comprehensive auditory nerve model would address some of the most challenging problems of the auditory nerve stimulation.

Since the inclusion of microstructures such as modiolus porosity and tissue heterogeneity in the cochlear model would yield contravening simulation results, all investigations performed through the existing state-of-the-art *in silico* modeling studies could be re-investigated. For example, with the inclusion of suggested microstructures, the induced transmembrane potential of SGNs can be investigated by monopolar and tripolar stimulation strategies. Especially, further simulations with monophasic and biphasic stimulating pulses could yield some more interesting results. An immediate logical extension of the present study would be investigating the quantitative effects of tissue heterogeneity and the modiolus porosity on the sub-threshold transmembrane potential of the SGNs. A possible way for such a study would be quantifying the pertaining uncertainties in the tissue density and spatial distribution, modiolus porosity and the dielectric properties of the tissues.

Prospectively, present study could serve as an initial modeling framework for ongoing research related to gene therapy to repair the cochlear pathology and

drug-induced re-sprouting of auditory fibers to cure profound deafness. Since the tissue density in the RC has a profound effect on the stimulation profile of the SGNs, the combination of cochlear implants and stem cell transplantation would serve as an advanced clinical intervention to cure profound deafness.

As rightly pointed out in [233], CI research has been facing the challenge of finding the underlying factors for unusual variability in CI performance across children and adults. It is also apparent that a reliable method that can be clinically used as a preimplant predictor for CI functionality is not yet available. The anticipation towards finding as many influencing factors as possible would be the only way to overcome such challenges. To this end, present *in silico* study explored three major factors which potentially contribute some valuable insights to hearing research.

“The truth will always fall on deaf ears!”

---

*Anthony T.Hincks*

# Bibliography

- [1] WHO. *Deafness and hearing loss*. 2013.
- [2] Michael F Opitz and Matthew D Zbaracki. "Listen Hear!: The Economic Impact and Cost of Hearing Loss in Australia". In: *Access Econ.* February (2006), pp. 8–91.
- [3] Andrej Kral and Gerard M O 'Donoghue. "Profound Deafness in Childhood". In: *N Engl J Med* 363 (2010), pp. 1438–50.
- [4] Walter E Nance. "The genetics of deafness". In: *Ment. Retard. Dev. Disabil. Res. Rev.* 9.2 (2003), pp. 109–119.
- [5] R Hinojosa and J R Lindsay. "Profound deafness. Associated sensory and neural degeneration". In: *Arch. Otolaryngol. (Chicago, Ill.* 106.4 (1980), pp. 193–209.
- [6] Raäl Hinojosa and Mitchell Marion. "Histopathology of Profound Sensorineural Deafness". In: *Ann. N. Y. Acad. Sci.* 405.1 (1983), pp. 459–484.
- [7] Marloes Sparreboom et al. "The effectiveness of bilateral cochlear implants for severe-to-profound deafness in children: a systematic review." In: *Otol. Neurotol.* 31.7 (2010), pp. 1062–1071.
- [8] Olivier Macherey and Robert P. Carlyon. "Cochlear implants". In: *Curr. Biol.* 24.18 (2014), R878–R884.
- [9] Jelmer van Schoonhoven et al. "The Effectiveness of Bilateral Cochlear Implants for Severe-to-Profound Deafness in Adults : A Systematic Review". In: *Otol. Neurotol.* 34.2 (2013), pp. 190–198.
- [10] Robert Yawn et al. "Cochlear implantation: a biomechanical prosthesis for hearing loss." In: *F1000Prime Rep.* 7.April (2015), p. 45.
- [11] Gerard O'Donoghue. "Cochlear implants—science, serendipity, and success." In: *N. Engl. J. Med.* 369.13 (2013), pp. 1190–3.
- [12] Joseph P. Roche and Marlan R. Hansen. *On the Horizon: Cochlear Implant Technology*. 2015. arXiv: 15334406.

- [13] Jace Wolfe and Erin C Schafer. *Programming cochlear implants*. 2015. ISBN: 9781597565523\|r159756552.
- [14] Blake S Wilson et al. "Cochlear implants: Some likely next steps". In: *Annu. Rev. Biomed. Eng* 5 (2003), pp. 207–49.
- [15] Son-A Chang et al. "Performance over time on adults with simultaneous bilateral cochlear implants." In: *J. Am. Acad. Audiol.* 21.1 (2010), pp. 35–43. arXiv: NIHMS150003.
- [16] Jan Maurer, Nicolaos Marangos, and E. Ziegler. "Reliability of cochlear implants". In: *Otolaryngol. - Head Neck Surg.* 132.5 (2005), pp. 746–750.
- [17] Kate E. Gfeller et al. "Music perception with cochlear implants and residual hearing". In: *Audiol. Neurotol.* Vol. 11. SUPPL. 1. 2006, pp. 12–15. ISBN: 1420-3030 (Print)\|r1420-3030 (Linking).
- [18] Ray Meddis and Enrique A. Lopez-Poveda. "Auditory Periphery: From Pinna to Auditory Nerve". In: *Comput. Model. Audit. Syst.* 2010, pp. 7–38. ISBN: 978-1-4419-5934-8. arXiv: arXiv:1011.1669v3.
- [19] Tania Hanekom and Johan J Hanekom. "Three-dimensional models of cochlear implants: A review of their development and how they could support management and maintenance of cochlear implant performance". In: *Netw. Comput. Neural Syst.* 27.2-3 (2016), pp. 67–106.
- [20] Vinamra Agrawal and Carrie Newbold. "Computer modelling of the cochlea and the cochlear implant: A review". In: *Cochlear Implants Int.* 13.2 (2012), pp. 113–123.
- [21] Jennifer K Bizley and Yale E Cohen. "The what, where and how of auditory-object perception". In: *Nat Rev Neurosci* 14.10 (2013), pp. 693–707. arXiv: NIHMS150003.
- [22] Neal Anthwal and Hannah Thompson. "The development of the mammalian outer and middle ear". In: *J. Anat.* 228.2 (2016), pp. 217–232.
- [23] Mohit Kumar et al. "Stochastic fuzzy modeling for ear imaging based child identification". In: *IEEE Trans. Syst. Man, Cybern. Syst.* 46.9 (2016), pp. 1265–1278.
- [24] Matthew J Mason. "Structure and function of the mammalian middle ear. II: Inferring function from structure". In: *J. Anat.* 228.2 (2016), pp. 300–312.

- [25] Eric G Ekdale. "Form and function of the mammalian inner ear". In: *J. Anat.* 228.2 (2016), pp. 324–337.
- [26] Helge Rask-Andersen et al. "Human cochlea: anatomical characteristics and their relevance for cochlear implantation." In: *Anat. Rec. (Hoboken)*. 295.11 (2012), pp. 1791–811.
- [27] Elsa Erixon et al. "Variational anatomy of the human cochlea : Implications for cochlear implantation". In: *Otol. Neurotol.* 30 (2008), pp. 14–22.
- [28] Ersin Avci et al. "Variations in microanatomy of the human cochlea". In: *J. Comp. Neurol.* 522.14 (2014), pp. 3245–3261.
- [29] Luis Robles and Mario A Ruggero. "Mechanics of the mammalian cochlea." In: *Physiol. Rev.* 81.3 (2001), pp. 1305–52. arXiv: NIHMS150003.
- [30] Mario A Ruggero. "Responses to sound of the basilar membrane of the mammalian cochlea". In: *Curr. Opin. Neurobiol.* 2.4 (1992), pp. 449–456.
- [31] Georg von Békésy. "Experiments in hearing". In: *J. Acoust. Soc. Am.* 88.6 (1960), p. 2905.
- [32] Donald D Greenwood. "Critical bandwidth and the frequency coordinates of the basilar membrane". In: *J. Acoust. Soc. Am.* 33.10 (1961), pp. 1344–1356.
- [33] Anders Fridberger et al. "Organ of corti potentials and the motion of the basilar membrane". In: *J Neurosci* 24.45 (2004), pp. 10057–10063.
- [34] Werner Hemmert, Hans P Zenner, and Anthony W Gummer. "Three-dimensional motion of the organ of Corti." In: *Biophys. J.* 78.5 (2000), pp. 2285–97.
- [35] Geoffrey A. Manley et al. "Understanding the Cochlea". In: *Understanding the Cochlea*. Springer International Publishing, 2017. Chap. 4, pp. XVIII, 351. ISBN: 978-3-319-52071-1.
- [36] Geoffrey A. Manley et al. "Understanding the Cochlea". In: *Understanding the Cochlea*. Springer International Publishing, 2017. Chap. 6, pp. XVIII, 351. ISBN: 978-3-319-52071-1.
- [37] Geoffrey A. Manley et al. "Understanding the Cochlea". In: *Understanding the Cochlea*. Springer International Publishing, 2017. Chap. 7, pp. XVIII, 351. ISBN: 978-3-319-52071-1.

- [38] WHO Media centre. *WHO | Deafness and hearing loss*. 2014.
- [39] Samuel R Atcherson et al. "Hearing loss: Hearing augmentation." In: *FP Essent*. 434 (2015), pp. 18–23.
- [40] Justin K Chau, John J W Cho, and Dieter K Fritz. "Evidence-based practice, management of adult sensorineural hearing loss". In: *Otolaryngol. Clin. North Am*. 45.5 (2012), pp. 941–958.
- [41] Sara Euteneuer, Stefan Hansen, and Allen F Ryan. "The role of the spiral ganglion neurons in cochlear implants. Today and in future regenerative inner ear treatment". In: *HNO* 56.4 (2008), pp. 457–60.
- [42] Ariel Moctezuma and Jane Tu. "An overview of cochlear implant systems". In: *BIOE 414 Univ. Ollinois* (2011), pp. 1–20.
- [43] Ziyang Zhu et al. "Cochlear-implant spatial selectivity with monopolar, bipolar and tripolar stimulation." In: *Hear. Res*. 283.1-2 (2012), pp. 45–58.
- [44] Slavomir Biedron et al. "The internal dimensions of the cochlear scalae with special reference to cochlear electrode insertion trauma." In: *Otol. Neurotol*. 31.5 (2010), pp. 731–7.
- [45] Roxanne M Edge et al. "Morphology of the unfixed cochlea". In: *Hear. Res*. 124 (1998), pp. 1–16.
- [46] Guangjian Ni et al. "Modelling cochlear mechanics". In: *Biomed Res. Int*. 2014 (2014), 42 pages.
- [47] Emery Mayon Ku. "Modelling the human cochlea." In: *J. Acoust. Soc. Am*. 126.6 (2009), p. 3373.
- [48] Ronald J Thomas Jr. "A model for cochlear implant electrode insertion and force evaluation: results with a new electrode design and insertion technique". In: *Laryngoscope* 115.8 (2005), pp. 1325–1339.
- [49] Manuela Nowotny and Anthony W Gummer. "Vibration responses of the organ of Corti and the tectorial membrane to electrical stimulation". In: *J. Acoust. Soc. Am*. 130.6 (2011), p. 3852.
- [50] Vinamra Agrawal and Carrie Newbold. "Computer modelling of the cochlea and the cochlear implant: a review." In: *Cochlear Implants Int*. 13.2 (2012), pp. 113–23.

- [51] Dimitrios Kikidis and Athanasios Bibas. "A clinically oriented introduction and review on finite element models of the human cochlea". In: *Biomed Res. Int.* 2014. Article ID 975070 (2014), pp. 1–8.
- [52] Georg von Békésy. "The coarse pattern of the electrical resistance in the cochlea of the guinea pig (electroanatomy of the cochlea)". In: *J. Acoust. Soc. Am.* 23 (1951), p. 18.
- [53] Johnstone J R and Pugsley I D. "Membrane resistance in endolymphatic walls of the first turn of the guinea-pig cochlea". In: *J. Acoust. Soc. Am.* 402. August (1966), pp. 1398–1404.
- [54] David Strelhoff. "A computer simulation of the generation and distribution of cochlear potentials". In: *J. Acoust. Soc. Am.* 54.3 (1973), p. 620.
- [55] Michael F Suesserman and Francis A Spelman. "Lumped-Parameter Model for In Vivo Cochlear Stimulation". In: *IEEE Trans. Biomed. Eng.* 40.3 (1993), pp. 237–245.
- [56] Andrej Kral et al. "Spatial resolution of cochlear implants: The electrical field and excitation of auditory afferents". In: *Hear. Res.* 121.1-2 (1998), pp. 11–28.
- [57] Filip J Vanpoucke, Andrzej J Zarowski, and Stefaan A Peeters. "Identification of the impedance model of an implanted cochlear prosthesis from intracochlear potential measurements". In: *IEEE Trans. Biomed. Eng.* 51.12 (2004), pp. 2174–2183.
- [58] Gary Girzon. "Investigation of current flow in the inner ear during electrical stimulation of intracochlear electrodes". Master thesis. Department of Electrical Engineering and Computer Science, Massachusetts Institute of Technology, 1987.
- [59] Charles C Finley, Blake S Wilson, and Mark W White. "Models of Neural Responsiveness to Electrical Stimulation". In: *Cochlear Implant. Model. Electr. Stimul. Ear.* Ed. by Josef M Miller and Francis A Spelman. New York, NY: Springer New York, 1990, pp. 55–96. ISBN: 978-1-4612-3256-8.
- [60] Johan H M Frijns, S L de Snoo, and Ruurd Schoonhoven. "Potential distributions and neural excitation patterns in a rotationally symmetric model of the electrically stimulated cochlea". In: *Hear. Res.* 87.1-2 (1995), pp. 170–186.
- [61] Johan H M Frijns, Jeroen J Briaire, and Ruurd Schoonhoven. "Integrated use of volume conduction and neural models to simulate the

- response to cochlear implants". In: *Simul. Pract. Theory* 8.1-2 (2000), pp. 75–97.
- [62] Jeroen J Briaire and Johan H M Frijns. "Field patterns in a 3D tapered spiral model of the electrically stimulated cochlea". In: *Hear. Res.* 148.1-2 (2000), pp. 18–30.
- [63] Randy K Kalkman et al. "Place pitch versus electrode location in a realistic computational model of the implanted human cochlea". In: *Hear. Res.* 315 (2014), pp. 10–24.
- [64] Tania Hanekom. "Three-dimensional spiraling finite element model of the electrically stimulated cochlea." In: *Ear Hear.* 22.4 (2001), pp. 300–315.
- [65] Frank Rattay, Petra Lutter, and Heidi Felix. "A model of the electrically excited human cochlear neuronI. Contribution of neural substructures to the generation and propagation of spikes". In: *Hear. Res.* 153.1-2 (2001), pp. 43–63.
- [66] Frank Rattay, Richardson Naves Leao, and Heidi Felix. "A model of the electrically excited human cochlear neuron. II. Influence of the three-dimensional cochlear structure on neural excitability". In: *Hear. Res.* 153.1-2 (2001), pp. 64–79.
- [67] Frank Rattay, L P Paredes, and R N Leao. "Strength-duration relationship for intra- versus extracellular stimulation with microelectrodes." In: *Neuroscience* 214 (2012), pp. 1–13.
- [68] Frank Rattay. "Analysis of models for external stimulation of axons". In: *IEEE Trans. Biomed. Eng.* BME-33.10 (1986), pp. 974–977.
- [69] J Patrick Reilly and Alan M Diamant. *Electrostimulation : theory, applications, and computational model*. English. Boston: Artech House, 2011. ISBN: 9781608071098 160807109X.
- [70] Charles T M Choi, Wei-dian Lai, and Yu-bin Chen. "Optimization of cochlear implant electrode array using genetic algorithms and computational neuroscience models". In: *Ieee Trans. Magn.* 40.2 (2004), pp. 639–642.
- [71] Wei Dian Lai and C. T M Choi. "Incorporating the electrode-tissue interface to cochlear implant models". In: *IEEE Trans. Magn.* Vol. 43. 4. 2007, pp. 1721–1724. ISBN: 1424403200.



- [72] Darren M Whiten. “Electro-anatomical models of the cochlear implant”. PhD thesis. Harvard University; MIT Division of Health Sciences and Technology., 2007.
- [73] Rami Saba. “Cochlear implant modelling: stimulation and power consumption”. PhD thesis. University of Southampton, 2012.
- [74] Annkathrin Grünbaum. “Entwicklung eines detaillierten Modells der humanen Cochlea für numerische Studien von implantierten Elektroden”. Dissartation. University of Rostock, 2014, p. 107.
- [75] James C Maxwell. “A dynamical theory of the electromagnetic field”. In: *Philos. Trans. R. Soc. London* 155. January (1865), pp. 459–512.
- [76] Ursula van Rienen. *Numerical Methods In Computational Electrodynamics*. Springer, 2001. ISBN: 9783540676294.
- [77] Robert Plonsey and Dennis B Heppner. “Considerations of quasi-stationarity in electrophysiological systems”. In: *Bull. Math. Biophys.* 29.4 (1967), pp. 657–664.
- [78] Jacob Fish and Ted Belytschko. *A First Course in Finite Elements*. 2007, pp. 1–319. ISBN: 9780470035801. arXiv: arXiv:1011.1669v3.
- [79] Oleck C Zienkiewicz et al. *The finite element method*. 2005, p. 1863. ISBN: 0750663219;0750663200;0750663227.
- [80] Matthew N O Sadiku, A Z Makki, and L C Agba. “A further introduction to finite element analysis of electromagnetic problems”. In: *IEEE Trans. Educ.* 34.4 (1991), pp. 322–329.
- [81] Matthew N O Sadiku. *Numerical Techniques in Electromagnetics*. 1992, pp. xviii + 690. ISBN: 0849342325.
- [82] Alan L Hodgkin and Andrew F Huxley. “A quantitative description of membrane current and its application to conduction and excitation in nerve”. In: *Bull. Math. Biol.* 52.1-2 (1990), pp. 25–71. arXiv: NIHMS150003.
- [83] Thomas Heimburg and Andrew D Jackson. “On soliton propagation in biomembranes and nerves.” In: *Proc. Natl. Acad. Sci. U. S. A.* 102.28 (2005), pp. 9790–9795.
- [84] Peter J Basser and Bradley J Roth. “New Currents in Electrical Stimulation of Excitable Tissues1”. In: *Annu. Rev. Biomed. Eng.* 2.1 (2000), pp. 377–397.

- [85] Denis Noble and RB Stein. "The threshold conditions for initiation of action potentials by excitable cells". In: *J. Physiol.* 187.1 (1966), pp. 129–162.
- [86] Lawrence T Cohen. "Practical model description of peripheral neural excitation in cochlear implant recipients: 4. Model development at low pulse rates: General model and application to individuals". In: *Hear. Res.* 248.1-2 (2009), pp. 15–30.
- [87] Robert Plonsey and Roger C Barr. "Electric field stimulation of excitable tissue". In: *IEEE Eng. Med. Biol. Mag.* 17.5 (1998), pp. 130–137.
- [88] Richard FitzHugh. "Mathematical models of threshold phenomena in the nerve membrane". In: *Bull. Math. Biophys.* 17.4 (1955), pp. 257–278.
- [89] Lars D Mosgaard and Thomas Heimburg. "Lipid ion channels and the role of proteins". In: *Acc. Chem. Res.* 46.12 (2013), pp. 2966–2976. arXiv: arXiv:1307.3045v1.
- [90] Robert Plonsey and Roger C Barr. *Bioelectricity: A quantitative approach*. 2007, pp. 1–528. ISBN: 9780387488646. arXiv: 9809069v1 [arXiv:gr-qc].
- [91] Frank Rattay. "Ways to approximate current-distance relations for electrically stimulated fibers". In: *J. Theor. Biol.* 125.3 (1987), pp. 339–349.
- [92] K W Altman and Robert Plonsey. "Analysis of excitable cell activation: Relative effects of external electrical stimuli". In: *Med. Biol. Eng. Comput.* 28.6 (1990), pp. 574–580.
- [93] Wei Liu et al. "The pre- and post somatic segments of the human type 1 spiral ganglion neurons-structural and functional considerations related to cochlear implantation". In: *J. Neurosci.* 284 (2015), pp. 470–482.
- [94] Waheeda A Hossain et al. "Where is the spike generator of the cochlear nerve? Voltage-gated sodium channels in the mouse cochlea." In: *J. Neurosci.* 25.29 (2005), pp. 6857–68.
- [95] Maarten H P Kole et al. "Action potential generation requires a high sodium channel density in the axon initial segment." In: *Nat. Neurosci.* 11.2 (2008), pp. 178–86.
- [96] Lianne A Cartee. "Spiral ganglion cell site of excitation II: numerical model analysis." In: *Hear. Res.* 215.1-2 (2006), pp. 22–30.

- [97] Eric Javel and Robert K. Shepherd. "Electrical stimulation of the auditory nerve. III. Response initiation sites and temporal fine structure". In: *Hear. Res.* 140.1-2 (2000), pp. 45–76.
- [98] Olivier Goury et al. "Numerical simulation of cochlear-implant surgery: Towards patient-specific planning". In: *Lect. Notes Comput. Sci. (including Subser. Lect. Notes Artif. Intell. Lect. Notes Bioinformatics)*. Vol. 9900 LNCS. 2016, pp. 500–507. ISBN: 9783319467191.
- [99] Michael J O'Leary et al. "Electrode insertion trauma in cochlear implantation". In: *Ann. Otol. Rhinol. Laryngol.* 100.9 (1991), pp. 695–699.
- [100] Stephen J Rebscher et al. "Considerations for design of future cochlear implant electrode arrays: electrode array stiffness, size, and depth of insertion." In: *J. Rehabil. Res. Dev.* 45.5 (2008), pp. 731–747. arXiv: NIHMS150003.
- [101] Paul Wong et al. "Development and Validation of a High-Fidelity Finite-Element Model of Monopolar Stimulation in the Implanted Guinea Pig Cochlea". In: *IEEE Trans. Biomed. Eng.* 63.1 (2016), pp. 188–198.
- [102] Alan G Micco and Claus-Peter Richter. "Electrical resistivity measurements in the mammalian cochlea after neural degeneration." In: *Laryngoscope* 116.8 (2006), pp. 1334–1341.
- [103] Igor V Timoshkin et al. "Forces acting on biological cells in external electrical fields". In: *Annu. Rep. - Conf. Electr. Insul. Dielectr. Phenomena, CEIDP*. 2006, pp. 676–679. ISBN: 1424405475.
- [104] Davorka Sel et al. "Sequential finite element model of tissue electroporation." In: *IEEE Trans. Biomed. Eng.* 52.5 (2005), pp. 816–27.
- [105] Blaz Valic et al. "Effect of electric field induced transmembrane potential on spheroidal cells: theory and experiment." In: *Eur. Biophys. J.* 32.6 (2003), pp. 519–28.
- [106] Jonghwan Lee, David a Boas, and Sung June Kim. "Multiphysics neuron model for cellular volume dynamics." In: *IEEE Trans. Biomed. Eng.* 58.10 (2011), pp. 3000–3.
- [107] Jan Gimsa and Derk Wachner. "Analytical description of the transmembrane voltage induced on arbitrarily oriented ellipsoidal and cylindrical cells." In: *Biophys. J.* 81.4 (2001), pp. 1888–96.

- 
- [108] Nicolas Gerber et al. "A multiscale imaging and modelling dataset of the human inner ear." In: *Sci. data* 4 (2017), p. 170132.
- [109] Constantino Grosse and Herman P. Schwan. "Cellular membrane potentials induced by alternating fields". In: *Biophys. J.* 63.6 (1992), pp. 1632–1642.
- [110] Feriel Sihem Hamdi et al. "Study of the transmembrane potential distribution of cell pairs in a microfluidic device using polymer obstacles to initiate electrofusion". In: *Eur. Phys. J. - Appl. Phys.* 62.01 (2013), pp. 11202–11212.
- [111] Alan Gerard Micco and Claus-Peter Richter. "Tissue resistivities determine the current flow in the cochlea." In: *Curr. Opin. Otolaryngol. Head Neck Surg.* 14.5 (2006), pp. 352–355.
- [112] Jens Haueisen et al. "Influence of tissue resistivities on neuromagnetic fields and electric potentials studied with a finite element model of the head". In: *IEEE Trans. Biomed. Eng.* 44.8 (1997), pp. 727–735.
- [113] Charlotte Daniels and Boris Rubinsky. "Electrical Field and Temperature Model of Nonthermal Irreversible Electroporation in Heterogeneous Tissues". In: *J Biomech Eng* 131.7 (2009), p. 71006.
- [114] M J Dennis and H M Gerschenfeld. "Some physiological properties of identified mammalian neuroglial cells." In: *J. Physiol.* 203.1 (1969), pp. 211–22.
- [115] Patrick R Amestoy, I. Duff, and J.-Y. L'Excellent. "Multifrontal parallel distributed symmetric and unsymmetric solvers". In: *Comput. Methods Appl. Mech. Eng.* 184.2-4 (2000), pp. 501–520.
- [116] Wenqin Hu et al. "Distinct contributions of Nav1.6 and Nav1.2 in action potential initiation and backpropagation". In: *Nat. Neurosci.* 12.8 (2009), pp. 996–1002.
- [117] Kevin J Bender, Christopher P Ford, and Laurence O Trussell. "Dopaminergic Modulation of Axon Initial Segment Calcium Channels Regulates Action Potential Initiation". In: *Neuron* 68.3 (2010), pp. 500–511.
- [118] Frank Rattay et al. "Impact of morphometry, myelination and synaptic current strength on spike conduction in human and cat spiral ganglion neurons." In: *PLoS One* 8.11 (2013), e79256.

- [119] C. Schmidt-Hieber and J. Bischofberger. “Fast Sodium Channel Gating Supports Localized and Efficient Axonal Action Potential Initiation”. In: *J. Neurosci.* 30.30 (2010), pp. 10233–10242.
- [120] Sean A Freeman et al. “Mechanisms of sodium channel clustering and its influence on axonal impulse conduction”. In: *Cell. Mol. Life Sci.* 73.4 (2016), pp. 723–735.
- [121] Jonathan Platkiewicz and Romain Brette. “A threshold equation for action potential initiation”. In: *PLoS Comput. Biol.* 6.7 (2010), p. 25.
- [122] Takuya Sasaki, Norio Matsuki, and Yuji Ikegaya. “Action-Potential Modulation During Axonal Conduction”. In: *Science (80-. )*. 331.6017 (2011), pp. 599–601.
- [123] Niloy Bhadra and Kevin L Kilgore. “Direct current electrical conduction block of peripheral nerve”. In: *IEEE Trans Neural Syst Rehabil Eng* 12.3 (2004), pp. 313–324.
- [124] Thomas Potrusil et al. “Morphometric classification and spatial organization of spiral ganglion neurons in the human cochlea: Consequences for single fiber response to electrical stimulation”. In: *Neuroscience* 214 (2012), pp. 120–135.
- [125] Rudolf Glueckert et al. “The human spiral ganglion: New insights into ultrastructure, survival rate and implications for cochlear implants”. In: *Audiol. Neurotol.* 10.5 (2005), pp. 258–273.
- [126] Jin-Ichi Nagumo, S. Arimoto, and S. Yoshizawa. “An Active Pulse Transmission Line Simulating Nerve Axon\*”. In: *Proc. IRE* 50.10 (1962), pp. 2061–2070.
- [127] Richard FitzHugh. “Impulses and Physiological States in Theoretical Models of Nerve Membrane”. In: *Biophys. J.* 1.6 (1961), pp. 445–466.
- [128] Revathi Appali. “Modeling the Coupling of Action Potential and Electrodes”. Dissertation. University of Rostock, 2013.
- [129] James Keener and James Sneyd. *Mathematical Physiology I: Cellular Physiology*. Vol. 82. 4. 2013, p. 476. ISBN: 4420767936. arXiv: 1406.6401.
- [130] Mojca Pavlin, Natasa Pavselj, and Damijan Miklavcic. “Dependence of induced transmembrane potential on cell density, arrangement, and cell position inside a cell system.” In: *IEEE Trans. Biomed. Eng.* 49.6 (2002), pp. 605–12.

- 
- [131] Richard R Gacek. "Clustering is a feature of the spiral ganglion in the basal turn". In: *Orl* 74.1 (2012), pp. 22–27.
- [132] Andrea Kleine Punte, Olivier Meeus, and Paul Van De Heyning. "Cochlear implants and tinnitus". In: *Textb. Tinnitus*. 2011, pp. 619–624. ISBN: 9781607611448.
- [133] Babür Küçük et al. "Microstructures of the bony modiolus in the human cochlea: A scanning electron microscopic study". In: *Microscopy* 40.3 (1991), pp. 193–197.
- [134] Helge Rask-Andersen et al. "Perilymph/modiolar communication routes in the human cochlea." In: *Ear Hear*. 27.5 (2006), pp. 457–465.
- [135] Tiaan K Malherbe, Tania Hanekom, and Johan J Hanekom. "The effect of the resistive properties of bone on neural excitation and electric fields in cochlear implant models." In: *Hear. Res.* 327 (2015), pp. 126–35.
- [136] Joanna Sierpowska et al. "Interrelationships between electrical properties and microstructure of human trabecular bone". In: *Phys. Med. Biol.* 51.20 (2006), pp. 5289–5303.
- [137] Masataka Hakamada et al. "Influence of porosity and pore size on electrical resistivity of porous aluminum produced by spacer method". In: *Mater. Trans.* 48.1 (2007), pp. 32–36.
- [138] Karin Lundin, Fredrik Stillesjö, and Helge Rask-Andersen. "Experiences and results from cochlear implantation in patients with long duration of deafness". In: *Audiol Neurotol Extra* 4.March 2016 (2014), pp. 46–55.
- [139] Randy K Kalkman et al. "Stimulation strategies and electrode design in computational models of the electrically stimulated cochlea: An overview of existing literature". In: *Netw. Comput. Neural Syst.* 6536.May (2016), pp. 1–28.
- [140] Johan Helsing. "Bounds to the conductivity of some two-component composites". In: *J. Appl. Phys.* 73.3 (1993), pp. 1240–1245.
- [141] David Linton Johnson and N Sen Pabitra. "Dependence of the conductivity of a porous medium on electrolyte conductivity". In: *Phys. Rev. B* 37.7 (1988), pp. 3502–3510.
- [142] Cristian Ciobanu et al. "Numerical calculation of electrical conductivity of porous electroceramics". In: (1999), pp. 17–23.

- [143] Sophie Hautot and Pascal Tarits. "Effective electrical conductivity of 3-D heterogeneous porous media". In: *Geophys. Res. Lett.* 29.14 (2002), p. 14.
- [144] Elena Cherkaev and Carlos Bonifasi-Lista. "Characterization of structure and properties of bone by spectral measure method". In: *J. Biomech.* 44.2 (2011), pp. 345–351.
- [145] Bashir M Suleiman. "Effective thermal conduction in composite materials". In: *Appl. Phys. A* 99.1 (2010), pp. 223–228.
- [146] Salvatore Torquato. *Random Heterogeneous Materials - Microstructure and Macrostructure Properties*. Vol. 16. 2002, pp. 1–701. ISBN: 0-387-95167-9.
- [147] David B Pisoni et al. "Individual differences in effectiveness of cochlear implants in children who are prelingually deaf: New process measures of performance." In: *Volta Rev.* 101.3 (1999), pp. 111–164. arXiv: NIHMS150003.
- [148] Maria Stella Arantes do Amaral et al. "Cochlear implant revision surgeries in children". In: *Braz. J. Otorhinolaryngol.* (2018).
- [149] Edwin M Monsell. "The mechanism of hearing loss in Paget's disease of bone". In: *Laryngoscope* 114.4 (2004), pp. 598–606.
- [150] Alan M Turing. "The chemical basis of morphogenesis". In: *Philos. Trans. R. Soc. Lond. B. Biol. Sci.* 237.641 (1952), pp. 37–72.
- [151] Hans Meinhardt. "Pattern formation in biology: A comparison of models and experiments". In: *Reports Prog. Phys.* 55.6 (1992), pp. 797–849.
- [152] Basil Nicolaenko, Bruno Scheurer, and Roger Temam. "Some global dynamical properties of a class of pattern formation equations". In: *Commun. Partial Differ. Equations* 14.2 (1989), pp. 245–297.
- [153] Benoît Perthame. "Linear instability, Turing instability and pattern formation". In: *Parabol. Equations Biol.* 2015, pp. 117–143. ISBN: 978-3-7643-7841-7. arXiv: arXiv:1011.1669v3.
- [154] Dwight Barkley. "A model for fast computer simulation of waves in excitable media". In: *Phys. D Nonlinear Phenom.* 49.1 (1991), pp. 61–70.

- [155] Matthew Dowle, Rolf Martin Mantel, and Dwight Barkley. "Fast simulations of waves in three-dimensional excitable media". In: *Int. J. Bifurc. Chaos* 07.11 (1997), pp. 2529–2545.
- [156] Björn Sandstede and Arnd Scheel. "Absolute versus convective instability of spiral waves". In: *Phys. Rev. E - Stat. Physics, Plasmas, Fluids, Relat. Interdiscip. Top.* 62.6 (2000), pp. 7708–7714.
- [157] Markus Bär and Markus Eiswirth. "Turbulence due to spiral breakup in a continuous excitable medium". In: *Phys. Rev. E* 48.3 (1993).
- [158] Waldo Nogueira et al. "Validation of a cochlear implant patient-specific model of the voltage distribution in a clinical setting". In: *Front. Bioeng. Biotechnol.* 4 (2016).
- [159] Hans Wilhelm Pau et al. "An "endosteal electrode" for cochlear implantation in cases with residual hearing? Feasibility study: preliminary temporal bone experiments." In: *Otol. Neurotol.* 26.3 (2005), pp. 448–54.
- [160] Hans Wilhelm Pau et al. "Would an endosteal CI-electrode make sense? Comparison of the auditory nerve excitability from different stimulation sites using ESRT measurements and mathematical models". In: *Eur. Arch. Oto-Rhino-Laryngology* 271.6 (2014), pp. 1375–1381.
- [161] Kiran Kumar Sriperumbudur, Hans Wilhelm Pau, and Ursula Van Rienen. "Effect of tissue heterogeneity on the transmembrane potential of type-1 spiral ganglion neurons: A simulation study". In: *IEEE Trans. Biomed. Eng.* 65.3 (2018), pp. 658–668.
- [162] Bryony A Nayagam, Michael A Muniak, and David K Ryugo. "The spiral ganglion: Connecting the peripheral and central auditory systems". In: *Hear. Res.* 278.1-2 (2011), pp. 2–20.
- [163] Helge Rask-Andersen et al. "Nerve fibre interaction with large ganglion cells in the human spiral ganglion. A TEM study." In: *Auris. Nasus. Larynx* 24.1 (1997), pp. 1–11.
- [164] Heinrich Spoendlin and Annelies Schrott-Fischer. "Analysis of the human auditory nerve". In: *Hear. Res.* 43.1 (1989), pp. 25–38.
- [165] Pavel Dublin and Menachem Hanani. "Satellite glial cells in sensory ganglia: Their possible contribution to inflammatory pain". In: *Brain. Behav. Immun.* 21.5 (2007), pp. 592–598.



- [166] Pedro C Miranda, Mark Hallett, and Peter J Basser. "The electric field induced in the brain by magnetic stimulation: A 3-D finite-element analysis of the effect of tissue heterogeneity and anisotropy". In: *IEEE Trans. Biomed. Eng.* 50.9 (2003), pp. 1074–1085.
- [167] Pedro C Miranda et al. "Tissue heterogeneity as a mechanism for localized neural stimulation by applied electric fields." In: *Phys. Med. Biol.* 52.18 (2007), pp. 5603–5617.
- [168] Boris Rubinsky. "Electrical Field and Temperature Model of Non-thermal Irreversible Electroporation in Heterogeneous Tissues". In: *J. Biomech. Eng.* 131.7 (2009), p. 071006.
- [169] Oleg V Aslanidi et al. "Heterogeneous and anisotropic integrative model of pulmonary veins: computational study of arrhythmogenic substrate for atrial fibrillation." In: *Interface Focus* 3.2 (2013), p. 20120069.
- [170] Alexander Golberg et al. "Tissue heterogeneity in structure and conductivity contribute to cell survival during irreversible electroporation ablation by "electric field sinks"." In: *Sci. Rep.* 5 (2015), p. 8485.
- [171] Hans Rullgård et al. "Simulation of transmission electron microscope images of biological specimens". In: *J. Microsc.* 243.3 (2011), pp. 234–256.
- [172] Chunming Li, John C. Gore, and Christos Davatzikos. "Multiplicative intrinsic component optimization (MICO) for MRI bias field estimation and tissue segmentation". In: *Magn. Reson. Imaging* 32.7 (2014), pp. 913–923.
- [173] George G Somjen. "Electrophysiology of neuroglia." In: *Annu. Rev. Physiol.* 37.171 (1975), pp. 163–190.
- [174] G. G. Somjen, H. Kager, and W. J. Wadman. "Computer simulations of neuron-glia interactions mediated by ion flux". In: *J. Comput. Neurosci.* 25.2 (2008), pp. 349–365.
- [175] Eric W Lothman and George G Somjen. "Extracellular potassium activity, intracellular and extracellular potential responses in the spinal cord". In: *J Physiol* 252 (1975), pp. 115–136.
- [176] Michael Trachtenberg, Paul L Kornblith, and J Häuptli. "Biophysical properties of cultured human glial cells". In: *Brain Res.* 38 (1972), pp. 279–298.

- [177] Antonia Vernadakis and Albert Berni. "Changes in the resting membrane potentials of glial cells in culture". In: *Brain Res.* 57.1 (1973), pp. 223–228.
- [178] Soojin Kang et al. "Effects of electrode position on spatiotemporal auditory nerve fiber responses: A 3D computational model study". In: *Comput. Math. Methods Med.* 2015 (2015).
- [179] George B Wanna et al. "Assessment of electrode placement and audiological outcomes in bilateral cochlear implantation". In: *Otol. Neurotol.* 32.3 (2011), pp. 428–432. arXiv: NIHMS150003.
- [180] George B Wanna et al. "Impact of intrascalar electrode location, electrode type, and angular insertion depth on residual hearing in cochlear implant patients: Preliminary results". In: *Otol. Neurotol.* 36.8 (2015), pp. 1343–1348.
- [181] Ursula van Rienen et al. "Electro-quasistatic simulations in bio-systems engineering and medical engineering". In: *Adv. Radio Sci.* 3 (2005), pp. 39–49.
- [182] Hans W Pau et al. "Temporal bone investigations on landmarks for conventional or endosteal insertion of cochlear electrodes." In: *Acta Otolaryngol.* 127.9 (2007), pp. 920–6.
- [183] Noha Hassan et al. "Mapping membrane-potential perturbations of chromaffin cells exposed to electric fields". In: *IEEE Trans. Plasma Sci.* 30.4 I (2002), pp. 1516–1524.
- [184] Gorazd Pucihar et al. "Numerical determination of transmembrane voltage induced on irregularly shaped cells". In: *Ann. Biomed. Eng.* 34.4 (2006), pp. 642–652.
- [185] Wei Liu et al. "Possible role of gap junction intercellular channels and connexin 43 in satellite glial cells (SGCs) for preservation of human spiral ganglion neurons : A comparative study with clinical implications." In: *Cell Tissue Res.* 355.2 (2014), pp. 267–78.
- [186] Maurice Klee and Robert Plonsey. "Extracellular stimulation of a cell having a non-uniform membrane". In: *IEEE Trans. Biomed. Eng.* 21.6 (1974), pp. 452–460.
- [187] Robin L Davis and Robert A Crozier. "Dynamic firing properties of type I spiral ganglion neurons". In: *Cell Tissue Res.* 361.1 (2015), pp. 115–127.

- [188] Z L Mo and Robin L Davis. "Heterogeneous voltage dependence of inward rectifier currents in spiral ganglion neurons." In: *J. Neurophysiol.* 78.6 (1997), pp. 3019–27.
- [189] Lianne A Cartee et al. "Evaluation of a model of the cochlear neural membrane. I. Physiological measurement of membrane characteristics in response to intrameatal electrical stimulation". In: *Hear. Res.* 146.1-2 (2000), pp. 143–152.
- [190] Qing Liu and Robin L Davis. "Regional specification of threshold sensitivity and response time in CBA/CaJ mouse spiral ganglion neurons". In: *J. Neurophysiol.* 98.4 (2007), pp. 2215–2222.
- [191] Robert A Crozier and Robin L Davis. "Unmasking of spiral ganglion neuron firing dynamics by membrane potential and neurotrophin-3". In: *J Neurosci* 34.29 (2014), pp. 9688–9702.
- [192] Pavel S Cherkas et al. "The effects of axotomy on neurons and satellite glial cells in mouse trigeminal ganglion". In: *Pain* 110.1-2 (2004), pp. 290–298.
- [193] Elise C Fear and Maria A Stuchly. "Biological cells with gap junctions in low-frequency electric fields". In: *IEEE Trans. Biomed. Eng.* 45.7 (1998), pp. 856–866.
- [194] Woo Chul Jeong et al. "Evaluation of three-dimensional anisotropic head model for mapping realistic electromagnetic fields of brain tissues". In: *AIP Adv.* 5.8 (2015).
- [195] Christian Schmidt et al. "Influence of uncertainties in the material properties of brain tissue on the probabilistic volume of tissue activated". In: *IEEE Trans. Biomed. Eng.* 60.5 (2013), pp. 1378–1387.
- [196] Saurav Z K Sajib et al. "Experimental evaluation of electrical conductivity imaging of anisotropic brain tissues using a combination of diffusion tensor imaging and magnetic resonance electrical impedance tomography". In: *APL Mater.* 6.6 (2016).
- [197] Salvatore Torquato. "Theory of random heterogeneous materials". In: *Handb. Mater. Model.* 2005, pp. 1333–1357. ISBN: 978-1-4020-3287-5 978-1-4020-3286-8.
- [198] M J Peters, J G Stinstra, and M Hendriks. "Estimation of the electrical conductivity of human tissue". In: *Electromagnetics* 21.7-8 (2001), pp. 545–557.

- [199] Bjorn Sjodin. *Using Curvilinear Coordinates*:<https://www.comsol.de/blogs/using-curvilinear-coordinates/>. Tech. rep. 2013.
- [200] Nancy Bannach. *Defining Curvilinear Coordinates for Anisotropic Materials*: <https://www.comsol.com/blogs/defining-curvilinear-coordinates-anisotropic-materials/>. 2014. (Visited on 06/27/2018).
- [201] Lianne A Cartee, Charles A Miller, and Chris van den Honert. "Spiral ganglion cell site of excitation I: comparison of scala tympani and intrameatal electrode responses." In: *Hear. Res.* 215.1-2 (2006), pp. 10–21.
- [202] Joseph B Nadol. "Patterns of neural degeneration in the human cochlea and auditory nerve: Implications for cochlear implantation". In: *Otolaryngol. - Head Neck Surg.* 117.3 (1997), pp. 220–228.
- [203] Corinna E Zimmermann, Barbara J Burgess, and Joseph B Nadol. "Patterns of degeneration in the human cochlear nerve". In: *Hear. Res.* 90.1-2 (1995), pp. 192–201.
- [204] Bryan E Pfingst et al. "Importance of cochlear health for implant function". In: *Hear. Res.* 322 (2015), pp. 77–88.
- [205] Alison J Evans et al. "Promoting neurite outgrowth from spiral ganglion neuron explants using polypyrrole/BDNF-coated electrodes". In: *J. Biomed. Mater. Res. - Part A* 91.1 (2009), pp. 241–250.
- [206] Jenny L Goehring et al. "How well do cochlear implant intraoperative impedance measures predict postoperative electrode function?". In: *Otol. Neurotol.* 34.2 (2013), pp. 239–244. arXiv: NIHMS150003.
- [207] Marek Zadrozniak et al. "Impedance changes in cochlear implant users". In: *Otolaryngol. Pol. Polish Otolaryngol.* 65.3 (2010), pp. 214–217.
- [208] Rachel A Scheperle et al. "Delayed changes in auditory status in cochlear implant users with preserved acoustic hearing". In: *Hear. Res.* 350 (2017), pp. 45–57.
- [209] Christian Schmidt et al. "Impact of uncertain head tissue conductivity in the optimization of transcranial direct current stimulation for an auditory target". In: *J. Neural Eng.* 12.4 (2015). arXiv: 15334406.
- [210] Motomu Tanaka. "Physics of interactions at biological and biomaterial interfaces". In: *Curr. Opin. Colloid Interface Sci.* 18.5 (2013), pp. 432–439.

- [211] Leszek Herbowski and Henryk Gurgul. "The structure of the electric double layer of macromolecules suspended in human cerebrospinal fluid". In: *J. Neurol. Neurophysiol.* 02.1 (2011), pp. 2–4.
- [212] Andre S Dukhin. "Biospecific mechanism of double layer formation and peculiarities of cell electrophoresis". In: *Colloids Surfaces A Physicochem. Eng. Asp.* 73.C (1993), pp. 29–48.
- [213] Leszek Herbowski, Henryk Gurgul, and Waldemar Staron. "Experimental determination of the Stern layer thickness at the interface of the human arachnoid membrane and the cerebrospinal fluid". In: *Z. Med. Phys.* 19.3 (2009), pp. 189–192.
- [214] Mohammad Seyyedi and Joseph B Nadol. "Does residual spiral ganglion cell count predict performance in patients with bilateral multichannel cochlear implants?" In: *Otolaryngol. – Head Neck Surg.* 149.2 Suppl (2013), P97–P97.
- [215] Helen X Xu et al. "Multi-channel cochlear implant histopathology: Are fewer spiral ganglion cells really related to better clinical performance?" In: *Acta Otolaryngol.* 132.5 (2012), pp. 482–490.
- [216] Aayesha M Khan et al. "Is word recognition correlated with the number of surviving spiral ganglion cells and electrode insertion depth in human subjects with cochlear implants?" In: *Laryngoscope* 115 (2005), pp. 672–677.
- [217] Waldo Nogueira and Go Ashida. "Development of a parametric model of the electrically stimulated auditory nerve". In: *Lect. Notes Appl. Comput. Mech.* Vol. 84. 2018, pp. 349–362. ISBN: 978-3-319-59547-4.
- [218] Nerea Mangado et al. "Towards a complete in silico assessment of the outcome of cochlear implantation surgery". In: *Mol. Neurobiol.* 55.1 (2018), pp. 173–186.
- [219] Johan H M Frijns, David M T Dekker, and Jeroen J Briaire. "Neural excitation patterns induced by phased-array stimulation in the implanted human cochlea." In: *Acta Otolaryngol.* 131.4 (2011), pp. 362–70.
- [220] Sébastien Joucla and Blaise Yvert. "The "mirror" estimate: An intuitive predictor of membrane polarization during extracellular stimulation". In: *Biophys. J.* 96.9 (2009), pp. 3495–3508.
- [221] Andres Agudelo-Toro and Andreas Neef. "Computationally efficient simulation of electrical activity at cell membranes interacting with

- self-generated and externally imposed electric fields." In: *J. Neural Eng.* 10.2 (2013), p. 026019.
- [222] Randy K Kalkman, Jeroen J Briaire, and Johan H M Frijns. "Current focussing in cochlear implants: An analysis of neural recruitment in a computational model". In: *Hear. Res.* 322 (2014), pp. 89–98.
- [223] Kae Jiun Chang and Matthew N. Rasband. "Excitable domains of myelinated nerves: Axon initial segments and nodes of ranvier". In: *Curr. Top. Membr.* 72 (2013), pp. 159–192.
- [224] Robert H Pierzycki et al. "Tinnitus and Sleep Difficulties after Cochlear Implantation". In: *Ear Hear.* 37.6 (2016), e402–e408.
- [225] Margaret W Skinner et al. "Effect of stimulation rate on cochlear implant recipients' thresholds and maximum acceptable loudness levels." In: *J. Am. Acad. Audiol.* 11.4 (2000), pp. 203–213.
- [226] Gabriella Tognola et al. "Numerical modeling and experimental measurements of the electric potential generated by cochlear implants in physiological tissues". In: *IEEE Trans. Instrum. Meas.* 56.1 (2007), pp. 187–193.
- [227] Spelman Fransis A, B. M. Clopton, and B. E. Pfingst. "Tissue Impedance and Current Flow in the Implanted Ear Implications for the Cochlear Prosthesis". In: *Ann. Otol. Rhinol. Laryngol.* 98 (1982), pp. 3–8.
- [228] W F Sewell. "The relation between the endocochlear potential and spontaneous activity in auditory nerve fibres of the cat." In: *J. Physiol.* 347 (1984), pp. 685–96.
- [229] Yoshiyuki Horio. "Potassium channels of glial cells: distribution and function." In: *Jpn. J. Pharmacol.* 87 (2001), pp. 1–6.
- [230] A Verkhratsky and C Steinhäuser. "Ion channels in glial cells." In: *Brain Res. Brain Res. Rev.* 32.2-3 (2000), pp. 380–412.
- [231] Harald Sontheimer, Joel A Black, and Stephen G Waxman. "Voltage-gated Na<sup>+</sup> channels in glia: properties and possible functions". In: *Trends Neurosci.* 19.8 (1996), pp. 325–331.
- [232] Li Yen M Huang, Yanping Gu, and Yong Chen. "Communication between neuronal somata and satellite glial cells in sensory ganglia". In: *Glia* 61.10 (2013), pp. 1571–1581. arXiv: NIHMS150003.
- [233] David B Pisoni et al. "Three challenges for future research on cochlear implants". In: *World J. Otorhinolaryngol. - Head Neck Surg.* (2018).